



POLITECNICO DI MILANO
DEPARTMENT OF MECHANICAL ENGINEERING
DOCTORAL PROGRAMME IN DYNAMICS AND VIBRATION OF
MECHANICAL SYSTEMS AND VEHICLES

INNOVATIVE CONTROL STRATEGIES FOR 4WD
HYBRID AND ELECTRIC VEHICLES

Doctoral Dissertation of:
Michele Vignati

Supervisor:

Prof. Edoardo Sabbioni & Federico Cheli

Tutor:

Prof. Massimiliano Gobbi

The Chair of the Doctoral Program:

Prof. Bianca Maria Colosimo

Year 2016 – Cycle XXIX

*Remember that all models are wrong;
the practical question is how wrong
do they have to be to not be useful.*
George E. P. Box

Abstract

IN recent years, the environmental concern has generated an high improvement in hybrid and electrical mobility technology. The use of electric motors to drive the vehicle allows to completely review the design of the vehicle in particular the powertrain layout. Several layouts are in fact available for the electric powertrain; the most interesting is the one with four electric motors, one per each wheel. The main interesting feature of this layout is the possibility of independently applying driving or braking torques on each wheel, i.e. torque vectoring control strategies can be fully exploited. In this doctoral dissertation thesis an innovative control strategy for IWM vehicles is developed. The proposed controller can increase vehicle performance and safety in cornering both on high and low friction conditions. The controller is made of two contributions: one, for steady-state cornering, is based on optimal control theory; the second, mainly for stability control, is based on a yaw index that does not need any vehicle model or friction coefficient/vehicle state estimation. This control strategy has been tested by means of numerical simulation both in transient and in steady-state conditions, in open and in close loop, on high and low friction road surface. The control strategy has also been applied to different powertrain layouts in order to highlight the possible improvement given by torque vectoring control strategy on the vehicle lateral dynamics behaviour even considering a reduced number of EMs (i.e. lower than four).

Contents

Symbols, Indices and Acronyms	VII
Summary	1
1 State of the art	5
1.1 Torque Vectoring control strategies	6
1.1.1 PIDs controller	7
1.1.2 Optimal Controllers	10
1.1.3 Sliding mode controller	11
1.1.4 Model Predictive control	12
1.1.5 Fuzzy controller	13
1.1.6 Conclusions on literature review	14
1.2 Torque vectoring actuation devices	14
1.2.1 Semi-active differential	14
1.2.2 Active differential	15
1.2.3 Independent brake control system	17
1.2.4 Electric motor	18
1.2.5 In-Wheel Motors	19
2 Vehicle model for dynamics simulation	25
2.1 Vehicle model	25
2.1.1 Dynamics of car body	27
2.1.2 Virtual work on chassis	28

CONTENTS

2.1.3	Wheels dynamics	28
2.1.4	Suspensions forces	29
2.2	Tyre model	29
2.2.1	Slips and slip angles calculation	29
2.3	In-Wheel motors model	30
2.4	Driver model	30
2.5	Model validation	33
3	Vehicle dynamics controller	35
3.1	Torque vectoring analysis	35
3.2	Main scheme of the controller	38
3.3	Transient control strategy	40
3.3.1	Yaw moment generation	43
3.3.2	State-space behaviour of the controller	43
3.3.3	Severe braking in turn manoeuvres	45
3.4	Steady-state optimal controller	50
3.4.1	Vehicle model	50
3.4.2	Cost function and gain definition	53
3.4.3	References	54
3.4.4	Torque distribution strategy	55
4	Vehicle state estimation	59
4.1	Vehicle speed estimation	59
4.2	Sideslip angle and friction coefficient	62
5	Simulation results	69
5.1	Steady-state circular driving behaviour	70
5.1.1	Steering pad constant radius	70
5.1.2	Steering pad constant speed	73
5.2	Lateral transient response	75
5.2.1	Steer step	75
5.2.2	Braking in a turn	80
5.2.3	Power on manoeuvre	82
5.2.4	Double lane change	83
6	TV for different powertrain layouts	89
6.1	Steady-state torque distribution strategy for different layouts	91
6.2	Simulation results	92
6.2.1	Steady-state circular driving behaviour	92

6.2.2	Transient cornering behaviour	95
6.3	Considerations on different powertrain layouts	101
7	Design of experimental vehicle prototype	103
7.1	Vehicle layout	103
7.1.1	Electric motors	104
7.1.2	Motor drives	104
7.1.3	Battery pack	106
7.1.4	Vehicle control unit	106
7.1.5	Transmission	108
7.1.6	Driver's inputs	108
7.1.7	Sensors	108
7.2	Vehicle expected performances	108
	Conclusions	111
A	MF-Tyre model	113
A.1	Longitudinal Force (pure longitudinal slip)	114
A.2	Lateral Force (pure side slip)	115
A.3	Longitudinal Force (combined slip)	115
A.4	Lateral Force (combined slip)	115
A.5	Relaxation length	116

CONTENTS

Symbols, Indices and Acronyms

Symbol	Description	Units
α	slip angle	rad
β	sideslip angle	rad
δ	wheel steer angle	rad
δ_{sw}	steering-wheel angle	rad
φ	chassis roll angle	rad
ϑ	chassis pitch angle	rad
ψ	chassis yaw angle	rad
ω	wheel rolling angular velocity	rad/s
a_x	longitudinal acceleration of the vehicle	m/s ²
a_y	lateral acceleration of the vehicle	m/s ²
C_α	tyre cornering stiffness	N/rad
C_κ	tyre driving stiffness	N
\mathbf{i}	versor of x axis	
\mathbf{j}	versor of y axis	
\mathbf{k}	versor of z axis	
l	vehicle wheelbase	m
l_f	vehicle cog distance from front axle	m
l_r	vehicle cog distance from rear axle	m
t_f	front axle half track width	m
t_r	rear axle half track width	m
T	torque on wheel	Nm

CONTENTS

v_x	longitudinal velocity; vehicle velocity component along vehicle x axis	m/s
v_y	lateral velocity; vehicle velocity component along vehicle y axis	m/s

Indices	Description
f	front
r	rear

Acronyms	Description
4IWD	Four Independent Wheel Drive
4WD	Four Wheel Drive
AWD	All Wheel Drive
BEV	Battery Electric Vehicle
EV	Electric Vehicle
HEV	Hybrid and Electric Vehicles
ICE	Internal Combustion Engine
IWM	In-Wheel Motor
EKF	Extended Kalman Filter
EM	Electric Motor
ESP	Elektronisches Stabilitätsprogramm
FIWD	Front Independent Wheel Drive
FWD	Front Wheel Drive
LQR	Linear Quadratic Regulator
NLPC	Non-Linear Predictive Control
RIWD	Rear Independent Wheel Drive
RWD	Rear Wheel Drive
SAT	Self Aligning Torque

Summary

IN last decades the research on hybrid and electric mobility has grown pushed by an high request of green transportation. Many powertrain layouts have been designed trying to exploit all the potential of electric motors. Among all the possible layouts, the one which is the most interesting for torque vectoring is represented by four independent wheel driven vehicle [29]. This layout can be realised with onboard motors with driving shafts or with in-wheel motors (IWM), i.e. motors collocated directly inside the wheel [27, 12].

The difference between the two solutions consists in the fact that onboard motors are classical electric motors which are connected to the wheel via a driving shaft and a motor reducer to adapt motor speed range to wheel speed range. IWMs instead are located inside wheels, this means that no driveshafts and no motor reducers are required, but, typically, to obtain smaller speed range the number of motor poles is increased. This means that the increase in efficiency due to the absence of motor reducer is partially mitigated by the increase of poles number.

Typically, IWMs have the motor stator that is fixed to wheel hub, the rotor instead is fixed to the rim so that the motor is completely housed inside the wheel. There are several advantages concerned with IWMs: all transmission components can be eliminated. This means room saving, weight saving and less components to take care of and maintain; available space can be saved onboard vehicle which can be used for larger batteries or for increasing comfort of passengers. The main drawback of IWMs is the in-

crease in unsprung masses which means that suspension stiffness has to be properly adjusted in order to maintain vehicle handling and comfort characteristics [1].

The main advantage of IWMs is instead the possibility of independently apply driving or braking torque on each wheel and thus the possibility to design in the easiest way a Torque Vectoring control strategy [9].

Optimal control theory is the most common approach used in the literature to design torque-vectoring control of IWM vehicles [35, 37, 13]. Specifically, Linear Quadratic Regulators (LQR) and Linear Quadratic Gaussian (LQG) controllers have been developed, able to effectively allocate driving/braking torque to the wheels based on a vehicle model (generally a single-track vehicle model). These kind of controllers have proved to be very effective in improving vehicle handling. However they require the estimation of the actual motion of the vehicle (sideslip angle and yaw rate) and to update the reference-model parameters (such as cornering stiffness) whenever working conditions change (as an example when road adherence conditions change). It can be argued how this is of concern particularly during manoeuvres characterised by very fast transients, such double lane changes or step-steer manoeuvres.

To further investigate the above mentioned issues in the design of torque-vectoring control of a IWM vehicle, a strategy based on optimal control theory is coupled with a control logic relying upon an index (called yaw index in the following), which is directly related to oversteering/understeering behaviour of the vehicle and it is based only on measured quantities (vehicle speed, yaw rate and lateral acceleration). During the transient parts of a manoeuvre, the control action is mainly decided based on the proposed yaw index, since it does not require any estimators/observers. In steady-state, the control strategy is instead mainly driven by optimal control, whose parameters are updated during transients (where decisions are taken based on the yaw index). To avoid that torque demanded by the control strategy to a single wheel may exceed the maximum available and prevent wheel spinning/locking-up a torque distributor is added to the control system.

In particular the thesis is structured as follows.

The first chapter of this thesis is a review of literature state of the art for what concerns torque vectoring control strategies and torque vectoring actuating devices.

Second chapter presents the numerical model used in simulations. It consists of 14 dof vehicle model where contact forces are modelled ac-

ording to Pakejca MF Tyre formulation, motor model and driver model developed in order to simulated close loop manoeuvres.

Third chapter shows in details the newly designed control strategy based on torque vectoring applied to four independently wheel driven vehicle equipped with in-wheel motors.

Forth chapter presents the estimators necessary to the controller. In particular, a fuzzy speed estimator and an Extended Kalman Filter for estimating sideslip angle and friction coefficient between tyres and wheels have been developed.

Fifth chapter reports the simulations results for testing controller effectiveness. Several manoeuvres have been simulated to test controller both in steady-state and in transient manoeuvres, with and without the coupling with driver (close loop and open loo manoeuvres) and considering the effect of tyre-road friction coefficient variation.

Sixth chapter presents the adaptation of the control strategy to different powertrain layouts of HEV. In particular it has been applied to two wheel drive vehicle (front and rear) and to plug-in solutions which can be mounted on common front or rear wheel drive ICE vehicle.

Last chapter presents the EV prototype which is being developed to test the effectiveness of the controller in real driving conditions.

CONTENTS

CHAPTER *1*

State of the art

VEHICLE lateral dynamics control is one of the most important feature of nowadays passengers' cars and vehicles since it is mainly connected to vehicle safety. There are several ways of affecting vehicle lateral behaviour, the most commonly used strategy both for lateral dynamics safety and performances improvement is base on torque vectoring.

In this thesis, torque vectoring is applied on four wheel independently driven vehicle in order to maximize the usage of in-wheel motors (IWM).

Torque vectoring consists in generating different longitudinal forces on wheels in order to develop a yaw moment on the vehicle that can change vehicle lateral dynamics. Considering figure [1.1](#), the equation of the in

plane motion of the vehicle are

$$\begin{cases} ma_x = \sum_i (F_{x,i} \cos \delta_i - F_{y,i} \sin \delta_i) \\ ma_y = \sum_i (F_{x,i} \sin \delta_i + F_{y,i} \cos \delta_i) \\ J_z \ddot{\psi} = \sum_i (F_{x,i} \sin \delta_i + F_{y,i} \cos \delta_i) l_i - \sum_i (F_{x,i} \cos \delta_i - F_{y,i} \sin \delta_i) c_i \end{cases} \quad (1.1)$$

where $F_{x,i}$ and $F_{y,i}$ are respectively the longitudinal and lateral contact forces of the tyre, l_i and c_i are respectively x and y coordinates of the i -th wheel in the cog reference frame, δ_i is the steer angle of the i -th wheel. Without losing in generality, if small steer angles are considered, the third equation of equations (1.1) becomes

$$J_z \ddot{\psi} = \sum_i F_{y,i} l_i - \sum_i F_{x,i} c_i \quad (1.2)$$

where it can be noticed that longitudinal forces F_x can affect yaw equilibrium of the vehicle, i.e. longitudinal forces can be used to steer the vehicle. The idea of torque vectoring is to generate suitable torques on wheels in order to obtain the desired yaw moment M_z induced by longitudinal forces.

$$M_z = M_{z,f} + M_{z,r} = (F_{x,fl} - F_{x,fr}) \frac{t_f}{2} + (F_{x,rl} - F_{x,rr}) \frac{t_r}{2} \quad (1.3)$$

The desired yaw moment M_z can be obtained according to different needs, lateral stability or performance improvement, and it can be generated using different actuators. In the following, a review of literature is presented and divide in two section: the first one presents the control strategies for torque vectoring while in the second one actuators for torque vectoring are analysed.

1.1 Torque Vectoring control strategies

Several approaches are available in literature and almost all method of classical and modern control have been applied for controlling vehicle lateral dynamics.

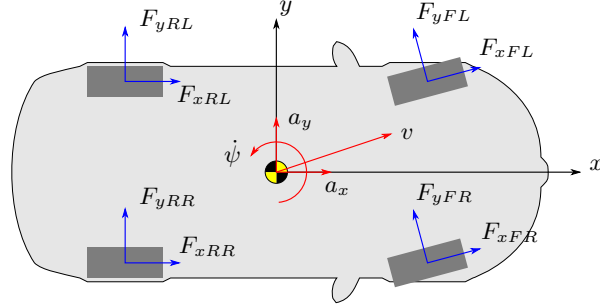


Figure 1.1: *Four contact point vehicle model*

1.1.1 PIDs controller

The simplest approach to torque vectoring consists in PID controllers which generate a yaw moment proportional to the error between a reference and the actual state.

Chõng and others [7] in 1996 proposed a proportional controller based on a linearised single track vehicle model. The proposed controller consists in a feedback part on vehicle yaw rate $\dot{\psi}$ and a feedforward part on steering angle δ . The difference of longitudinal forces (i.e. the yaw moment) on the front and rear axles is the same and it is calculated according to the following equation

$$\Delta F_f = \Delta F_r = -k_b \dot{\psi} + k_f \delta_f \quad (1.4)$$

where k_b and k_f are respectively the feedback and the feedforward gains. The feedback gain is designed to make the damping ratio entirely independent on the vehicle speed while the feedforward gain is calculated to achieve that the steady-state value of sideslip angle β is zero. Drawbacks of this work are that: friction coefficient effect is not accounted; sideslip angle is not measured or estimated, this means that the effectiveness of the controller cannot be checked; high speed, where stability concerns may arise, have not been considered.

Hallowell and Ray in [16] designed a control strategy based on two contributions: a traction controller and a stability controller. The controller requires the measurements of brake and accelerator pedal position, wheels angular velocities, steer angle, steer angle rate and yaw rate. The traction

controller reduces the torque applied on each wheel as function of the estimated slip condition through wheel acceleration ($\dot{\omega}$) evaluation; the slip κ of the wheel is evaluated according to the following equation

$$\kappa = \frac{|\omega| - |\omega_{ideal}|}{\max(\omega, \omega_{ideal})} \quad (1.5)$$

Vehicle stability controller is instead a proportional controller that generates a yaw moment M according to the difference between actual yaw acceleration ($\ddot{\psi}$) and its desired value which is inferred from the driver commanded steer angle rate $\dot{\delta}_{SW}$. Again, no consideration have been done on the effect of friction variation.

Osborn and others, in [29], showed the results of a sensitivity analysis using a simplified non-linear vehicle model used as the basis for a successful vehicle dynamics control strategy. Only control parameters realistically measurable on a vehicle were used. By varying the front-rear torque distribution with a yaw velocity error feedback, and the left-right ratio with lateral acceleration error feedback, the handling objectives of maintaining vehicle path and maximizing acceleration can be fulfilled. Control of front-rear torque distribution alone delivers almost the same performance enhancement as fully independent control, for a considerably lower investment in hardware. A satisfactory tuning of the dual PI control loops was achieved with an iterative search approach. To achieve a robust implementation in-vehicle, fine-tuning of control parameters would be necessary combined with some degree of gain scheduling to handle different regimes of operation.

In [22], Kakalis and others presented the feasibility study of a system designed for the improvement of the handling characteristics of a sport vehicle based on the yaw moment control. The proposed system, named BTV, generates an asymmetric distribution of the longitudinal forces on the driving axle through an independent actuation of the brakes and a control of the throttle valve. The feed-forward part is constituted of a 3D map whose values correspond to the maximum oversteering moment tolerable by the car in various adherence levels. A PID controller to maintain stability is chosen for the feedback contribution.

In [32], Pinto and others developed a yaw motion control system based on torque vectoring of twin rear electric motors (called eDC). The main features of the system are the energy-efficient and unintrusive interventions, the high yaw authority in compensating understeer, the possibility of enforcing optimal yaw tracking in sub-limit driving, and the high potential for

ease of integration with an existing ESC system. The PID control strategy generates a yaw moment on the vehicle in order to reduce the error between reference yaw rate and actual yaw rate $\dot{\psi}$. Control intervention is limited when sideslip angle β exceed given boundary values. β is estimated by integration of $a_y/v_x - \dot{\psi}$ when non-stationary behaviour is detected. This method can lead to some error in sideslip evaluation in steady-state conditions since measurements are affected by noise which can cause integration process to diverge.

In [38] and in [39], Sill proposed a PID controller for lateral dynamics where the torques applied on wheels are decided according to saturation estimation. Axle saturation is thus explicitly quantified and used in a feedback structure. This was then used along with a direct yaw-moment control component. The method enabled stabilization of a nominally over-steering vehicle while retaining yaw responsiveness. Simulation results revealed the benefits of each piece of the control scheme: the stable completion of the extreme avoidance manoeuvre due to the saturation balancing control as well as an improved response from direct yaw-moment control.

In [8], a PID on yaw rate error is compared both with passive vehicle and active with sliding mode controller. The results highlight the ability of the controllers to significantly change the understeer characteristic compared with the baseline vehicle. In the case of the PID controllers, a preliminary analysis in the frequency domain has shown that gain scheduling is not necessary for compensating variations in the vehicle yaw rate response at different operating points. Furthermore, in both quasi-steady-state manoeuvres and typical transient tests, the PID algorithms allow good tracking performance and acceptable robustness against variations in the main vehicle parameters and operating conditions. The tracking performance in quasi-steady-state conditions is further enhanced by the suboptimal sliding-mode approach, which also achieves the objective of minimizing the variation in the vehicle yaw rate in acceleration conditions during tip-in manoeuvres while cornering. However, the sliding-mode controllers can provoke undesirable oscillations in yaw rate during step steer manoeuvres at high steering amplitudes. Overall, ease of implementation, predictable behaviour, and good frequency response are key characteristics in favour of the PID controllers for real vehicle applications.

1.1.2 Optimal Controllers

An other approach is based on Optimal Control Theory in which the control action is generated by minimising a cost function which can consider different targets.

Sakai and others [37] proposed a motion control for an electric vehicle with four independently driven in-wheel motors. They designed the controller according to Linear Quadratic Regulator theory based on linearised, time invariant, single track vehicle model. The control action is the yaw moment generated by differentiating the left and right longitudinal forces on wheels. In [36] they also presented a force distribution algorithm necessary to generate the desired yaw moment and the desired driving/braking force. The algorithm takes into account the wheel residual force according to friction limit.

Optimal control is used also by Esmailzadeh and others in [11]. They proposed a control law that relies on linearised time invariant single track vehicle model. It consists in the disturbance feed-forward signal, which is related to the input steering angle, and the two state variable feedback terms being those of the yaw rate $\dot{\psi}$ and the lateral velocity v_y .

$$J = \int_{t_0}^{t_f} \left[\frac{1}{2} (\dot{\psi} - \dot{\psi}_d)^2 + \frac{1}{2} w M_z^2 \right] dt \quad (1.6)$$

The obtained yaw moment is generated trough right to left difference of the longitudinal forces of the front and rear axles respectively. The controller is coupled with an estimator of sideslip angle which cannot be easily measured onboard vehicles.

In [17], Hancock and others designed a double feedback controller for an overdriven differential. The primary feedback is designed using a quadratic cost function which attempts to create a neutral steer characteristic. The primary feedback relies on 2DOF vehicle model, in which linear lateral forces are considered and the torque transfer ΔT from left to right side of vehicle is the control input. In vehicle model equations, two additional states δ_d and $\dot{\delta}_d$ are added to the system in order to account for driver dynamics. The cost function for LQR controller is thus

$$J = \int \left(r - \frac{U}{l} \delta_d \right)^2 dt + \int \left(\frac{1}{u_m^2} \right) u^2 dt \quad (1.7)$$

where the main goal of the controller is to obtain a neutral steering behaviour of the vehicle, reference yaw rate is in fact equal to $\frac{U}{l} \delta_d$. u_m rep-

resents instead the maximum torque ΔT that can be developed by active differential without saturating the tyres. The secondary controller aims instead to minimize the deviation in yaw behaviour between the reference and vehicle models, its purpose is to account for non linearities which are non considered in linear reference model of the primary feedback. An other cost function is then defined with the target of minimising the reference and the vehicle model error.

Ono, in [28], developed an integrated control for four-wheel-distributed steering and four-wheel-distributed traction/braking systems. The control strategy is based on tyre combined force allocation which focuses on maximum usage of available friction contact force on each wheel. Tyre grip margin and radius of friction circle was estimated using the relation among Self Aligning Torque (SAT), and the lateral and longitudinal forces of each tyre. Further, vehicle dynamics control based on the friction circle of each tyre has also been proposed. A distribution algorithm using SQP calculates the magnitude and direction of tyre forces, which satisfy constraints corresponding to the target resultant force and moment of the vehicle motion and minimize μ rate of each tyre γ which is an index defining tyre usage: for the i -th tyre

$$\gamma_i = \frac{\sqrt{F_{xi}^2 + F_{yi}^2}}{F_{zi}} \quad (1.8)$$

The global optimality of the convergent solution of the recursive algorithm was proved by extension to convex problem. This implies that the proposed distribution algorithm achieves theoretical limited performance of vehicle dynamics integrated control for steering and traction/braking systems. In addition, the effect of this vehicle dynamics control for the 4-wheel-distributed steering and 4-wheel-distributed traction/braking systems was demonstrated by simulation to compare with the combination of the various actuators.

The limit in these controllers is that they can handle only low lateral acceleration values since a linear vehicle model is used. Moreover the effect of friction is not considered although this parameter is of paramount importance when dealing with lateral dynamics stability.

1.1.3 Sliding mode controller

The use of electric motor, due to high bandwidth of the actuators, allows to develop controller based on sliding mode control theory. Same examples

are here reported.

In [34], Reiveley and other use a simplified vehicle dynamics model for the development of a variable torque distribution yaw moment controller for a prototype hybrid vehicle. An hybrid vehicle architecture was proposed to provide the facilities for a VTD yaw moment control. This control was developed through sliding mode control techniques based on a 2-DOF linearised reference model with a desired neutral steering response. To achieve a more robust implementation the control gains of the vehicle were determined through the use of an uncertainty analysis. Some challenges to the development of a robust control such as electric motor torque limitations and tyre force generation where presented. Numerical simulations have shown that torque vectoring control can be used to provide a more linear vehicle response to driver requests. However, the use of torque vectoring across the rear axle has shown to increase the operational sideslip angle of the vehicle during cornering events. In order to reduce the potential loss of control the use of available VTD force approximation was utilized. It should be noted that this method would rely on a system to estimate the road friction coefficient, which is not a directly measurable parameter. Therefore in authors' opinion it would be necessary to create more advanced controls to minimize the possibility of tyre saturation for the implementation of such a controller.

In [15], the problem of the torque-vectoring control of a four-wheel-drive fully electric vehicle with in-wheel drivetrains is addressed and a yaw rate controller based on integral sliding mode is presented. They presented an integrated sliding mode controller that is made of two contribution: a PID feedback contribution that stabilize the vehicle in absence of model uncertainties and a sliding mode controller that deals with the generalized model uncertainties and guarantees robustness. A low pass filter is used in order to reduce chattering.

1.1.4 Model Predictive control

In [14], wheel torque control systems were developed using Non-Linear Predictive Control (NLPC) theory for drive or brake torque distribution and a brake-based ESP system to control the vehicle longitudinal and lateral dynamics, in which the range of control inputs was limited to physically realizable values. The simulation results indicated that the controller can achieve good control of vehicle behaviour in extreme manoeuvres, and showed robust performance owing to the changes in the road condition. The frame-

work presented in this paper can also, potentially, be expanded to include control inputs such as active steer and active anti-roll bars for the development of an integrated chassis control algorithm.

1.1.5 Fuzzy controller

An other different approach relies on Fuzzy control theory. In [33], Pusca and others designed a fuzzy controller for a AWD vehicle with independent motors. The command rules are given by a complex table in which the torque command is defined according to reference yaw rate, actual yaw rate, actual steer angle, estimated slip and others. This lateral control system is then coupled with a slip control system which considers both slip estimation and slip angle estimation. Linguistic rules are associated to vehicle state condition and the lateral dynamics controller decide on which wheel a torque can be applied. The decision is taken according to the amount of residual longitudinal force available which is calculated according to fuzzy rules.

In [23] an alternative approach to optimal problem is presented. It consist in solving the optimal torque distribution by means of genetic algorithm. In that paper, Kim and others proposed a vehicle stability control logic for a 4WD hybrid electric vehicle using regenerative braking of the rear motor and EHB. To obtain the optimal brake torque distribution between the regenerative braking torque and the EHB torque, a genetic algorithm is used. The genetic algorithm calculates the optimal regenerative braking torque and the optimal EHB torque for the given inputs of the desired yaw moment and road friction coefficient. Based on the optimal brake torque distribution, the vehicle stability control logic proposed generates the desired direct yaw moment to compensate the errors of the sideslip angle and yaw rate by a fuzzy control algorithm corresponding to the driver's steering angle and vehicle velocity. Performance of the vehicle stability control logic is evaluated by comparison of fixed regenerative braking and optimal regenerative braking for a single lane change manoeuvre. It is found from the simulation results that the optimal regenerative braking is able to provide the increased recuperation energy compared with fixed regenerative braking while satisfying the vehicle stability.

1.1.6 Conclusions on literature review

In general, what emerges from literature review is that most of control strategies do not account for vehicle non linearities, for friction coefficient variation or for vehicle state estimation when not measurable. Controllers based on optimal control theory are apparently the most performing for 4WD IWMs vehicles but these controllers need vehicle state knowledge which, on common commercial cars, must be estimated. In particular the most critical parameter is friction coefficient. The aim of this thesis is to develop a robust control strategy that can overcome the highlighted issues.

1.2 Torque vectoring actuation devices

There are several ways of applying torque vectoring in a vehicle. In common Internal Combustion Engine (ICE) torque vectoring can be applied in different fashions: brake torque vectoring (BTV), semi-active and active differentials. Usually brake based torque vectoring systems are applied in lateral stability control systems, conversely semi-active and active differential have the duty to improve vehicle cornering performances. In an independently wheel driven electric vehicle both the purposes are demanded to the electric motors that can both drive and brake the wheels independently. Only for high braking torques the mechanical brakes are required.

1.2.1 Semi-active differential

Semi-active differential is an evolution of common differential in which one of the two driving shafts is equipped with a friction clutch that allows the torque transfer from one wheel to the other. The flow of torque direction is only from the faster to the slowest wheel. The working principle of the semi-active differential can be easily understood considering the virtual work principle applied to the schematic system reported in Figure 1.2. With respect to a common differential, an electronic controllable clutch is added. The here presented scheme considers hydraulically actuated multi-discs friction clutch. It is used to transfer torque from one shaft to the other. Considering a left turn in which the speed of the left wheel is lower than the right wheel speed ($\vartheta_l < \vartheta_r$), the overall virtual work of the system reads

$$\sum \delta L = T_h \delta \vartheta_h - T_r \delta \vartheta_r - T_l \delta \vartheta_l + T_f \delta \vartheta_l - T_f \delta \vartheta_h = 0 \quad (1.9)$$

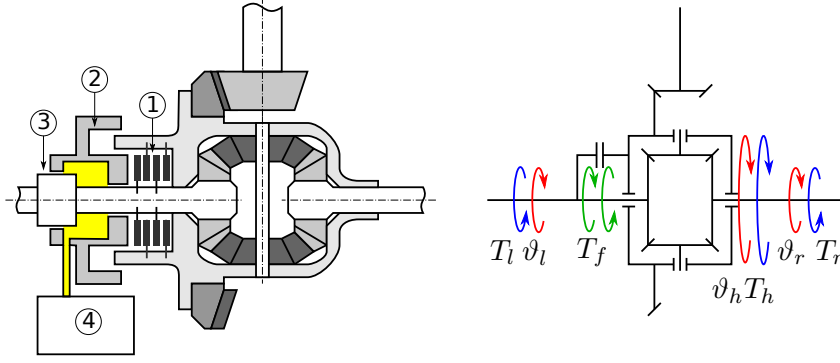


Figure 1.2: Scheme of a semi-active differential: 1. clutch plates, 2. actuation piston, 3. shaft pushing area, 4. control unit.

where T and ϑ are respectively the torque and the rotation about their own axis of differential housing \bullet_h , left wheel shaft \bullet_l and right wheel shaft \bullet_r ; T_f is the friction torque of the clutch whose sign is taken according to the assumption $\dot{\vartheta}_l < \dot{\vartheta}_r$ (the opposite case in which $\dot{\vartheta}_l > \dot{\vartheta}_r$ can be easily obtained). Considering the kinematic relationship between housing rotation and wheel rotation

$$\vartheta_h = \frac{\vartheta_r + \vartheta_l}{2} \quad (1.10)$$

substituting equation (1.10) into the virtual work equation (1.9), and solving for the two independent variable ϑ_r and ϑ_l we obtain

$$\begin{cases} T_r = \frac{T_h - T_f}{2} \\ T_l = \frac{T_h + T_f}{2} \end{cases} \quad (1.11)$$

this means that an amount of torque T_f developed by friction clutch can be transferred from right shaft to the left shaft, i.e. from the fastest to the slowest shaft in absence of losses/dissipations.

1.2.2 Active differential

Active differential is a farther development of semi-active differential in which the limitation in torque transferring process is overcome. With active differential is in fact possible to transfer an amount of torque from one

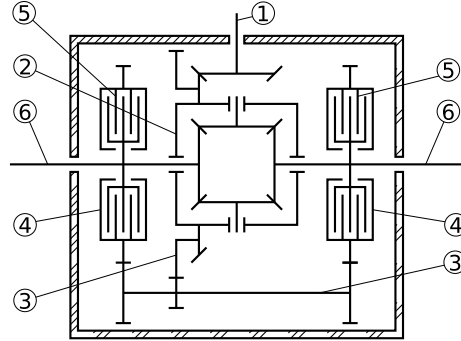


Figure 1.3: Active differential scheme: the input shaft 1 transfers driving power to the traditional bevel gear differential 2 and, through the additional gearing 3, to the clutch housings 4. Clutch discs 5 are fixed to the output axles 6.

wheel to the other independently on the relative speed between the two of them. This possibility is obtained with an high increase in cost and mechanical complexity of the system.

In Figure 1.3 is reported the scheme of an active differential (see [3]). An auxiliary shaft is connect to the housing with a fixed transmission ratio τ . This auxiliary shaft is connected to both right and left shafts through controllable friction clutches. In this way clutches always spin faster than wheels shafts thus torque can be transferred independently from one shaft to the other.

In the following, l and r subscript indicate respectively left and right, f stands for friction clutch while h is for differential housing (bevel gear differential, n2 in Figure 1.3).

The torque transfer can be calculated applying the virtual work principle to the scheme in figure 1.3 obtaining

$$T_h \delta \vartheta_h - T_r \delta \vartheta_r - T_l \delta \vartheta_l + T_{fl} (\delta \vartheta_f - \delta \vartheta_l) + T_{fr} (\delta \vartheta_f - \delta \vartheta_r) = 0 \quad (1.12)$$

where T_{fl} and T_{fr} are the friction torques applied on left and right shaft respectively; ϑ_f is the clutches speed

$$\vartheta_f = \tau \vartheta_h \quad (1.13)$$

rearranging the equation we end up with the expression of the wheels torques

$$\begin{cases} T_h - 2T_l + T_{fl}\tau - 2T_{fl} + T_{fr}\tau = 0 \\ T_h - 2T_r + T_{fl}\tau + T_{fr}\tau - 2T_{fr} = 0 \end{cases} \quad (1.14)$$

(e) and return flow pump (f). The return flow pump begins to convey brake fluid in order to continue raising the brake pressure.

Hold pressure: The intake valve (c) closes. The exhaust valve (d) remains closed. The pressure cannot escape from the wheel brake cylinders. The return flow pump stops (f) and control valve (a) closes.

Reduce pressure: control valve (a) switches to the opposite direction. The intake valve (c) remains closed while the exhaust valve opens. The brake fluid can flow back through the tandem master cylinders into the reservoir.

In this way each wheel has an independent circuit and can be braked independently from others. This system is mainly used in active safety systems like ESP where a speed reduction is preferable. It can also be used for cornering performances improvement but the driving torque must be increased contemporary in order to obtain no speed reduction of the vehicle, this is the bases of Brake Torque Vectoring (BTV).

As stated in [22], as far as handling performance is concerned, BTV showed its superiority with respect to the semi-active differential and allows to get the same improvement provided by an active differential under several operating conditions.

1.2.4 Electric motor

It is of really high interest the use of electric motors (EM) in powertrain layout where two or more wheels are controlled independently through a dedicated EM. There are several layouts for electric powertrain which will be further discussed in the following. Here the attention is focused on the two possible solutions for connecting one motor to one wheel. The most forthright solution is to use conventional EM with a gearbox placed on-board and connected to the wheel through a drive shaft. This solution allows the use of high speed compact conventional EM [24]. Electric motors have faster response than ICE and can drive the wheels from zero speed, this allows to eliminate the clutch. Also the energy efficiency of EM is really high and, since EM are reversible, it is possible to recover energy in braking with the same machine. Also the bandwidth of EM is significantly higher than hydraulic brakes. On the other hand, to apply torque vectoring several distributed motors are needed. For high braking manoeuvres the braking torque of EM is not enough to stop the vehicle within an acceptable

distance, this means that hydraulic brakes cannot be fully eliminated but downsized. If pure electric vehicles are considered, the weight of battery is considerable and may be greater than the weight saved when removing ICE, gear box, driving shafts etc...

As EM has been rediscovered in recent years for driving vehicle purposes, many authors developed energetic model of electric powertrain in order to highlight the superior energy efficiency of such powertrain. In [6], Cheli and others proposed an energetic model that simulates the overall power flux between the different power trains installed on an Plug-In HEV in order to estimate the energy consumption of the vehicle in the different possible modes. They showed the cumulative energy consumption obtained during simulation (both for the pure electric that for the ICE modality) is satisfactory similar to the experimental ones. The validation of the model described would be the bases for developing control strategies for hybrid vehicle, in particular plug in ones before testing on a prototype.

In [31], instead, a feasibility study of a energy control strategy is presented. The target of the strategy is to minimise the overall power consumption of the vehicle based on the knowledge of each motor characteristic in terms of torque and in terms of efficiency maps.

1.2.5 In-Wheel Motors

A particularly interesting evolution of EM for driving vehicles is represented by the so called In-Wheel Motors (IWM). IWM are electric motors collocated directly inside the wheel where the rotor of the motor is directly plug to wheel hub shaft. This is certainly not a new idea, with US patents recorded in 1884 discussing the concept and the Lohne Porsche (see Figure 1.5) of 1899 selling 300 copies of a vehicle with IWM. This ideas has being studied intently for NASA's successful lunar rover vehicle.

Recently some industry dusted off this idea to follow the increasing request of electric mobility. In Figure 1.6 a modern IWM developed by Pro-tean Electric is reported.

Several advantages are given by the use of IWM. Studies by Murata [27] considered the feasibility of installing IWM on existing suspension systems, proposing several solutions. He highlighted the benefits in overall vehicle weight reduction as shown in Figure 1.7a; an estimated reduction of about 36% can be achieved. In fact many components of the driveline can be removed: differential gear, driveshafts. Suspensions arms and brakes have to be redesigned, but brakes can be downsized since a considerable amount

1.2. TORQUE VECTORING ACTUATION DEVICES



Figure 1.5: *The young Ferdinand Porsche came up with the idea for the design of the Lohner-Porsche vehicle. Instead of complex drive trains, internal-pole electric motors powered the front wheels directly. The hub-mounted electric motors were powered by batteries with a terminal voltage of 60-80 V and a capacity of 170-300 Ah. At a normal speed of 35 km/h the vehicle had a range of around 50 km. The Lohner-Porsche received a great deal of recognition and praise at the Paris Exposition of 1900.*

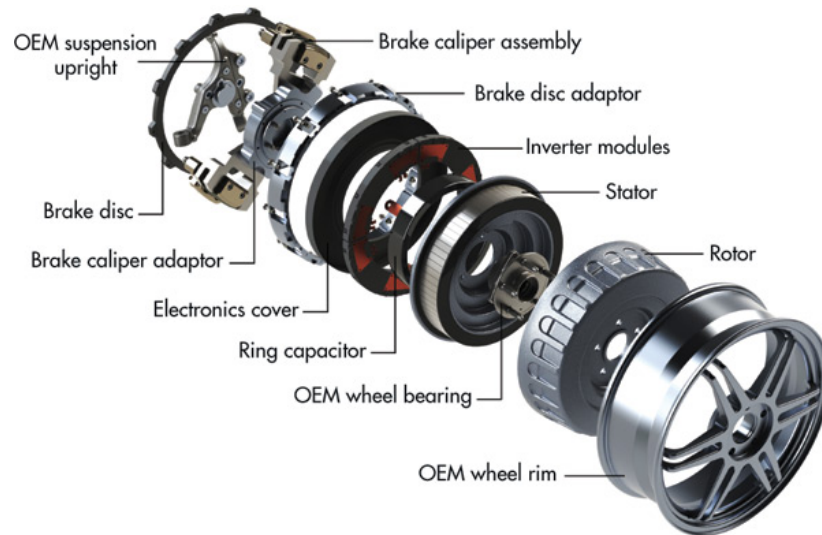


Figure 1.6: *Modern example of In-Wheel Motors. Custom micro-inverter modules from TT electronics will provide the integrated power electronics in Protean In-Wheel Motors (courtesy of TT Electronics and Protean Electric)*

Table 1.1: *IWM: comparison of package efficiency ([27]). FF front engine, front driven. FR front engine, rear driven. MR mid engine, rear driven. RR rear engine, rear driven.*

	FF	FR	MR/RR	IWM
Space efficiency	Good Large interior space	Poor Requires space for propeller shaft and differential gear	Very poor At worst, only 2 occupants possible	Excellent Installed inside tire
Drive efficiency	Excellent Everything inside engine compartment	Good Propeller shaft loss	Poor Cooling pipes/AC pipes, etc.	Excellent Everything inside tire
Tyre efficiency	Poor Same tyres at rear despite low load	Good Traction improvement	Excellent Maximum efficiency by using different size tyres at front/rear	Excellent Same as MR vehicle

of braking torque can be developed by IWM. IWM can also become the main actuator for limit braking manoeuvre where it can improve ABS efficiency due to its faster response with respect to hydraulic brakes. In driving condition, driving shaft flexibility is removed with benefits on response to accelerator pedal.

This mass reduction is followed by a lowering of the vehicle cog with several advantages in vehicle dynamics, in particular in driving efficiency. Also more room can be saved onboard in correspondence of front and rear axles leading to a possible increase in turning angle and a lower rear floor. Murata summarises all this effect in table 1.1.

The main drawback of IWM is the increase in unsprung masses. This effect is critical because the unsprung mass is directly connected to roadholding capability and ride comfort of the vehicle. Murata highlight it (see Figure 1.7b) estimating a mass increase of about 23%, by the way he showed also that the ratio between unsprung and sprung mass of a IWM vehicle is comparable with front engine front driven vehicle. Other authors faced this problem.

Vos and others in [40] studied the influence of in-wheel motors on the ride comfort of vehicles. Experiments on open road with an ICE vehicle with artificially increased unsprung masses showed that motors in the front wheels decrease the ride comfort between 10% and 25%, depending on the severity of the road. Motors in the rear wheels decrease the ride comfort only between 1% and 8%. Using a validated model, they showed that due to the placement of heavy battery packs, the ride comfort of a battery elec-

1.2. TORQUE VECTORING ACTUATION DEVICES

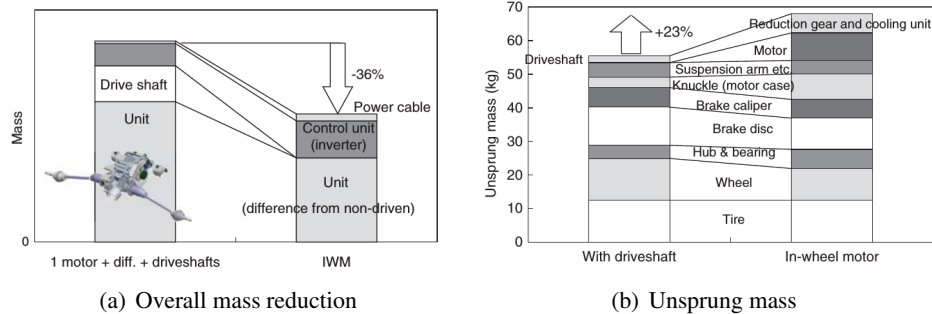


Figure 1.7: *Murata consideration on IWM effect on vehicle overall mass and unsprung mass.*

tric vehicle (BEV) is 14% increased with respect to an ICE vehicle. The dynamic wheel load and suspension travel increase only slightly. A 160 kg heavier BEV with in-wheel motors has the same ride comfort as the original ICE vehicle. However, the motors do increase the dynamic wheel load up to 40%. An active hybrid controlled electromagnetic suspension system is able to diminish the dynamic wheel load from 40% to around 20%. Since this is not enough to guarantee the safety of the vehicle, other control approaches have to be investigated.

Anderson and Harty in [1] show the results of several tests performed with a commercial vehicle after adding 30 kg of mass on each wheel. They compared obtained results with the ones of the original vehicle and concluded that the obvious impact of implementing in-wheel motors on a vehicle is to increase its unsprung mass. Slightly less obvious effects are to increase the yaw inertia and to improve the torque response rate. Popular reservations around increased unsprung mass centre on degraded ride and grip performance.

These aspects of performance have been examined in detail and can be summarised thus:

ride overall: difference in road roughness results in very large differences in scores compared to influence of unsprung mass;

primary ride: ¹ no discernible difference on smooth roads, slight degradation in rough road performance

¹RMS of sprung mass vertical acceleration in frequency range 0-3Hz

secondary ride: ² slight degradation in both rough and smooth road performance may require detail changes to seat or suspension components;

refinement: ³ some change in suspension component detail may be required to recover small loss in refinement behaviour;

active safety: noticeable but not severe loss in smooth and rough road grip levels; slight increase in damping levels may be required to optimise performance;

driveability: slight changes to suspension components may be required to restore agility.

While perceptible differences emerge with increased unsprung mass, on the whole they are small and unlikely to be apparent to an average driver. The nature and magnitude of the changes appears to be nothing that cannot be overcome by the application of normal engineering processes within a product development cycle. Conversely, the promise of individual wheel motor control shows good potential for substantial improvements in vehicle behaviour.

²RMS of sprung mass vertical acceleration above 3Hz

³RMS of sprung mass fore-aft vertical acceleration using a 2 dof quarter car vehicle model

1.2. TORQUE VECTORING ACTUATION DEVICES

CHAPTER 2

Vehicle model for dynamics simulation

THE simulation of physical real systems has become a key point in engineering. New ideas can be tested easily, with really short time and without significant costs. In this chapter the vehicle, the motor and the driver models used in simulations are reported. The simulation environment used is Simulink Matlab[®].

2.1 Vehicle model

Vehicle dynamics is simulated through a 14 *dofs* vehicle model [5].

The independent variables used to describe vehicle dynamics are:

- longitudinal and lateral velocity of roll centre (${}^L v_{xRC}$ and ${}^L v_{yRC}$) and vertical velocity of roll centre (v_z)

$$\{\dot{q}_{bd}\} = \{ {}^L v_{xRC} \quad {}^L v_{yRC} \quad v_{zRC} \}^T \quad (2.1)$$

- chassis rotation about absolute z absolute axis (yaw ψ), about y local axis around pitch centre (pitch ϑ) and about x local axis around roll

2.1. VEHICLE MODEL

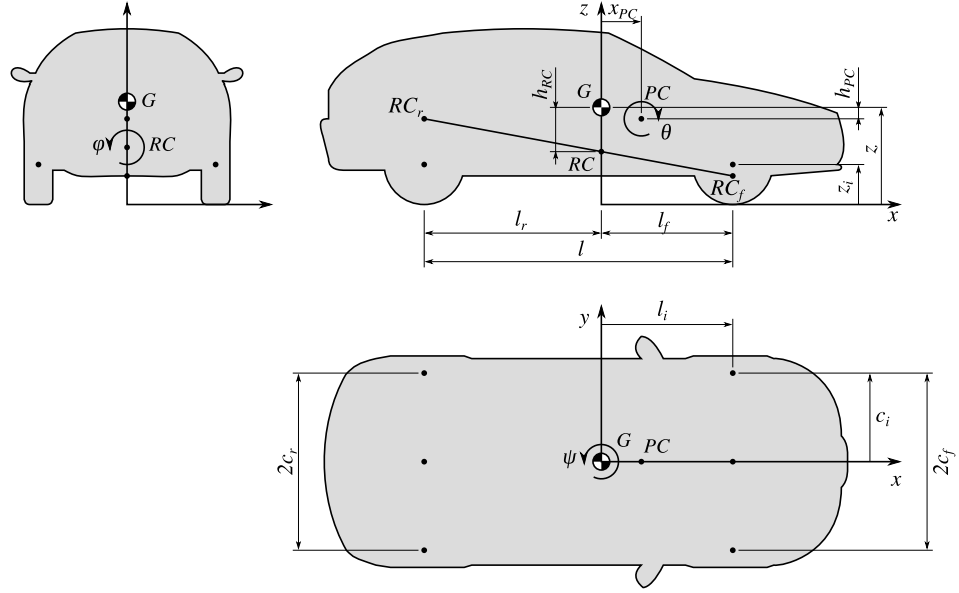


Figure 2.1: Vehicle model description

centre (roll φ)

$$\{\dot{q}_{br}\} = \{\dot{\varphi} \quad \dot{\vartheta} \quad \dot{\psi}\}^T \quad (2.2)$$

- unsprung masses absolute vertical displacement

$$\{q_{wd}\} = \{z_{fr} \quad z_{fl} \quad z_{rr} \quad z_{rl}\}^T \quad (2.3)$$

- wheels rotation about hubs axes

$$\{\dot{q}_{wr}\} = \{\omega_{fr} \quad \omega_{fl} \quad \omega_{rr} \quad \omega_{rl}\}^T \quad (2.4)$$

Some assumption are made. Pitch and roll rotation are considered small, thus gyroscopic effect are neglected. Vertical travel of the wheel is the unique relative displacement allowed between chassis and unsprung masses; this means that the longitudinal and lateral displacement of the unsprung mass in the $X_L - Y_L$ plane are supposed to take place as the unsprung mass was fixed to the chassis. No variation of wheelbase and track width are considered.

Figure 2.1 reports the main quantities used to write the equation of motion of the vehicle.

2.1.1 Dynamics of car body

The equation of motion for car body and unsprung mass displacement related to car body motion is

$$[M_b]\ddot{q}_b = -[M_{b,nl}]\dot{q}_b + Q_b \quad (2.5)$$

Where

$$[M_b] = \begin{bmatrix} m & 0 & 0 & 0 & m_b h_{PC} & 0 \\ 0 & m & 0 & -m_b h_{RC} & 0 & 0 \\ 0 & 0 & m_b & 0 & m_b x_{PC} & 0 \\ 0 & -m_b h_{RC} & 0 & J_x & 0 & 0 \\ m_b h_{PC} & 0 & m_b x_{PC} & 0 & J_y & 0 \\ 0 & 0 & 0 & 0 & 0 & J_{bz} \end{bmatrix} \quad (2.6)$$

with

$$J_x = J_{bx} + m_b h_{RC}^2 + \sum_{i=1}^4 m_i h_{ri}^2 \quad (2.7)$$

$$J_y = J_{by} + m_b (h_{PC}^2 + x_{PC}^2)$$

instead non linear effect of inertia forces are accounted with the following matrix

$$M_{b,nl} = \dot{\psi} \begin{bmatrix} 0 & -m & 0 & m_b h_{RC} & 0 & 0 \\ m & 0 & 0 & 0 & m_b h_{PC} & 0 \\ 0 & 0 & 0 & 0 & 0 & 0 \\ -m_b h_{RC} & 0 & 0 & 0 & -m_b h_{PC} h_{RC} & 0 \\ 0 & -m_b h_{PC} & 0 & m_b h_{PC} h_{RC} & 0 & 0 \\ 0 & 0 & 0 & 0 & 0 & 0 \end{bmatrix} \quad (2.8)$$

Where the velocity of car body cog absolute velocity is expressed in local reference frame. It is related to independent variable by the following expressions

$$\begin{Bmatrix} v_{xG} \\ v_{yG} \\ v_{zG} \end{Bmatrix} = \begin{Bmatrix} v_x + h_{PC} \dot{\vartheta} \\ v_y - h_{RC} \dot{\varphi} \\ v_z + x_{PC} \dot{\vartheta} \end{Bmatrix} \quad (2.9)$$

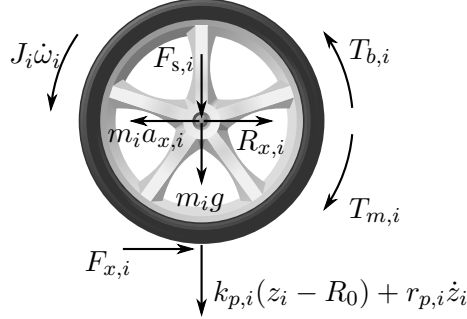


Figure 2.2: Forces applied on i -th wheel

2.1.2 Virtual work on chassis

The Lagrangian component of active forces on vehicle car body reads

$$Q_b = \left\{ \begin{array}{l} \sum_{i=1}^4 \tilde{F}_{xi} + F_{wind,x} \\ \sum_{i=1}^4 \tilde{F}_{yi} + F_{wind,y} \\ \sum_{i=1}^4 F_{si} + F_{wind,z} - m_b g \\ \sum_{i=1}^4 F_{si} c_i + \sum_{i=1}^4 T_{wi} \sin \delta_i + m_b g h_{RC} \varphi + M_{wind,x} \\ - \sum_{i=1}^4 T_{wi} \cos \delta_i - F_{wind,x} h_{PC} - m_b g x_{RC} + M_{wind,y} \\ - \sum_{i=1}^4 \tilde{F}_{xi} c_i + \sum_{i=1}^4 \tilde{F}_{yi} l_i + \sum_{i=1}^4 M_{zi} + M_{wind,z} \end{array} \right\} \quad (2.10)$$

where

$$\begin{aligned} \tilde{F}_{xi} &= F_{xi} \cos \delta_i - F_{yi} \sin \delta_i \\ \tilde{F}_{yi} &= F_{xi} \sin \delta_i + F_{yi} \cos \delta_i \end{aligned} \quad (2.11)$$

2.1.3 Wheels dynamics

Dynamics equation of unsprung masses for vertical displacement

$$m_i \ddot{z}_i + r_{pi} \dot{z}_i + k_{pi}(z_i - R_0) = -F_{si} - m_i g \quad (2.12)$$

while rotation about hub axis, neglecting gyroscopic effects, reads

$$J_i \dot{\omega}_i = T_{wi} - M_{yi} - F_{xi} z_i \quad (2.13)$$

where M_{yi} is rolling resistance torque.

In simulations the unsprung masses and wheel inertia are increased in order to account for the presence of IWM.

2.1.4 Suspensions forces

Force on suspension uses lookup table to account for nonlinearities (damping, boundstops, etc) and suspension elasto-kinematic behaviour. Each suspension spring is supposed to be positioned in correspondence of tyres contact points.

The force of the i -th suspension is

$$F_{si} = -(k_i \Delta L_i + r_i \dot{\Delta L}_i) - (k_{\phi,j} \Delta L_{RL,j} + r_{\phi,j} \dot{\Delta L}_{RL,j}) \quad (2.14)$$

where k_i and r_i are the stiffness and the damping coefficient of the i -th suspension spring and damper; ΔL_i is the elongation of the i -th suspension; $k_{\phi,j}$ and $r_{\phi,j}$ are the stiffness and the damping coefficients of the j -th axle roll bar expressed in N/m and Ns/m while $\Delta L_{RL,j}$ is the difference between right and left suspension elongations on the j -th axle.

The i -th suspension elongation is

$$\Delta L_i = z - (h_G - R_r) + \varphi c_i + \vartheta(x_{PC} - l_i) - z_i \quad (2.15)$$

while

$$\Delta L_{RL,j} = \Delta L_{jR} - \Delta L_{jL} \quad (2.16)$$

2.2 Tyre model

Tyres are modelled according to combined slip MF-Tyre model ([30]).

$$F_i = D_i \sin(C_i \arctan\{B_i x - E_i(B_i x - \arctan(B_i x))\}) \quad (2.17)$$

where x is slip ratio κ for longitudinal forces and slip angle α for lateral forces. B , C , D and E are coefficient determined by experimental test on tyre.

MF-Tyre model used accounts for combined slip effect, vertical load dependency and for relaxation length. In Appendix A detailed equation of the model are reported.

2.2.1 Slips and slip angles calculation

Slip ratio are calculated as follows

$$\kappa_i = 1 - \frac{\omega_i z_i}{v_{xi}} \quad (2.18)$$

where v_{xi} is the longitudinal velocity of the hub in wheel reference frame which can be computed as

$$v_{xi} = (v_x - c_i \dot{\psi}) \cos \delta_i + (v_y + l_i \dot{\psi}) \sin \delta_i \quad (2.19)$$

Slip angles are instead calculated as

$$\alpha_i = \arctan \left(\frac{v_y + l_i \dot{\psi}}{v_x - c_i \dot{\psi}} \right) - \delta_i \quad (2.20)$$

2.3 In-Wheel motors model

The modelled vehicle is driven by four in-wheel motors which are modelled from a mechanical point of view. The torque versus speed characteristic both for driving and braking is taken into account, motor characteristic is shown in Figure 2.3. It represent the characteristic curve of IWM produced by Protean Electric and whose main data are summarised in Table 2.1. Dimensions of IWM are suitable for 18" wheels which are supported by the considered vehicle.

Motor energy consumption and regeneration is taken into account considering motors and power electronics efficiency. The power consumption (P_e) of each motor is evaluated as

$$P_e = T_m \omega_m + k_m T_m^2 \quad (2.21)$$

where T_m and ω_m are respectively the torque and the angular speed of the motor while $k_m = 0.021 \text{ (Nms)}^{-1}$ is a constant that includes power electronics and motor copper losses [25].

2.4 Driver model

A path follower driver model was developed in order to perform close loop manoeuvres [2]. The driver is a PD controller with position and yaw feedback. Making reference to Figure 2.4, the steering wheel angle is evaluated as

$$\delta_{SW} = \sum_{i=1}^2 (k_{p,d,i} \varepsilon_d(l_i) + k_{d,d,i} \dot{\varepsilon}_d(l_i)) + \sum_{i=1}^2 (k_{p,\psi,i} \varepsilon_\psi(l_i) + k_{d,\psi,i} \dot{\varepsilon}_\psi(l_i)) \quad (2.22)$$

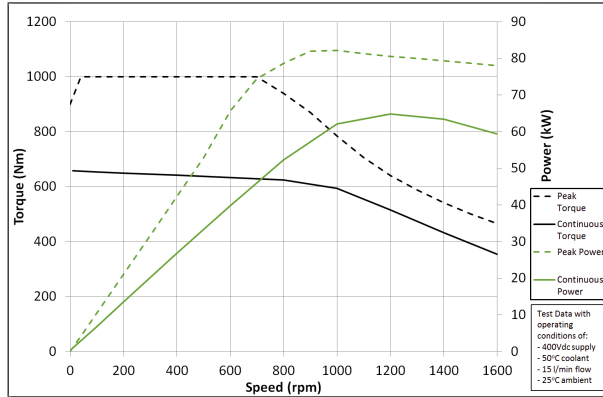


Figure 2.3: IWM characteristic by Protean Electric

Table 2.1: IWM data

Peak power @ 400 Vdc	[kW]	75
Continuous output power @ 400 Vdc	[kW]	54
Peak output torque	[Nm]	1000
Continuous output torque	[Nm]	650
Nominal input voltage	[Vdc]	200-400
Maximum speed @ 400 Vdc	[rpm]	1400
Diameter	[mm]	420
Width	[mm]	115
Total motor mass	[kg]	34

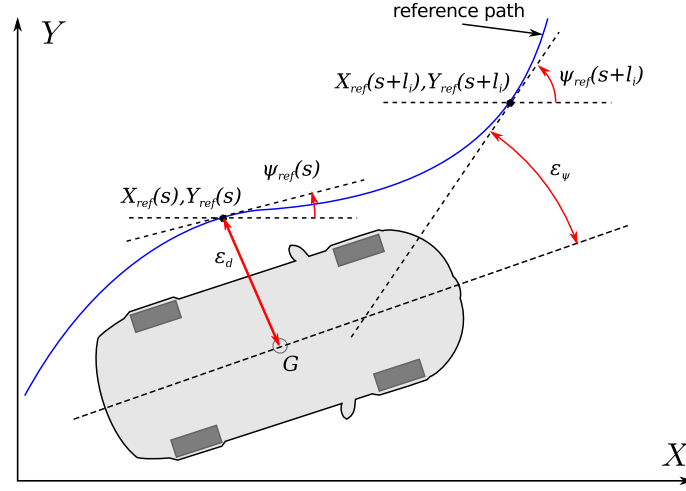


Figure 2.4: Driver used to perform close loop manoeuvres

where $k_{p,d,i}$ and $k_{d,d,i}$ are respectively the proportional and the derivative gains on distance error ε_d while $k_{p,\psi,i}$ and $k_{d,\psi,i}$ are respectively the proportional and the derivative gains on yaw angle error ε_ψ of the i -th preview point.

Two error functions are considered to calculate the steering-wheel angle, one is the error of cog position with respect to the desired trajectory

$$\varepsilon_d(l_i) = \sqrt{(X_{G,ref}(s+l_i) - X_G)^2 + (Y_{G,ref}(s+l_i) - Y_G)^2} \quad (2.23)$$

where s is the curvilinear abscissa.

The second error function is a yaw angle error and it is used to maintain the vehicle aligned with the desired trajectory

$$\varepsilon_\psi(l_i) = \psi_{ref}(s+l_i) - \psi \quad (2.24)$$

Each error is evaluated in correspondence of two preview distances l_i which are a function of vehicle speed V and longitudinal acceleration a_x

$$l_i = Vt_i + \frac{1}{2}a_x t_i^2 \quad (2.25)$$

t_i are the driver response time that can be tuned in order to simulate a different driver behaviour.

Table 2.2: *Vehicle data used for vehicle model validation which is a commercial segment D passengers car.*

parameter	description	unit	value
c_f	front axle half-track width	m	0.757
c_r	rear axle half-track width	m	0.748
h_G	vehicle cog height from ground	m	0.58
l	vehicle wheelbase length	m	2.70
l_f	distance of vehicle c.o.g from front axle	m	1.16
l_r	distance of vehicle c.o.g from rear axle	m	1.54
m	vehicle overall mass	kg	1681

2.5 Model validation

The presented vehicle model has been validated thanks to Mechanical Department facilities. Experimental data collected by instrumented segment D passengers car whose main data are reported in table 2.2. The car is equipped with a 6 dof inertia platform, optical velocity measurement sensor, CAN-BUS data reader, Dynamo-metric HUB on FL wheel.

The simulation takes as input the measured steering wheel angle while a PID controller generates driving/braking torques on wheels in order to track the measured longitudinal velocity. Simulation results have been compared to experimental data as shown in figure 2.5 where following quantities are reported:

- Steering wheel angle δ_{SW} ;
- longitudinal velocity v_x ;
- longitudinal and lateral acceleration a_x and a_y ;
- yaw rate $\dot{\psi}$;
- sideslip angle β ;
- vertical and lateral force on front left wheel F_{zFL} and F_{yFL} .

These data have been collected in a normal driving condition in a typical city path.

2.5. MODEL VALIDATION

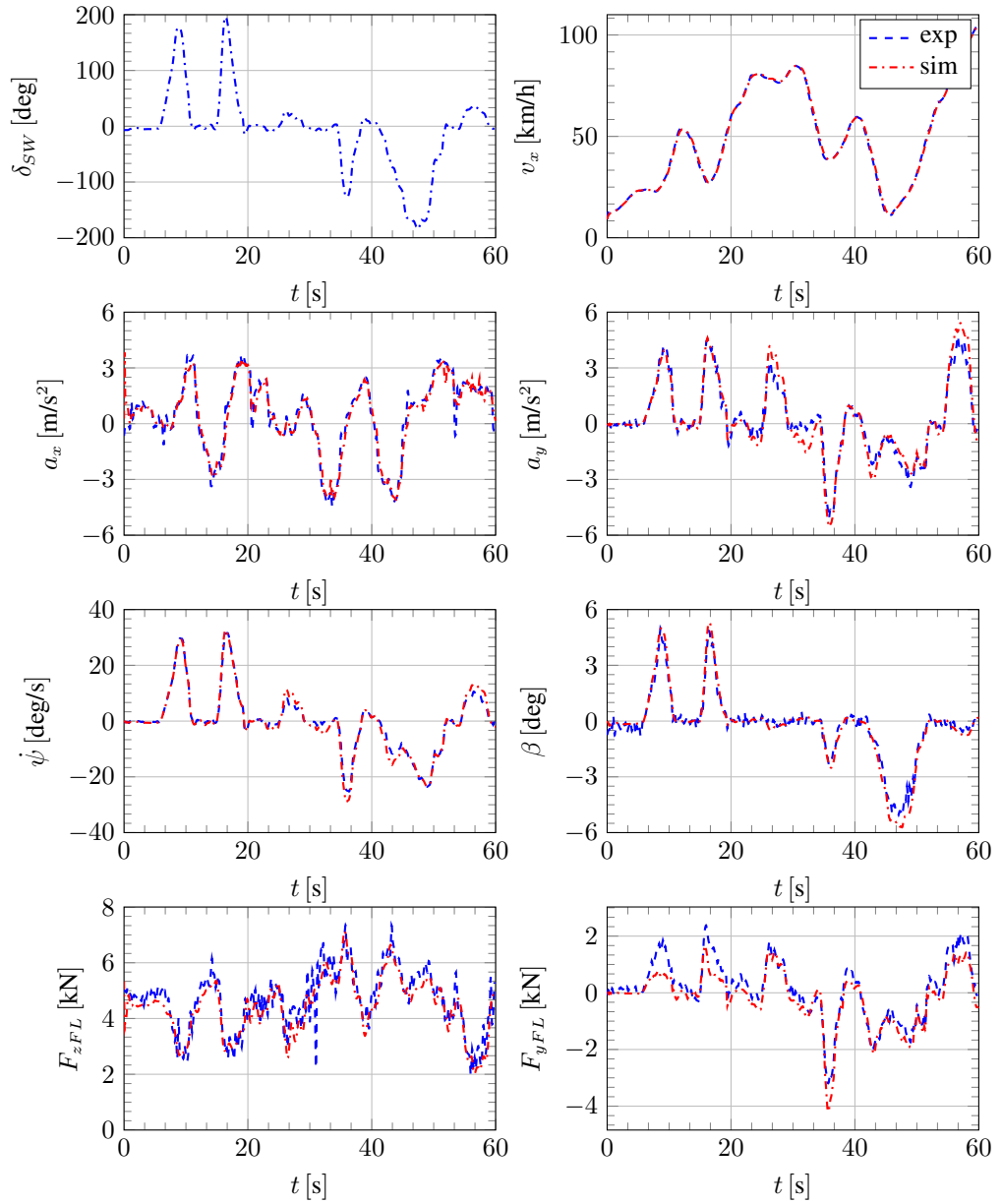


Figure 2.5: Comparison of experimental and numerical data.

CHAPTER 3

Vehicle dynamics controller

IN this chapter the newly designed control strategy for vehicle lateral dynamics is presented. Before going into details of the control strategy, some consideration on torque vectoring capability in modifying vehicle lateral dynamics are presented.

Torque vectoring consists in applying driving/braking torques on wheels in order to generate a yaw moment that is summed to vehicle yaw moment due to lateral forces. In the first paragraph some quantitative considerations on the yaw moment generated by longitudinal forces are presented. In the following a detailed description of the control strategy here designed is presented. This control strategy is designed for vehicles with four independent electric motors thus the controller have the capability of independently apply driving or braking torques on each wheel.

3.1 Torque vectoring analysis

In order to understand the controller capability in modifying vehicle lateral dynamics, some consideration are here presented on the effective amount

3.1. TORQUE VECTORING ANALYSIS

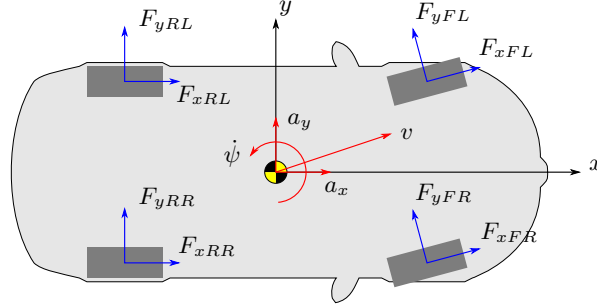


Figure 3.1: *Four contact point vehicle model*

of yaw moment that can be developed by applying a torque on one single wheel of the vehicle. Considering Figure 3.1, the maximum applicable yaw moment by the i -th wheel of the vehicle is the sum of the yaw moment generated by lateral force and longitudinal force.

However it must be considered that, when a driving/braking torque is demanded, the longitudinal force increase (in amplitude) and this affects the lateral force according to the friction circle diagram:

$$\mu_i = \sqrt{\frac{F_{xi}^2 + F_{yi}^2}{F_{zi}^2}} = \sqrt{\mu_{xi}^2 + \mu_{yi}^2} \quad (3.1)$$

The total yaw moment generated by the i -th wheel, neglecting steer angle for sake of simplicity, can thus be written as

$$M_{zi} = F_{xi}c_i + F_{yi}l_i \quad (3.2)$$

where l_i and c_i are respectively the x and y coordinates of the i -th wheel in the cog reference frame. Expressing lateral force F_{yi} as function of lateral friction coefficient μ_{yi} and vertical load F_{zi} and considering equation (3.1) we obtain

$$M_{zi} = F_{xi}c_i + \sqrt{\mu_i^2 - \frac{F_{xi}^2}{F_{zi}^2}} F_{zi}l_i \quad (3.3)$$

the maximum yaw moment M_{zi} due to longitudinal force is obtained through

$$\max(M_{zi}) \Rightarrow \frac{\partial M_{zi}}{\partial F_{xi}} = 0 \quad (3.4)$$

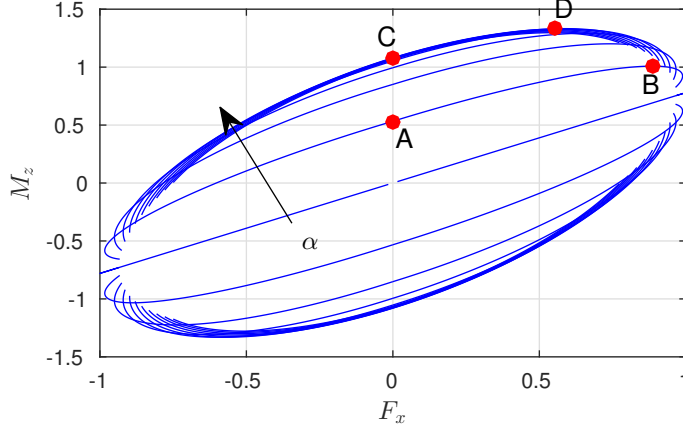


Figure 3.2: Yaw moment as function of longitudinal and lateral forces. Both have been normalized by vertical load.

which produces

$$\frac{F_{xi}}{F_{zi}} = \pm \mu \sqrt{\frac{c_i^2}{c_i^2 + l_i^2}} \quad (3.5)$$

if a 60-40% front-rear weight distribution is considered for a vehicle with a wheelbase of 2.7 m and a track width of 1.54 m, the above equation (for $\mu = 1$) gives a value of 42.9% for rear wheels and 58.0% for front wheels. If we substitute the value of F_x which maximize M_z into M_z expression we obtain

$$M_{z,max} = \mu F_z \sqrt{c_i^2 + l_i^2} \quad (3.6)$$

if compared with the yaw moment given by only maximum lateral force $M_{z,F_y} = \mu F_y l_i$ we obtain that

$$\frac{M_{z,max}}{M_{z,F_y}} = \frac{\sqrt{c_i^2 + l_i^2}}{l_i} \quad (3.7)$$

The value of this ratio is 1.23 for front wheels and 1.11 for rear wheels of the considered car. This means that longitudinal forces can considerably (up to 23% increase of yaw moment) modify lateral dynamics of the vehicle and a considerable amount of longitudinal force can be required to the tyre without reducing significantly the lateral force.

If a more complex tyre model is considered, practically same results can be obtained. Considering the following tyre model for combined slip with isotropic tyre behaviour we have that the tyre contact forces are

$$\begin{Bmatrix} F_x \\ F_y \end{Bmatrix} = \begin{Bmatrix} \sigma_x \\ \sigma_y \end{Bmatrix} \frac{\mu F_z d}{\sigma} \sin(C \arctan(B\sigma)) \quad (3.8)$$

where $\sigma = \sqrt{\sigma_x^2 + \sigma_y^2}$ and

$$\sigma_x = \begin{cases} \kappa & \text{braking} \\ \frac{\kappa}{\kappa + 1} & \text{driving} \end{cases} \quad \sigma_y = \begin{cases} \tan \alpha & \text{braking} \\ \frac{\tan \alpha}{\kappa + 1} & \text{driving} \end{cases} \quad (3.9)$$

being κ the longitudinal slip and α the slip angle. It is possible to draw the yaw moment as function of longitudinal force F_x for different value of slip angle α .

Looking at figure 3.2, it is possible to appreciate the effect of F_x on M_z . If no longitudinal forces are applied on the vehicle with a certain slip angle, smaller than slip angle corresponding to maximum lateral force, the yaw moment is the one given by point A in the figure. The maximum M_z achievable is given by point B where the increase is about 100% and it has been obtained with a longitudinal force which is about 89% of F_z . If instead we consider the lateral force developed when slip angle corresponds to the maximum lateral force we are in point C in the graph. The maximum achievable M_z is obtained in point D with an increase of 23% when F_x is 55% of F_z .

3.2 Main scheme of the controller

After having shown the potential of applying torque vectoring in controlling vehicle lateral dynamics, here the control strategy based on torque vectoring is presented. It has been designed to be applied to four independently driven vehicle, it means that each wheel can be control independently from the others.

The logic has also been applied to other powertrain layouts with proper adjustments according to the number of EMs installed on the vehicle. This extension is presented in chapter 6.

The main scheme of the controller is reported in Figure 3.3. The high level controller generates a suitable yaw moment in order to control vehicle lateral dynamics. It is made mainly of two contributions:

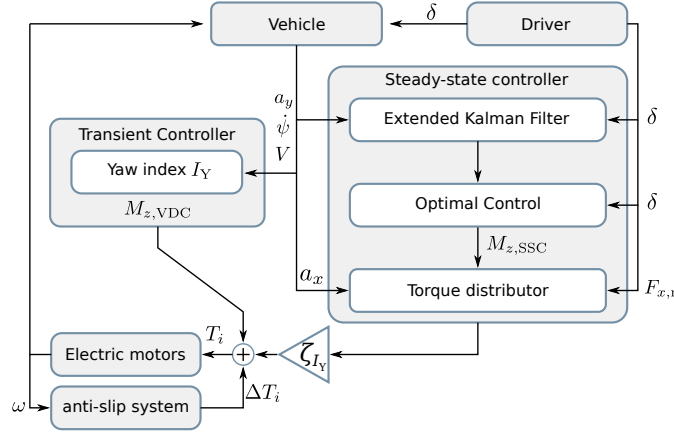


Figure 3.3: Main scheme of the controller

- a transient controller (dynamic stability control, DSC, in the following) which relies on Yaw Index I_Y which is related to the dynamic over/under-steering condition of the vehicle. Yaw index is defined as

$$I_Y = \frac{a_y}{v_x} - \dot{\psi} \quad (3.10)$$

As better explained in the following, this index is directly related to time derivative of vehicle lateral velocity.

The target of this controller is to increase vehicle stability. It is to point out that this controller doesn't need any estimation of sideslip angle and, what is more important, of friction coefficient. The only estimation required is longitudinal velocity of the vehicle which can be roughly estimated from wheels angular velocity.

- a steady-state controller (SSC) that is based on optimal control theory. The steady state controller is coupled with an Extended Kalman Filter which is used for vehicle state estimation; in particular EKF is used to estimate sideslip angle β and the friction coefficient between tyres and road μ . SSC target is to track yaw rate and sideslip angle references by generating a yaw moment.

To generate the demanded yaw moment, torque is distributed among the four wheels accounting for driver's inputs (brake and accelerator pedals) and load transfer due to acceleration.

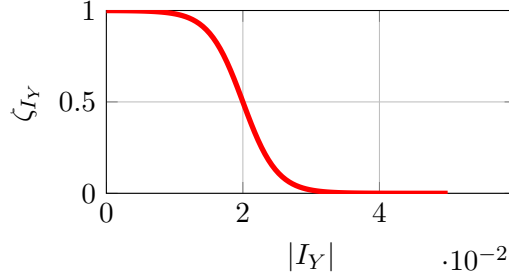


Figure 3.4: Weight coefficient for the sum of the two controller contributions.

The duty of this contribution is mainly to improve vehicle steady-state handling characteristic.

The global torques demanded at the on i -th wheel (T_i) is the weighed sum of the two contributions

$$T_i = T_{i,\text{DSC}} + \zeta_{I_Y} T_{i,\text{SSC}} \quad (3.11)$$

The weight ζ_{I_Y} cancels SSC contribution in limit handling manoeuvres. The higher the value of $|I_Y|$, the lower the value of ζ_{I_Y} according to the following function:

$$\zeta_{I_Y} = \frac{1}{2} (1 - \tanh(c_1 |I_Y| + c_2)) \quad (3.12)$$

where c_1 and c_2 are constant parameter that can be tuned by control designer according to the desired level of officiousness of the transient controller. The shape of ζ_{I_Y} is reported in figure 3.4.

At a lower level, an antislip control block prevents wheels from exceeding a given value of slip κ modulating torques on wheels.

3.3 Transient control strategy

Vehicle dynamics stability control strategy (DSC in the following) aims to enhance vehicle lateral stability in cornering condition. DSC relies on an index (I_Y) related to vehicle dynamic over/under-steering¹ behaviour and

¹The author, for sake of simplicity in explanation, adopted the oversteering term meaning that the vehicle is leaving a steady-state turning condition due to a reduction of the rear axle cornering force which generate an increase in yaw rate causing an increase of sideslip angle opposite to the

Table 3.1: Yaw index for different conditions

a_y	$\dot{\psi}$		YI	$\dot{\beta}$		$M_{z,DSC}$
+	+	$\frac{a_y}{v_x} = \dot{\psi}$	0	0	steady-state	0
+	+	$\frac{a_y}{v_x} > \dot{\psi}$	+	-	understeer	+
+	+	$\frac{a_y}{v_x} < \dot{\psi}$	-	+	oversteer	-
-	-	$\frac{a_y}{v_x} = \dot{\psi}$	0	0	steady-state	0
-	-	$\frac{a_y}{v_x} > \dot{\psi}$	-	+	understeer	-
-	-	$\frac{a_y}{v_x} < \dot{\psi}$	+	-	oversteer	+

generates a yaw moment according to the following equation

$$M_{z,DSC} = k_Y \cdot I_Y \quad (3.13)$$

where k_Y is the controller gain and I_Y is the yaw index expressed as

$$I_Y = \frac{a_y}{v_x} - \dot{\psi} \quad (3.14)$$

where a_y is the vehicle lateral acceleration, v_x is the vehicle speed and $\dot{\psi}$ is the yaw rate.

The meaning of I_Y can be easily understood considering vehicle cornering condition (see Figure 3.5). In steady-state (Figure 3.5a), yaw rate $\dot{\psi}$ is equal to the ratio between lateral acceleration a_y and vehicle speed v thus I_Y is null and no yaw moment is needed.

Instead, if the vehicle is in oversteering condition (Figure 3.5b) in a counter-clockwise turn, yaw rate is greater than a_y/v_x , thus I_Y is negative and a negative yaw moment should be applied to prevent vehicle from spinning.

On the contrary, if the vehicle is in understeering condition (Figure 3.5c) in a counter-clockwise turn, yaw rate is lower than the ratio a_y/v_x , I_Y is positive and a positive yaw moment should be applied to the vehicle to increase its yaw rate (i.e. entering the turn). Table 3.1 summarises the meaning of the Yaw Index.

DSC tries to ensure vehicle stability keeping yaw index near to zero value. This means that the controller aim is to keep the vehicle in steady-state cornering condition. This prevents an excessive increase of the sideslip

turn direction. Conversely the understeer term indicate a transient condition in which the vehicle leaves the steady-state condition due to a reduction of the front axle cornering force which makes the vehicle enlarge its trajectory

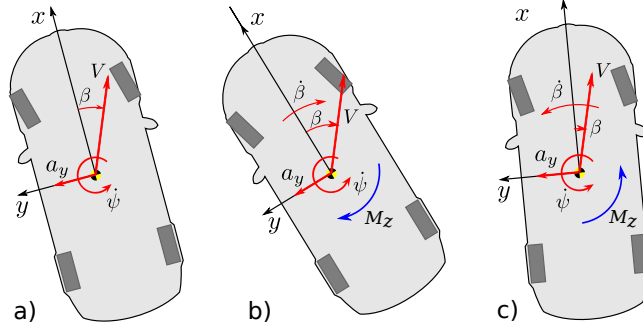


Figure 3.5: Vehicle behaviour in a) steady-state, b) oversteering and c) understeering.

angle. In fact, considering a vehicle in a turn, for small sideslip angles β , lateral acceleration can be written as

$$a_y = v_x \dot{\beta} + \dot{\psi} v_x + \dot{v} \beta \quad (3.15)$$

rearranging the equation we obtain

$$\dot{\beta} = \frac{a_y - \dot{\psi} v_x - \dot{v} \beta}{v_x} \quad (3.16)$$

if constant speed manoeuvres are considered ($\dot{v} = 0$), the yaw index equals $\dot{\beta}$

$$\dot{\beta} = \frac{a_y - \dot{\psi} v_x}{v_x} = \frac{a_y}{v_x} - \dot{\psi} = I_Y \quad (3.17)$$

This means that the control logic generates a yaw moment that prevent sideslip angle from excessive increase.

In order to avoid erroneous evaluation of I_Y in case of bank angle, thus giving a constant lateral acceleration due to the projection of gravity along vehicle y axis, the index is high pass filtered.

It is to point out that the use of yaw index as described above implies that no vehicle state estimation is needed by the control strategy. In fact neither friction and sideslip angle appear in the index formulation. This represents a big advantage since the controller can work in all conditions without the complexity and the coupling with a state observer. As already mentioned, during transients in limit handling conditions, only this controller is acting. In limit handling manoeuvres, in fact $|I_Y|$ gets big and so the weight of the SSC becomes null. This avoids lags/errors in sideslip/friction estimation.

3.3.1 Yaw moment generation

The yaw moment required by DSC ($M_{z,DSC}$) needs to be generated applying suitable longitudinal forces on wheels. Torques are thus distributed among wheels according to yaw index absolute value

$$T_{FR} = -T_{FL} = \begin{cases} \frac{M_{z,DSC}}{2c_f R_r} & \left| \frac{a_y}{v_x} \right| < |\dot{\psi}| \\ 0 & \left| \frac{a_y}{v_x} \right| > |\dot{\psi}| \end{cases} \quad (3.18)$$

$$T_{RR} = -T_{RL} = \begin{cases} 0 & \left| \frac{a_y}{v_x} \right| < |\dot{\psi}| \\ \frac{M_{z,DSC}}{2c_r R_r} & \left| \frac{a_y}{v_x} \right| > |\dot{\psi}| \end{cases} \quad (3.19)$$

where c_f and c_r are the front and rear track half width respectively and R_r is the rolling radius.

This choice is driven by the consideration that a dynamic oversteer condition can be caused by a drop of lateral force on the rear axle. If we consider the friction circle, it is better to apply longitudinal forces on the front axle in order to avoid any excessive saturation on the rear axle which will cause an increase of oversteer. The same consideration is done for understeer condition.

3.3.2 State-space behaviour of the controller

In order to assess the validity of the proposed controller by a theoretical point of view, a simple single track vehicle model is considered. The equation of the in plane motion of the vehicle reads

$$\begin{cases} \dot{v}_x = \dot{\psi}v_y + \frac{1}{m}F_{x,f} \cos \delta + \frac{1}{m}F_{x,r} - \frac{1}{m}F_{y,f} \sin \delta - \frac{1}{m}F_{res} \\ \dot{v}_y = -\dot{\psi}v_x + \frac{1}{m}F_{x,f} \sin \delta + \frac{1}{m}F_{y,f} \cos \delta + \frac{1}{m}F_{y,r} \\ \ddot{\psi} = \frac{l_f}{J}F_{x,f} \sin \delta + \frac{l_f}{J}F_{y,f} \cos \delta - \frac{l_r}{J}F_{y,r} + \frac{M_z}{J} \end{cases} \quad (3.20)$$

In order to simplify the problem for a better understanding of the results, it is here assumed that the longitudinal acceleration a_x is a given constant parameter imposed by the driver, thus the first equation reads

$$\dot{v}_x = \dot{\psi}v_y + a_x \quad (3.21)$$

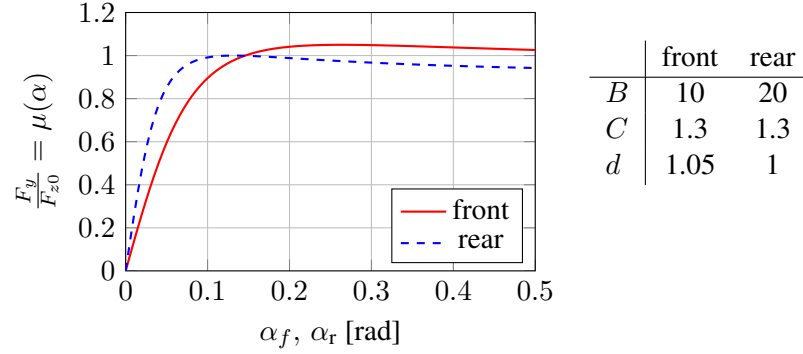


Figure 3.6: Normalised lateral forces of front and rear axle as function of slip angles.

also, the steer angle δ , which does not compare explicitly in equation (3.20) but it is necessary to calculate slips angle from which lateral contact forces depends on. Slip angles are evaluated according to the following equations

$$\begin{aligned}\alpha_f &= \delta - \arctan\left(\frac{v_y + \dot{\psi}l_f}{v_x}\right) \\ \alpha_r &= -\arctan\left(\frac{v_y - \dot{\psi}l_r}{v_x}\right)\end{aligned}\quad (3.22)$$

Lateral forces are calculate according to simplified Pacejka MF-Tyre model

$$F_y = D \sin(C \arctan(B\alpha)) \quad (3.23)$$

the shape of lateral forces is reported in figure 3.6. Here also the load transfer due to longitudinal acceleration is accounted as follows

$$\begin{aligned}F_{zf} &= mg\frac{l_r}{l} - ma_x\frac{h_G}{l} \\ F_{zr} &= mg\frac{l_f}{l} + ma_x\frac{h_G}{l}\end{aligned}\quad (3.24)$$

As suggested by many authors and in particular from [10] for the definition of vehicle fixed point and their stability only the difference between the front and rear axles normalised lateral force with respect to static load F_{z0} can be considered. In fact also the handling diagram, that is one of the most

used and powerful tool for studying vehicle dynamics behaviour, relies on the normalised lateral force $\frac{F_y}{F_{z0}} = \mu(\alpha)$. The two lateral forces presents the behaviour reported in figure 3.6. This condition is considered since it is the most critical for vehicle stability ([10],[26, Ch.5])

According to the vehicle model here presented several cases have been enquired in order to generate a phase-plane plot for different vehicle longitudinal speed v_x , for different steer angle δ and for different longitudinal acceleration a_x . For a better understanding of the phenomenon the sideslip angle β of the vehicle is used instead of the lateral speed v_y . The relationship between v (modulus of velocity vector), β and v_y and their derivatives are

$$\begin{aligned} v &= \sqrt{v_x^2 + v_y^2} \\ \beta &= \arctan\left(\frac{v_y}{v_x}\right) \\ \begin{bmatrix} \dot{v} \\ \dot{\beta} \end{bmatrix} &= \begin{bmatrix} \cos \beta & v \sin \beta \\ \sin \beta & v \cos \beta \end{bmatrix}^{-1} \begin{bmatrix} v_x \\ v_y \end{bmatrix} \end{aligned} \quad (3.25)$$

In figure 3.7 the phase plane has been drawn for straight line driving at constant longitudinal speed $v_x = 100$ km/h for different value of controller gain k_Y . As it can be noticed, the controller changes the shape of the basin of attraction of the stable fixed point in $(\beta, \dot{\psi}) = (0, 0)$ where the stream lines are straighter and makes the system to go faster to the fixed stable node. Over a certain value of k_Y the streamlines changes they shape from spirals to straight lines. This means that the damping of the system is higher and it is more difficult for state variables to leave the fixed stable node.

Figure 3.8 compare the state space plane of passive vehicle with active vehicle for a given value of v_x and k_Y for different values of steering angle. It can be seen that the controller can in fact increase the basin of attraction of the stable fixed point of the system for the range of speed considered.

3.3.3 Severe braking in turn manoeuvres

The transient controller, as it has been defined, presents some critical issue when severe braking in turn manoeuvres occurs. In fact, in these situations, the term $\dot{v}\beta$ in equation (3.16) becomes large and, since sideslip angle is not measured, the yaw index can give wrong informations on the amount and direction of the yaw moment necessary to maintain vehicle stability. In order to prevent this effect another contribution is added to the yaw mo-

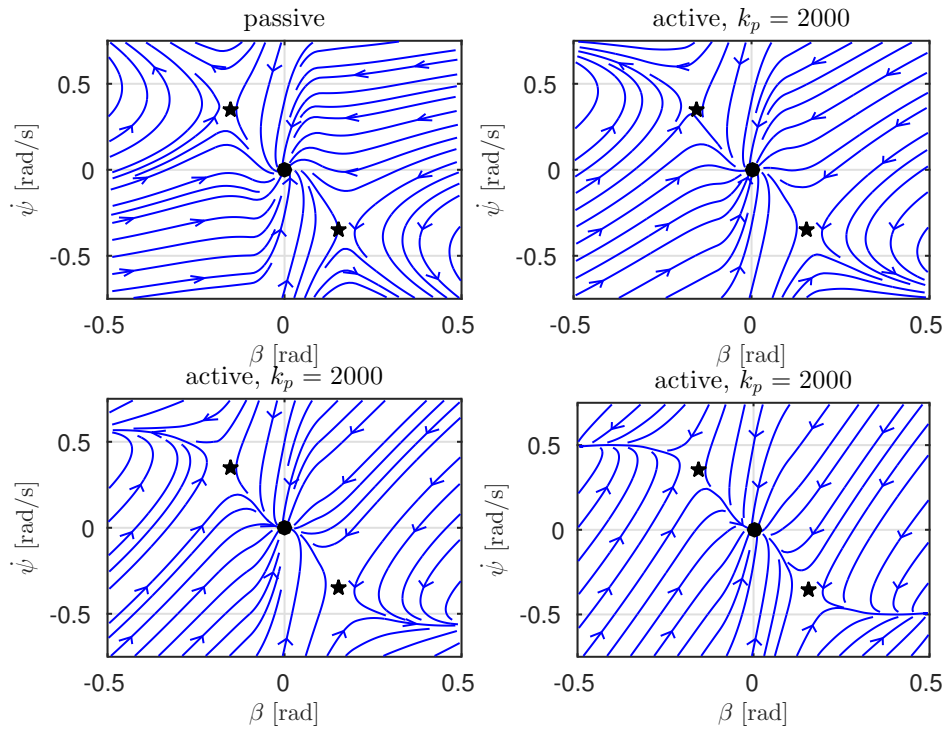


Figure 3.7: Vehicle 1. Phase plane plot for different value of the controller gain. $\delta = 0$ rad, $v_x = 100$ km/h, $a_x = 0$ m/s². ● stable node, ★ saddle node, ○ unstable node

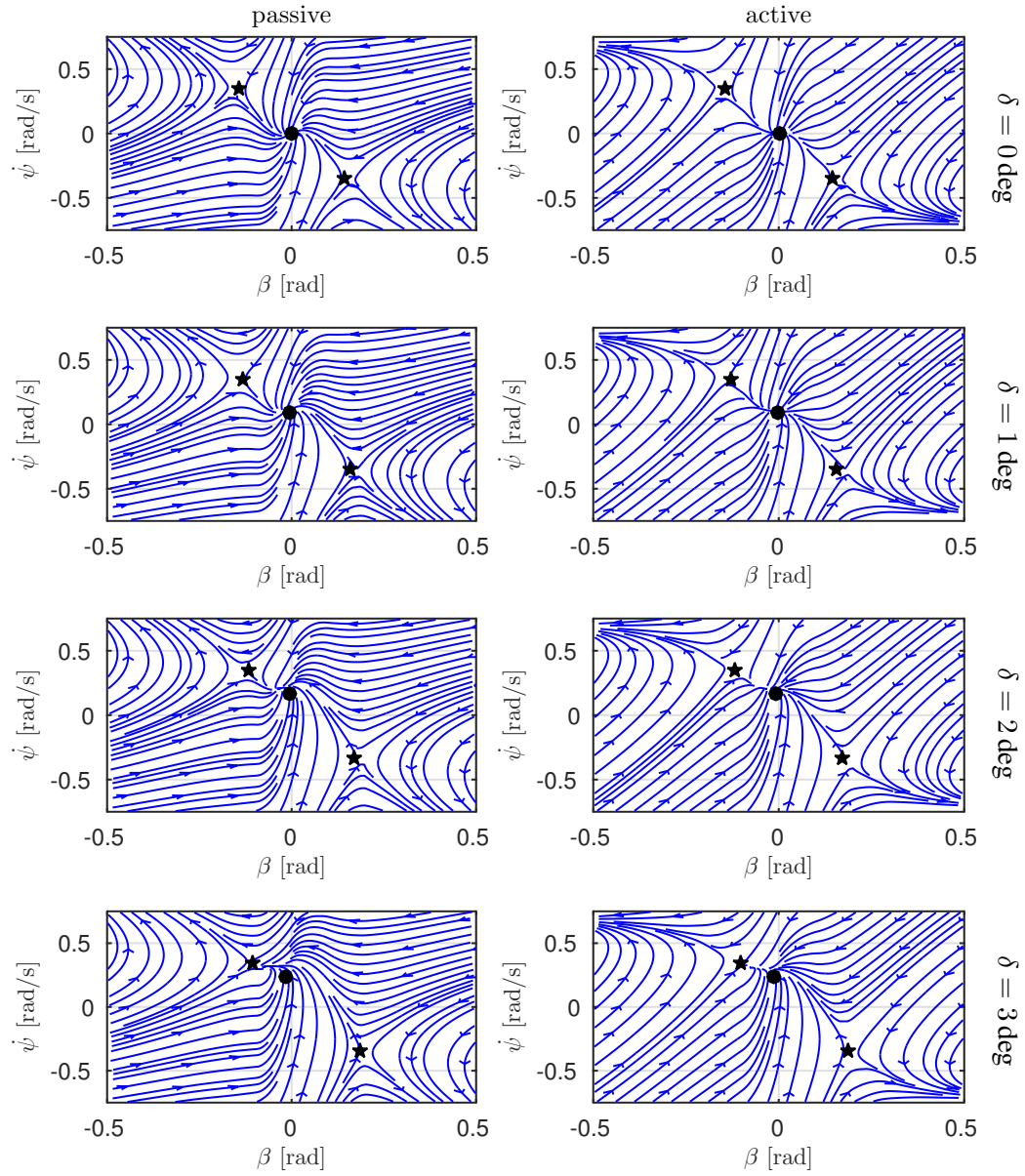


Figure 3.8: Vehicle 1, passive and active. Phase plane plot for different steer angle $\delta = 0, 1, 2,$ and 3 deg. $v_x = 100$ km/h and $a_x = 0$ m/s². ● stable node, ★ saddle node, ○ unstable node

ment required by transient controller. When this contribution is activated it overcomes the DSC contribution.

This contribution that called Brake in Turn Controller (BTC) is a proportional controller that generates a yaw moment $M_{z,BTC}$ as

$$M_{z,BTC} = -k_{BTC} \left(\ddot{\psi}_{BTC} - \ddot{\psi} \right) \quad (3.26)$$

where $\ddot{\psi}$ is yaw angular acceleration while $\ddot{\psi}_{BTC}$ is the reference yaw angular acceleration in the case that the vehicle has no sideslip angle. This expression comes from the expression of tangential and centripetal accelerations for a point moving on a constant radius path:

$$a_t = \ddot{\psi} \rho \quad (3.27)$$

$$a_c = \dot{\psi}^2 \rho \quad (3.28)$$

where ρ is the turn radius; in the same conditions, yaw rate is

$$\dot{\psi} = \frac{v_x}{\rho} \quad (3.29)$$

If sideslip angle is zero, $a_t = a_x$ and $a_c = a_y$, thus

$$\ddot{\psi}_{BTC} = \frac{a_y}{a_x} \dot{\psi}^2 \quad (3.30)$$

This control is activated on when longitudinal deceleration is grater than 2.5 m/s^2 .

In order to show the importance of this contribution, results of a brake in turn manoeuvre are here anticipated; see chapter 5 for details about the manoeuvre. Figure 3.9 reports steering wheel angle δ_{SW} , sideslip angle β , longitudinal and lateral accelerations a_x and a_y , vehicle longitudinal velocity v_x and yaw rate $\dot{\psi}$. What can be noticed is that both passive cannot accomplish the manoeuvre and the vehicle spins. Also the vehicle controlled with DSC but without BTC cannot accomplish the manoeuvre although in the beginning of the manoeuvre some improvements can be noticed: sideslip angle, yaw rate and lateral acceleration grow with low slope. The vehicle controlled with DSC with BTC instead accomplishes the manoeuvre: sideslip angle doesn't grows over 1 degree and the peak of yaw rate is limited to about 15% of the steady-state value before the braking.

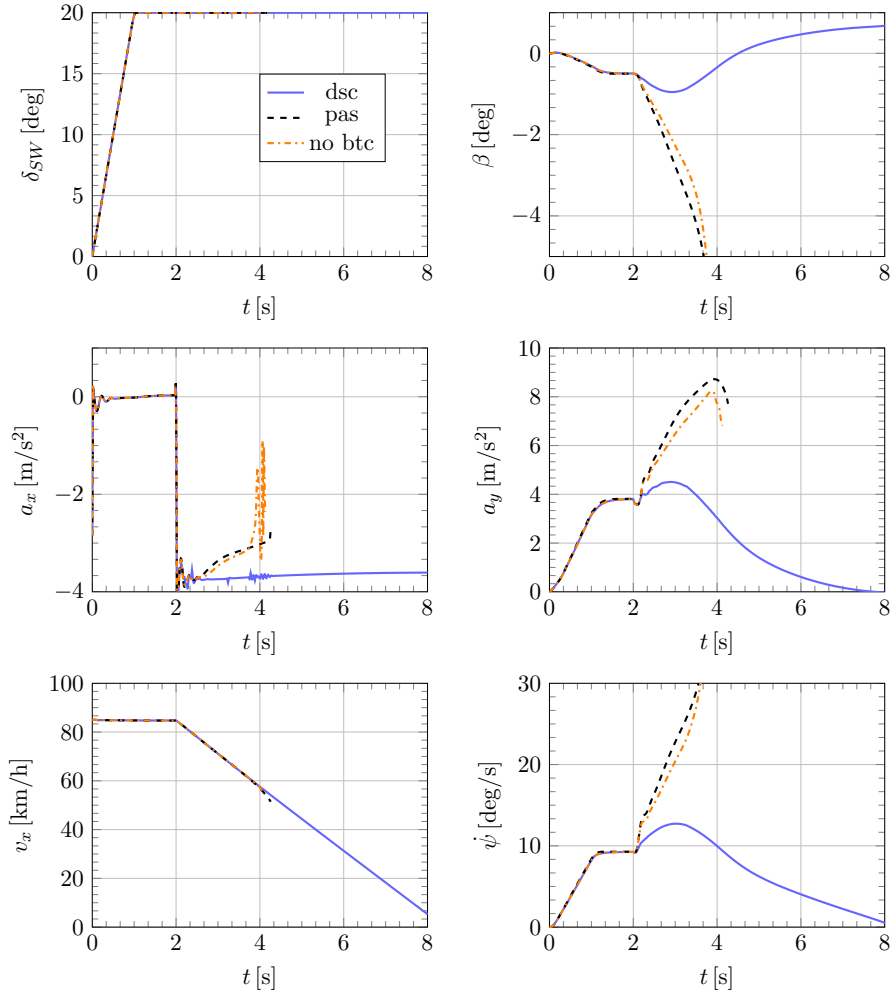


Figure 3.9: Brake in turn manoeuvre, effect of BTC.

3.4 Steady-state optimal controller

The target of the steady-state controller is to increase vehicle promptness in entering a turn and to increase the cornering performances in steady-state cornering condition. This controller has been developed according to optimal control theory based on non-linear single track vehicle model. The controller is coupled with Extended Kalman Filter (EKF) for vehicle state estimation together with friction coefficient estimation.

3.4.1 Vehicle model

The vehicle model used to design the optimal controller is a non-linear single track vehicle model whose equations of motion for lateral dynamics are

$$\begin{cases} ma_y = F_{y,f} + F_{y,r} \\ J\ddot{\psi} = F_{y,f}l_f - F_{y,r}l_r + M_z \end{cases} \quad (3.31)$$

where m and J are respectively the mass and the yaw moment of inertia of the vehicle, l_f and l_r are the distance of the vehicle centre of mass from the front and rear axle respectively, M_z is the control action, i.e. the yaw moment generated by the controller, $F_{y,f}$ and $F_{y,r}$ are the cornering contact forces of the front and rear axle which are calculated according to simplified Pacejka's MF-Tyre model

$$F_{y,j} = D_j \sin[C_j \arctan(B_j \alpha_j)] \quad (3.32)$$

with

$$D_j = \mu F_{z,j} d_j \quad (3.33)$$

$$B_j = b_j / \mu \quad (3.34)$$

where j stands for front and rear axle, μ is the overall mean friction coefficient between tyres and road, $F_{z,j}$ is the vertical load on the j -th axle. Parameters b_j , C_j and d_j are obtained by least square fitting the axles characteristics. This force formulation is a simplification of the Pacejka's model in which an additional parameter E is used. Here this simpler formulation is good enough to reproduce axles characteristic with a more simple expression to be handled in particular when calculating lateral forces derivatives.

Sideslip angles of the front and rear axle are calculated by following kinematic relationship

$$\begin{cases} \alpha_f = \arctan\left(\frac{v_y + \dot{\psi}l_f}{v_x}\right) - \delta \approx \beta + \frac{\dot{\psi}l_f}{v} - \delta \\ \alpha_r = \arctan\left(\frac{v_y - \dot{\psi}l_r}{v_x}\right) \approx \beta - \frac{\dot{\psi}l_r}{v} \end{cases} \quad (3.35)$$

Considering the kinematic relationship between lateral acceleration a_y and sideslip angle β , and considering small steering angle and small sideslip angle, we end up with the following system of equations

$$\begin{cases} \ddot{\beta} \\ \ddot{\psi} \end{cases} = \begin{cases} \frac{1}{m_v}(F_{y,f} + F_{y,r}) - \dot{\psi} - \frac{a_x}{v}\beta \\ \frac{1}{J}(F_{y,f}l_f - F_{y,r}l_r) + \frac{1}{J}M_z \end{cases} \quad (3.36)$$

$$\begin{cases} \dot{\beta} \\ \dot{\psi} \end{cases} = \begin{cases} f(\beta, \dot{\psi}, \delta) \\ g(\beta, \dot{\psi}, \delta, M_z) \end{cases}$$

In order to design an optimal controller the model of the vehicle needs to be linearised at each time step around the actual state. Calling \mathbf{x} the state of the system

$$\mathbf{x} = \begin{Bmatrix} \beta \\ \dot{\psi} \end{Bmatrix} \quad (3.37)$$

the linearised equations of the system in state space formulation are

$$\dot{\mathbf{x}} = [A]\mathbf{x} + [B]u + [C]w \quad (3.38)$$

where the two inputs of the system $u = M_z$ and $w = \delta$ have been distinguished to consider that the controller can only act on M_z while δ is imposed by the driver.

The state matrix $[A]$, the actuation matrix $[B]$ and the disturbance matrix

[C] read

$$[A] = \begin{bmatrix} a_{11} & a_{12} \\ a_{21} & a_{22} \end{bmatrix} \quad (3.39)$$

$$a_{11} = \frac{\partial f(\mathbf{x})}{\partial \beta} = \frac{1}{mv} \left(\frac{\partial F_{y,f}}{\partial \alpha_f} \frac{\partial \alpha_f}{\partial \beta} + \frac{\partial F_{y,r}}{\partial \alpha_r} \frac{\partial \alpha_r}{\partial \beta} \right) - \frac{a_x}{v} \quad (3.40)$$

$$a_{12} = \frac{\partial f(\mathbf{x})}{\partial \dot{\psi}} = \frac{1}{mv} \left(\frac{\partial F_{y,f}}{\partial \alpha_f} \frac{\partial \alpha_f}{\partial \dot{\psi}} + \frac{\partial F_{y,r}}{\partial \alpha_r} \frac{\partial \alpha_r}{\partial \dot{\psi}} \right) - 1 \quad (3.41)$$

$$a_{21} = \frac{\partial g(\mathbf{x})}{\partial \beta} = \frac{l_f}{J} \frac{\partial F_{y,f}}{\partial \alpha_f} \frac{\partial \alpha_f}{\partial \beta} - \frac{l_r}{J} \frac{\partial F_{y,r}}{\partial \alpha_r} \frac{\partial \alpha_r}{\partial \beta} \quad (3.42)$$

$$a_{22} = \frac{\partial g(\mathbf{x})}{\partial \dot{\psi}} = \frac{l_f}{J} \frac{\partial F_{y,f}}{\partial \alpha_f} \frac{\partial \alpha_f}{\partial \dot{\psi}} - \frac{l_r}{J} \frac{\partial F_{y,r}}{\partial \alpha_r} \frac{\partial \alpha_r}{\partial \dot{\psi}} \quad (3.43)$$

$$[B] = \begin{bmatrix} b_{11} \\ b_{21} \end{bmatrix} \quad (3.44)$$

$$b_{11} = \frac{\partial f(\mathbf{x})}{\partial M_z} = 0 \quad (3.45)$$

$$b_{12} = \frac{\partial g(\mathbf{x})}{\partial M_z} = \frac{1}{J} \quad (3.46)$$

$$[C] = \begin{bmatrix} c_{11} \\ c_{21} \end{bmatrix} \quad (3.47)$$

$$c_{11} = \frac{\partial f(\mathbf{x})}{\partial \delta} = \frac{1}{mv} \frac{\partial F_{y,f}}{\partial \alpha_f} \frac{\partial \alpha_f}{\partial \delta} \quad (3.48)$$

$$c_{21} = \frac{\partial g(\mathbf{x})}{\partial \dot{\psi}} = \frac{l_f}{J} \frac{\partial F_{y,f}}{\partial \alpha_f} \frac{\partial \alpha_f}{\partial \dot{\psi}} \quad (3.49)$$

where lateral forces have been derived according to the chain rule since lateral forces are functions of slip angles α and slip angles are function of state variables. Slip angles derivative with respect to state variables read:

$$\frac{\partial \alpha_f}{\partial \beta} = 1 \quad \frac{\partial \alpha_r}{\partial \beta} = 1 \quad \frac{\partial \alpha_f}{\partial \dot{\psi}} = \frac{l_f}{v} \quad \frac{\partial \alpha_r}{\partial \dot{\psi}} = -\frac{l_r}{v} \quad (3.50)$$

l_f and l_r are the distance of the vehicle cog from front and rear axle respectively.

3.4.2 Cost function and gain definition

The optimal controller requires a cost function to be minimised. If \mathbf{x}_r is the reference state, which is supposed to be constant, the quadratic cost function for controller synthesis can be written as

$$J(\mathbf{x}, t) = \int_t^{t_f} (\mathbf{x}_r - \mathbf{x})^T [Q] (\mathbf{x}_r - \mathbf{x}) + (\mathbf{u}_r - \mathbf{u})^T [R] (\mathbf{u}_r - \mathbf{u}) dt \quad (3.51)$$

where $[Q] = [Q]^T \geq 0$ is a symmetric and positive semi-definite matrix which accounts for state variables errors weight in cost definition. $[R] = [R]^T > 0$ is instead a symmetric and positive definite matrix which accounts for actuation entity.

Matrices Q and R are defined as follows

$$[Q] = \begin{bmatrix} \frac{1}{\beta_{\max}^2} & 0 \\ 0 & \frac{1}{(\mu g/v_x)^2} \end{bmatrix} \quad (3.52)$$

$$[R] = \frac{1}{(2c_f mg)^2} \quad (3.53)$$

where β_{\max} is a constant given parameter, $\mu g/v_x$ represents the maximum steady-state value of yaw rate while $2c_f mg$ is the maximum yaw moment that can be developed by longitudinal forces when each longitudinal force is equal to the vertical load on the same wheel.

If the state reference \mathbf{x}_r is a constant point in the state space ($\dot{\mathbf{x}}_r = 0$) we obtain

$$0 = [A]\mathbf{x}_r + [B]u_r + [C]w \quad (3.54)$$

calling

$$\begin{aligned} \mathbf{x}_s &= \mathbf{x}_r - \mathbf{x} \\ u_s &= u_r - u \end{aligned} \quad (3.55)$$

the cost function J becomes

$$J(\mathbf{x}, t) = \int_t^{t_f} (\mathbf{x}_s^T [Q] \mathbf{x}_s + u_s [R] u_s) dt \quad (3.56)$$

for LQR problem the minimal cost is assumed to be quadratic ($J^*(\mathbf{x}, t) = \mathbf{x}_s^T [S] \mathbf{x}_s$). $[S]$ is obtained by solving the Hamilton-Jacobi-Bellman equation that in the case of quadratic cost function is in the form of differential Riccati equation

$$[\dot{S}(t)] = -[S(t)][A] - [A]^T [S(t)] - [Q] + [S(t)][B][R]^{-1}[B]^T [S(t)] \quad (3.57)$$

we obtain the optimal control law which is given by

$$u_s = -[R]^{-1}[B]^T[S(t)]\mathbf{x}_s \quad (3.58)$$

3.4.3 References

Target of the controller is to track state references. For what concerns yaw rate reference $\dot{\psi}_r$ it is calculated according to steering wheel angle $\delta_{SW} = \tau_{SW}\delta$ (τ_{SW} is the steer ratio between the steering wheel angle and the steer angle at the wheel). Considering kinematic steering, accounting also for understeer coefficient, the steer angle reads

$$\delta = (1 + K_{US}v^2)\delta_0 \quad (3.59)$$

being δ_0 the Ackermann steering angle defined as

$$\delta_0 = \frac{l}{\rho} = \frac{l\dot{\psi}}{v} \quad (3.60)$$

where l is vehicle wheelbase and ρ the curvature radius of the trajectory. Substituting equation (3.60) into equation (3.59) and accounting for kinematic relationship between yaw rate, velocity and radius ($v = \dot{\psi}\rho$) one ends up with yaw rate of an ideal vehicle as function of speed and steering angle

$$\dot{\psi}_{lin} = \frac{v}{l(1 + K_{US}v^2)}\delta = \Psi\delta \quad (3.61)$$

This value of yaw rate must be saturated according to friction limitations

$$\dot{\psi}_{max} = \frac{\mu g}{v} \quad (3.62)$$

In order to avoid discontinuity in reference equation it has been smoothed with an exponential function. Yaw rate reference thus reads

$$\dot{\psi}_{ref} = \begin{cases} \dot{\psi}_{lin} & |\delta| \leq \delta_1 \\ \dot{\psi}_1 + (\dot{\psi}_{max} - \dot{\psi}_1) \left(1 - e^{-\frac{\Psi(|\delta| - \delta_1)}{(\dot{\psi}_{max} - \dot{\psi}_1)}}\right) & |\delta| > \delta_1 \end{cases} \quad (3.63)$$

The resulting yaw rate reference is reported in figure 3.10. Transition point from linear to non-linear behaviour ($\delta_1, \dot{\psi}_1$) can be chose by controller designer; it must be considered that δ_1 and $\dot{\psi}_1$ are related by equation (3.61): $\dot{\psi}_1 = \Psi\delta_1$.

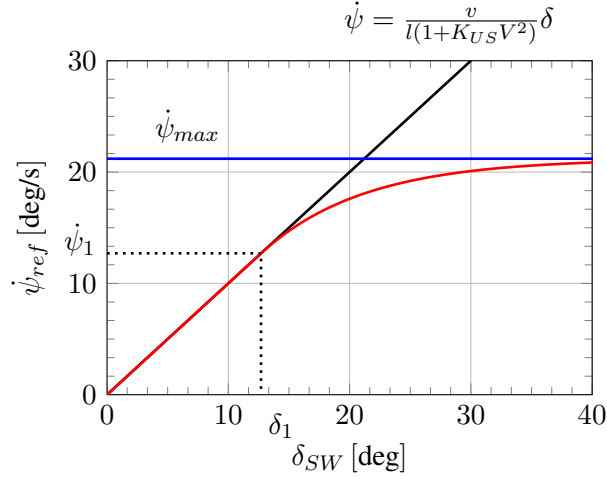


Figure 3.10: Yaw rate reference for optimal control.

Sideslip angle reference instead has been designed so that the controller acts on sideslip angle only when it becomes larger than a maximum value β_{\max} . Tracking the two state variables is in fact conflicting for the controllers in most of the cases. This reference is on purpose designed in order to avoid this conflict. The reference sideslip angle reads

$$\beta_{\text{ref}} = \beta_{\max} \tanh\left(\frac{\beta}{\beta_{\max}}\right) \quad (3.64)$$

this means that the tracking error of sideslip angle is near to zero when β is small while it becomes large when β grows over β_{\max} .

3.4.4 Torque distribution strategy

Once the total yaw moment and the required longitudinal force are calculated, these have to be generated applying differential torques on wheels. This duty is demanded to the torques distributor block whose inputs are the yaw moment M_z by steady-state controller and the total longitudinal driving/braking force F_x required by the driver. This approach was preferred to the introduction of the longitudinal equilibrium into the equations of the reference model of the LQR to directly impose constraints on the calculated longitudinal forces demand to each individual tyre so to account for

1. physical limitations (maximum longitudinal force F_x required to the most loaded tyre);
2. vehicle dynamics (oversteering/understeering tendency of the vehicle).

In torque distribution it is assumed, for sake of simplicity, that the longitudinal force $F_{x,i}$ generated on i -th wheel is equal to the ratio between the applied motor torque T_i and wheel rolling radius $R_{r,i}$

$$F_{x,i} \simeq \frac{T_i}{R_{r,i}} \quad (3.65)$$

The total longitudinal force on the vehicle due to contact forces is

$$F_x = F_{x,\text{fr}} + F_{x,\text{fl}} + F_{x,\text{rr}} + F_{x,\text{rl}} \quad (3.66)$$

instead the yaw moment is given by this equation

$$M_z = (F_{x,\text{fr}} - F_{x,\text{fl}})c_f + (F_{x,\text{rr}} - F_{x,\text{rl}})c_r \quad (3.67)$$

where c_f and c_r are respectively the front and the rear axle half track. In order to consider weight distribution of the vehicle and load transfer in driving/breaking, the ratio between longitudinal forces of the front and the rear axle is fixed to be the same as the vertical force ratio.

$$\frac{F_{x,\text{fr}} + F_{x,\text{fl}}}{F_{x,\text{rr}} + F_{x,\text{rl}}} = \frac{F_{z,\text{fr}} + F_{z,\text{fl}}}{F_{z,\text{rr}} + F_{z,\text{rl}}} = \frac{l_r - \frac{a_x}{g}h_G}{l_f + \frac{a_x}{g}h_G} = \xi_P \quad (3.68)$$

Considering equations (3.66), (3.67) and (3.68) the following linear system can be written

$$\begin{bmatrix} 1 & 1 & 1 & 1 \\ c_f & -c_f & c_r & -c_r \\ 1 & 0 & -\xi_P & 0 \\ 0 & 1 & 0 & -\xi_P \end{bmatrix} \begin{Bmatrix} F_{x,\text{fr}} \\ F_{x,\text{fl}} \\ F_{x,\text{rr}} \\ F_{x,\text{rl}} \end{Bmatrix} = \begin{Bmatrix} F_x \\ M_z \\ 0 \\ 0 \end{Bmatrix} \quad (3.69)$$

solving the system, longitudinal forces on wheels can be obtained

$$\begin{cases} F_{x,\text{fr}} = \frac{\xi_p}{2(1 + \xi_p)} F_x + \frac{\xi_p}{\xi_p c_f + c_r} M_z \\ F_{x,\text{fl}} = \frac{\xi_p}{2(1 + \xi_p)} F_x - \frac{\xi_p}{\xi_p c_f + c_r} M_z \\ F_{x,\text{rr}} = \frac{1}{2(1 + \xi_p)} F_x + \frac{1}{\xi_p c_f + c_r} M_z \\ F_{x,\text{rl}} = \frac{1}{2(1 + \xi_p)} F_x - \frac{1}{\xi_p c_f + c_r} M_z \end{cases} \quad (3.70)$$

then torques demanded to the wheels are

$$\begin{cases} T_{x,fr} \\ T_{x,fl} \\ T_{x,rr} \\ T_{x,rl} \end{cases} = \begin{cases} F_{x,fr} R_{r,fr} \\ F_{x,fl} R_{r,fl} \\ F_{x,rr} R_{r,rr} \\ F_{x,rl} R_{r,rl} \end{cases} \quad (3.71)$$

where $R_{r,i}$ is the rolling radius of the i -th wheel.

3.4. STEADY-STATE OPTIMAL CONTROLLER

CHAPTER 4

Vehicle state estimation

WHEN controlling vehicle dynamics some quantities are needed to the controller. Some of these quantities can be measured with cheap sensors: e.g. longitudinal and lateral accelerations, yaw rate and wheels angular velocities about hubs axes. Other quantities instead cannot be measured by cheap sensors or simply cannot be measured at all: thus they need to be estimated. In vehicle dynamics this is the case of sideslip angle which can be measured only with costly optical speed sensors and friction coefficient which can only be measured with dedicated .

4.1 Vehicle speed estimation

Vehicle speed is estimated according to a fuzzy logic which associates a weight w_i to the measured angular speed of each wheel about hub axis and measured longitudinal acceleration a_x .

The vehicle longitudinal speed is thus calculated as a weighted sum of

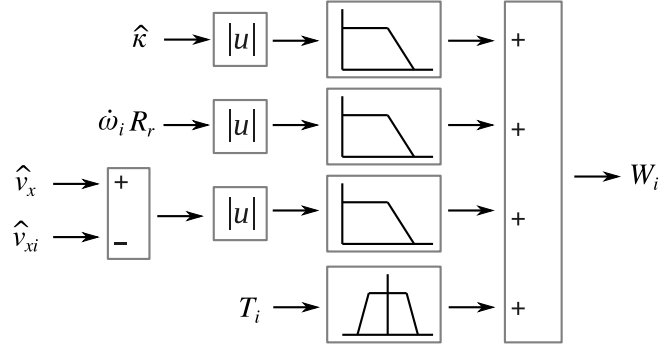


Figure 4.1: Fuzzy weight of speed estimation for wheel speed.

all wheels speed and acceleration integration

$$\hat{v}_x = \frac{\sum_i W_i v_{xi} + W_{a_x} v_{a_x}}{\sum_i W_i + W_{a_x}} \quad (4.1)$$

Weight W_i are calculated by fuzzy rules based on the following inputs:

- torque applied on each wheel: T_i ;
- slip ratio for each wheel which is estimated as

$$\hat{\kappa} = \frac{T_i - J_i \dot{\omega}}{R_r C_\kappa} \quad (4.2)$$

C_κ is the slip stiffness defined as $\left(\frac{\partial F_{x,i}}{\partial \kappa}\right)_{\kappa=0}$ for pure slip condition;

- absolute value of wheel peripheral acceleration $A_{r_i} = R_r \dot{\omega}_i$.
- absolute value of the difference between vehicle speed estimated by the i -th wheel and actual estimated value of vehicle speed: $e_i = \hat{v}_{xi} - \hat{v}_x$, where

$$\hat{v}_{xi} = \frac{\omega_i R_r}{\cos \delta_i} + c_i \dot{\psi} - l_i \dot{\psi} \tan \delta_i \quad (4.3)$$

δ_i is the wheel steer angle, l_i and c_i are the coordinate of the i -th wheel in vehicle moving reference frame.

Each variable is fuzzyfied by means of trapezoidal membership functions that range from 0, which means that the wheel is slipping and cannot

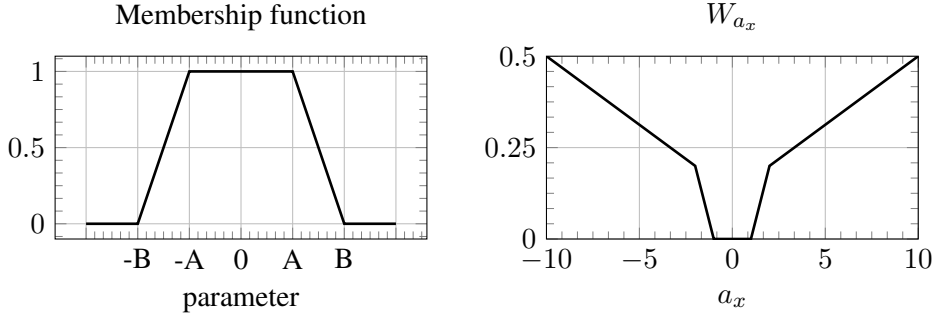


Figure 4.2: Wheels membership function and acceleration weight function for vehicle speed estimation.

be accounted for vehicle speed evaluation, to 1, which means the wheel speed can be considered reliable for vehicle speed evaluation. The shape of membership functions is reported in Figure 4.2 while their boundary values are reported in table 4.1.

For what concerns longitudinal acceleration, it is integrated in time in order to obtain a speed estimation:

$$\hat{v}_{a_x} = \hat{v}_x(t = t^*) + \int_{t^*}^{t-t^*} a_x dt \quad (4.4)$$

To avoid numerical drifting of the integration due to measurement noise, the integrator starts only when longitudinal acceleration is greater than a certain value ($t^* = t(|a_x| > 1 \text{ m/s}^2)$). The weight W_{a_x} of the speed estimation due to longitudinal acceleration integration is a function of a_x itself as reported in Figure 4.2. W_{a_x} grows from 0.2 to 0.5 when longitudinal acceleration ranges from 1 to 10 m/s^2 while it is zero when $|a_x| < 1 \text{ m/s}^2$.

Figure 4.3 reports two examples of estimator performances in a straight line braking manoeuvre and in a double lane change manoeuvre. In pure

Table 4.1: Membership functions values for vehicle speed estimation.

parameter	lower bound (point A)	upper bound (point B)
slip $\hat{\kappa}$	3 %	8 %
peripheral acceleration $\dot{\omega}R_r$	9 m/s^2	25 m/s^2
speed difference $\hat{v}_{xi} - \hat{v}_x$	15 km/h	25 km/h
torque T_i	1500 Nm	2000 Nm

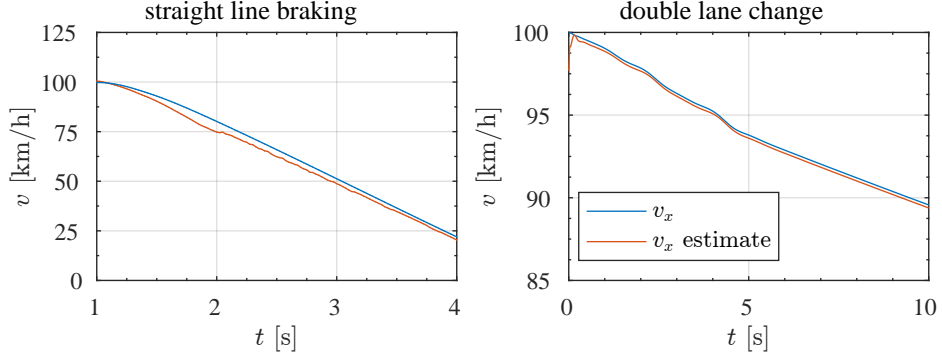


Figure 4.3: Vehicle speed estimation. Straight line braking and double lane change manoeuvres.

braking condition the maximum estimation error is about 7% while the mean error is 1.1%. In double lane change manoeuvre the maximum error is lower than 0.3% and the mean error is 0.2%.

4.2 Sideslip angle and friction coefficient

Friction coefficient and sideslip angle are needed by steady-state controller. Sideslip angle could be measured with costly sensors like optical speed sensors which measure vehicle velocity with respect to the ground along vehicle x and y axes. This sensor is not cheap and cannot be mounted on a commercial vehicle. Thus sideslip angle needs to be estimated. Friction coefficient is instead also difficult to be measured since it requires an *ad hoc* experimental setup.

The idea is to estimate both quantities through the use of an Extended Kalman Filter [4]. The estimator is based on the non-linear single track vehicle model described by following equations of motion

$$\begin{cases} m\dot{v}_y = -m\dot{\psi}v_x + F_{x,f}\sin\delta + F_{y,f}\cos\delta + F_{y,r} \\ J_z\ddot{\psi} = (F_{x,f}\sin\delta + F_{y,f}\cos\delta)l_f - F_{y,r}l_r + M_z \end{cases} \quad (4.5)$$

where δ is the steer angle of front wheels, M_z is the yaw moment required by the lateral dynamics controller. Also $F_{x,f}$, the longitudinal force of the front axle, is considered a known input since it can be calculated as the sum of left and right wheels torques T_i multiplied by the rolling radius of wheels.

Both the inputs are taken from the previous time instant. Longitudinal velocity v_x and steer angle δ are given inputs to the estimator.

Cornering forces of front and rear axles are introduced by means of three parameters Pacejka tyre model

$$F_{y,j} = D_j \sin [C_j \arctan (B_j \alpha_j)] \quad (4.6)$$

where j stands for front and rear, while parameters are defined as

$$\begin{aligned} D_j &= \mu F_{zj} d_j \\ B_j &= \frac{b_j}{\mu} \end{aligned} \quad (4.7)$$

thus lateral forces are functions of slip angles α_j , which depends on steer angle δ and vehicle lateral velocity v_y (i.e. sideslip angle β),

$$\begin{cases} \alpha_f = \arctan \left(\frac{v_y + \dot{\psi} l_f}{v_x} \right) - \delta \\ \alpha_r = \arctan \left(\frac{v_y - \dot{\psi} l_r}{v_x} \right) \end{cases} \quad (4.8)$$

and on friction coefficient between tyres and road μ . Here an overall mean friction coefficient is considered, it is assumed to be the same for all the tyres. Vertical forces on axles are evaluated according to the following equations

$$\begin{aligned} \hat{F}_{z,f} &= mg \frac{l_r}{l} - ma_x \frac{h_G}{l} \\ \hat{F}_{z,r} &= mg \frac{l_f}{l} + ma_x \frac{h_G}{l} \end{aligned} \quad (4.9)$$

where load transfer due to longitudinal acceleration a_x is considered.

The non linear equations (4.5) of the vehicle model can be rewritten in compact form as

$$\begin{cases} \dot{\mathbf{z}}(t) = \begin{cases} \dot{\mathbf{x}}(t) \\ \dot{\mu}(t) \end{cases} = \begin{bmatrix} \mathbf{g}(\mathbf{x}(t), \mathbf{u}(t), \mu(t)) \\ 0 \end{bmatrix} + \begin{bmatrix} \mathbf{w}(t) \\ w_\mu(t) \end{bmatrix} \\ \mathbf{y}(t) = \mathbf{h}(\mathbf{x}(t), \mathbf{u}(t), \mu(t)) + \mathbf{v}(t) \end{cases} \quad (4.10)$$

where g refers to eq (4.5) while the friction coefficient μ is introduced as a state and modelled as Gaussian white noise: i.e. it is assumed that there is

no relationship between μ and its time derivative $\dot{\mu}$. In eq. (4.10), \mathbf{w} and \mathbf{v} are the process and the measurement noises, \mathbf{z} is the augmented state vector,

$$\mathbf{z} = \begin{Bmatrix} \mathbf{x} \\ \mu \end{Bmatrix} \quad (4.11)$$

which includes the vehicle model state vector \mathbf{x}

$$\mathbf{x} = \{v_y \quad \dot{\psi}\}^T \quad (4.12)$$

and the friction coefficient μ (as already mentioned).

\mathbf{u} is the input vector containing the steer angle δ , the vehicle speed v_x , longitudinal force $F_{x,f}$ required by controller and the yaw moment M_z generated by controller

$$\mathbf{u} = \{\delta \quad v_x \quad F_{x,f} \quad M_z\}^T \quad (4.13)$$

and \mathbf{y} is the measurement vector

$$\mathbf{y} = \left\{ \frac{a_y}{g} \quad \dot{\psi} \quad \frac{\hat{F}_{yf}}{F_{zf0}} \quad \frac{\hat{F}_{yr}}{F_{zr0}} \right\}^T \quad (4.14)$$

where lateral acceleration a_y has been normalized dividing by gravity g , and the estimated lateral forces (F_{yf} and F_{yr}) have been normalized dividing by static vertical load of respective axle (F_{zf0} and F_{zr0}). This is made in order to reduce possible numerical issue associated with quantities of different order of magnitude. Axles cornering forces are not measured but estimated based on the measured lateral acceleration

$$\hat{F}_{yf} = ma_y \frac{l_r}{l} \quad \hat{F}_{yr} = ma_y \frac{l_f}{l} \quad (4.15)$$

The introduction of the estimates of the cornering forces into the measurements vector allows to speed up the estimation of the friction coefficient.

The following Extended Kalman Filter (EKF) can thus be written

$$\begin{cases} \dot{\hat{\mathbf{z}}}_k &= \mathbf{f}(\hat{\mathbf{z}}_{k-1}, \hat{\mu}_{k-1}) + G(\mathbf{y} - \hat{\mathbf{y}}_{k-1}) \\ \hat{\mathbf{y}} &= \mathbf{h}(\hat{\mathbf{z}}, \mathbf{u}) \end{cases} \quad (4.16)$$

where, referring to eq. (4.10), $\mathbf{f} = \{\mathbf{g} \quad 0\}^T$, G is the gain matrix that is obtained as

$$G = KC^T R^{-1} \quad (4.17)$$

K is the matrix that solves the optimal problem. Minimizing the following performance index

$$J = \int_0^t (\hat{\mathbf{z}} - [C]\mathbf{y})^T [Q] (\hat{\mathbf{z}} - [C]\mathbf{y}) dt \quad (4.18)$$

the solution is obtained by means of Differential Riccati Equation

$$\dot{K} = AK - KC^T R^{-1} CK + Q + KA^T \quad (4.19)$$

Matrices Q and R are respectively the process and the measurements noise matrices. They are defined as

$$[Q] = \begin{pmatrix} q_1 & 0 & 0 \\ 0 & q_2 & 0 \\ 0 & 0 & q_3 \end{pmatrix} \quad (4.20)$$

$$[R] = \begin{pmatrix} r_1 & 0 & 0 & 0 \\ 0 & r_2 & 0 & 0 \\ 0 & 0 & r_3 & 0 \\ 0 & 0 & 0 & r_4 \end{pmatrix} \quad (4.21)$$

where q_1 , q_2 and q_3 are the process variance due to actuations noise. Values of q can be obtained according to expected maximum variation values of $\dot{\psi}$, β and μ :

$$q_1 = \frac{1}{\Delta \dot{\psi}_{\max}^2} \quad q_2 = \frac{1}{\Delta \beta_{\max}^2} \quad q_3 = \frac{1}{\Delta \mu_{\max}^2} \quad (4.22)$$

r_1 , r_2 , r_3 and r_4 are obtained calculating the measurements variance (σ^2) in static condition of the vehicle.

Matrices A and C are respectively the state and the measurements matrices which are obtained linearising the system about the actual state \mathbf{z}_k and \mathbf{u}_k

$$A_k = \left. \frac{\partial \mathbf{f}(\mathbf{z}, \mathbf{u})}{\partial \mathbf{z}} \right|_{\mathbf{z}_k, \mathbf{u}_k} = \begin{bmatrix} \frac{\partial \dot{v}_y}{\partial v_y} & \frac{\partial \dot{v}_y}{\partial \dot{\psi}} & \frac{\partial \dot{v}_y}{\partial \dot{\mu}} \\ \frac{\partial \dot{\psi}}{\partial v_y} & \frac{\partial \dot{\psi}}{\partial \dot{\psi}} & \frac{\partial \dot{\psi}}{\partial \dot{\mu}} \\ \frac{\partial \dot{\mu}}{\partial v_y} & \frac{\partial \dot{\mu}}{\partial \dot{\psi}} & \frac{\partial \dot{\mu}}{\partial \dot{\mu}} \end{bmatrix} \quad (4.23)$$

$$C_k = \left. \frac{\partial \mathbf{h}(\mathbf{z}, \mathbf{u})}{\partial \mathbf{z}} \right|_{\mathbf{z}_k, \mathbf{u}_k} = \begin{bmatrix} \frac{1}{g} \frac{\partial a_y}{\partial v_y} & \frac{1}{g} \frac{\partial a_y}{\partial \dot{\psi}} & \frac{1}{g} \frac{\partial a_y}{\partial \dot{\mu}} \\ \frac{\partial \dot{\psi}}{\partial v_y} & \frac{\partial \dot{\psi}}{\partial \dot{\psi}} & \frac{\partial \dot{\psi}}{\partial \dot{\mu}} \\ \frac{1}{F_{zf0}} \frac{\partial F_{yf}}{\partial v_y} & \frac{1}{F_{zf0}} \frac{\partial F_{yf}}{\partial \dot{\psi}} & \frac{1}{F_{zf0}} \frac{\partial F_{yf}}{\partial \dot{\mu}} \\ \frac{1}{F_{zr0}} \frac{\partial F_{yr}}{\partial v_y} & \frac{1}{F_{zr0}} \frac{\partial F_{yr}}{\partial \dot{\psi}} & \frac{1}{F_{zr0}} \frac{\partial F_{yr}}{\partial \dot{\mu}} \end{bmatrix} \quad (4.24)$$

where

$$\frac{\partial \dot{v}_y}{\partial v_y} = \frac{1}{m} \left(\frac{\partial F_{yf}}{\partial v_y} \cos \delta + \frac{\partial F_{yr}}{\partial v_y} \right) \quad (4.25)$$

$$\frac{\partial \dot{v}_y}{\partial \dot{\psi}} = -v_x + \frac{1}{m} \left(\frac{\partial F_{yf}}{\partial \dot{\psi}} \cos \delta + \frac{\partial F_{yr}}{\partial \dot{\psi}} \right) \quad (4.26)$$

$$\frac{\partial \dot{v}_y}{\partial \mu} = \frac{1}{m} \left(\frac{\partial F_{yf}}{\partial \mu} \cos \delta + \frac{\partial F_{yr}}{\partial \mu} \right) \quad (4.27)$$

$$\frac{\partial \ddot{\psi}}{\partial v_y} = \frac{1}{J_z} \left(\frac{\partial F_{yf}}{\partial v_y} l_f \cos \delta - \frac{\partial F_{yr}}{\partial v_y} l_r \right) \quad (4.28)$$

$$\frac{\partial \ddot{\psi}}{\partial \dot{\psi}} = \frac{1}{J_z} \left(\frac{\partial F_{yf}}{\partial \dot{\psi}} l_f \cos \delta - \frac{\partial F_{yr}}{\partial \dot{\psi}} l_r \right) \quad (4.29)$$

$$\frac{\partial \ddot{\psi}}{\partial \mu} = \frac{1}{J_z} \left(\frac{\partial F_{yf}}{\partial \mu} l_f \cos \delta - \frac{\partial F_{yr}}{\partial \mu} l_r \right) \quad (4.30)$$

$$\frac{\partial \dot{\mu}}{\partial v_y} = 0 \quad (4.31)$$

$$\frac{\partial \dot{\mu}}{\partial \dot{\psi}} = 0 \quad (4.32)$$

$$\frac{\partial \dot{\mu}}{\partial \mu} = 0 \quad (4.33)$$

$$(4.34)$$

In previous equations, partial derivatives of cornering forces with respect to state variables appear. Considering that cornering forces depend only on sideslip angle, vertical load and friction, the partial derivatives can be computed as

$$\frac{\partial F_{y,j}}{\partial v_y} = \frac{\partial F_{y,j}}{\partial \alpha_j} \frac{\partial \alpha_j}{\partial v_y} \quad (4.35)$$

$$\begin{aligned} \frac{\partial F_{y,j}}{\partial \alpha_j} &= B_j C_j D_j \frac{\cos [C_j \arctan (B_j \alpha_j)]}{1 + B_j^2 \alpha_j^2} \\ \frac{\partial F_{y,j}}{\partial \mu} &= d_j F_{z,j} \sin [C_j \arctan (B_j \alpha_j)] - \frac{\alpha B_j C_j D_j}{\mu (1 + B_j^2 \alpha_j^2)} \cos [C_j \arctan (B_j \alpha_j)] \end{aligned} \quad (4.36)$$

To assess the performance of the implemented state observer for friction coefficient estimation, the following manoeuvre has been performed.

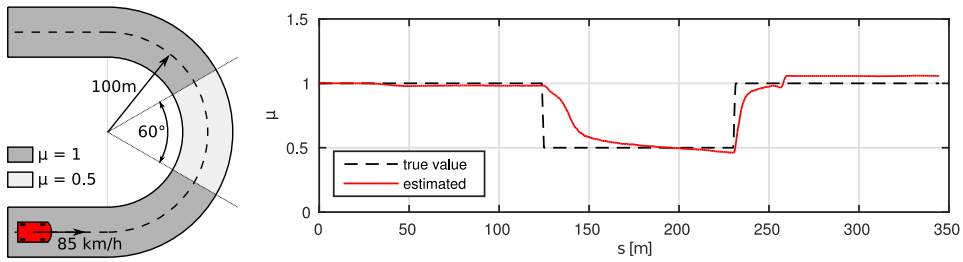


Figure 4.4: Friction estimation by EKF as function of curvilinear abscissa s for a constant radius turn with friction variation from 1 to 0.5.

It consists of 100 m radius U-turn carried out at the constant speed of 85 km/h. The U-turn is divided into 3 regions characterized by a different friction coefficient, as shown in Figure 4.4. Specifically, a circle sector having 60° amplitude and characterized by a friction coefficient of 0.5 is placed in the middle of the turn. The friction coefficient is equal to 1 elsewhere. Since the friction coefficient is varied abruptly (0.5 m), the test allows to evaluate the bandwidth of the state observer. As it can be seen in Figure 4.4, when passing from high to low friction, the friction coefficient estimation error is less than 20% after 21 m (0.9 s being speed 85 km/h) instead when passing from low to high friction the estimation error is lower than 20% after only 5 m (0.2 s).

Simulation results of another test manoeuvre is reported in Figure 4.5. It is a double lane change manoeuvre performed on low friction road ($\mu = 0.5$). Figure reports the yaw rate $\dot{\psi}$, lateral acceleration a_y , sideslip angle β and friction coefficient μ estimations compared with true values. The correct estimation of friction coefficient is achieved after less than 2 seconds from the very first steering wheel actuation. The convergence of the filter is faster in fact only when the vehicle approaches the maximum value of lateral acceleration allowed by friction coefficient. It is in fact well known that the cornering stiffness of the tyres does not depends on friction coefficient. This reflects on filter performances: friction coefficient is non observable for really low lateral acceleration when cornering stiffness is constant; only with higher values of lateral accelerations the non linearity of cornering forces allows to observe the friction coefficient and thus the filter can correctly converges to the true value. This effect is of minor importance for the designed steady-state controller whose target is to improve vehicle cornering performances for high lateral accelerations. Also vehicle dynamics

4.2. SIDESLIP ANGLE AND FRICTION COEFFICIENT

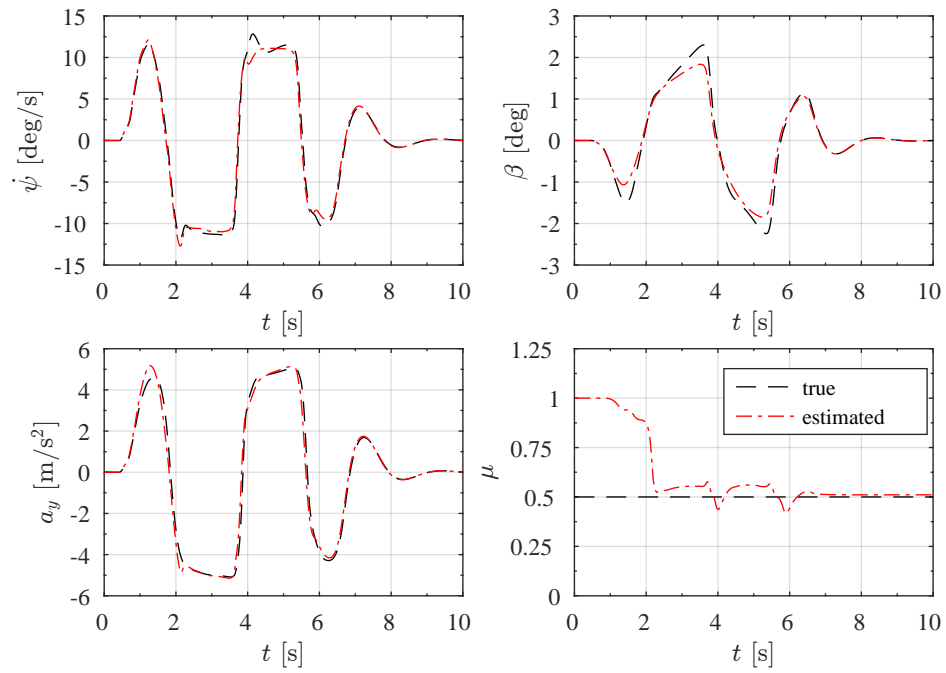


Figure 4.5: Friction estimation by EKF for a double lane change manoeuvre on low friction road $\mu = 0.5$.

for low lateral accelerations is more stable than for high accelerations, this means that a wrong estimation of friction coefficient is not so important in these cases.

CHAPTER 5

Simulation results

SIMULATIONS have been performed in order to evaluate controller performances. In this chapter results from simulations are shown. The simulated manoeuvres are reported in table 5.1, the aim is to test controller performances both in transient and in steady-state conditions and with and without coupling with driver (open and close loop manoeuvres). For some manoeuvres also the effect of friction coefficient variation is analysed.

In particular simulations results of the following manoeuvres are reported:

- steady-state manoeuvres, in which the steady-state full active vehicle is compared to passive vehicle:
 - steering pad constant radius: close loop manoeuvre, steer is actuated by the driver model previously presented;
 - steering pad constant speed: open loop manoeuvre, vehicle speed is increased by cruise controller.
- transient manoeuvres, in which the active vehicle is compared to both to passive vehicle and vehicle equipped only with DSC controller:

Table 5.1: *Simulated manoeuvres*

Manoeuvre	type	steer input	friction	standard
Steering Pad Const. Radius	steady-state	close-loop	high and low	ISO 4138
Steering Pad Const. Speed	steady-state	open-loop	high	ISO 4138
Step steer	transient	open-loop	high and low	ISO 7401
Braking in a turn	transient	open-loop	high and low	ISO 7975
Power on in a turn	transient	close-loop	high	
Double lane change	transient	close-loop	high and low	ISO 3888

- step-steer manoeuvre: open loop in which speed is maintained by cruise controller;
- braking in a turn: open loop where braking force are required by the driver;
- power-on manoeuvre: close loop with a reference trajectory;
- double lane change: close loop with a reference trajectory.

5.1 Steady-state circular driving behaviour

Steady-state performances of the controller have been tested according to standard ISO 4138 [19]. Steering pad constant radius and steering pad constant speed manoeuvres have been simulated comparing the passive and the active vehicle.

5.1.1 Steering pad constant radius

Steering pad constant radius manoeuvre is a close loop manoeuvre in which, as suggested by standard ISO 4138 [19], the test vehicle is driven at several speeds over a circular path of known radius. The standard radius of the path shall be 100 m, but larger and smaller radii may be used, with 40 m as the recommended lower value and 30 m as the minimum.

The directional-control response characteristics are determined from data obtained while driving the vehicle at successively higher speeds on the constant-radius path. This procedure can be conducted in a relatively small area. During the test, the vehicle remains on a circle with a continuous slow speed increase, during which data are taken.

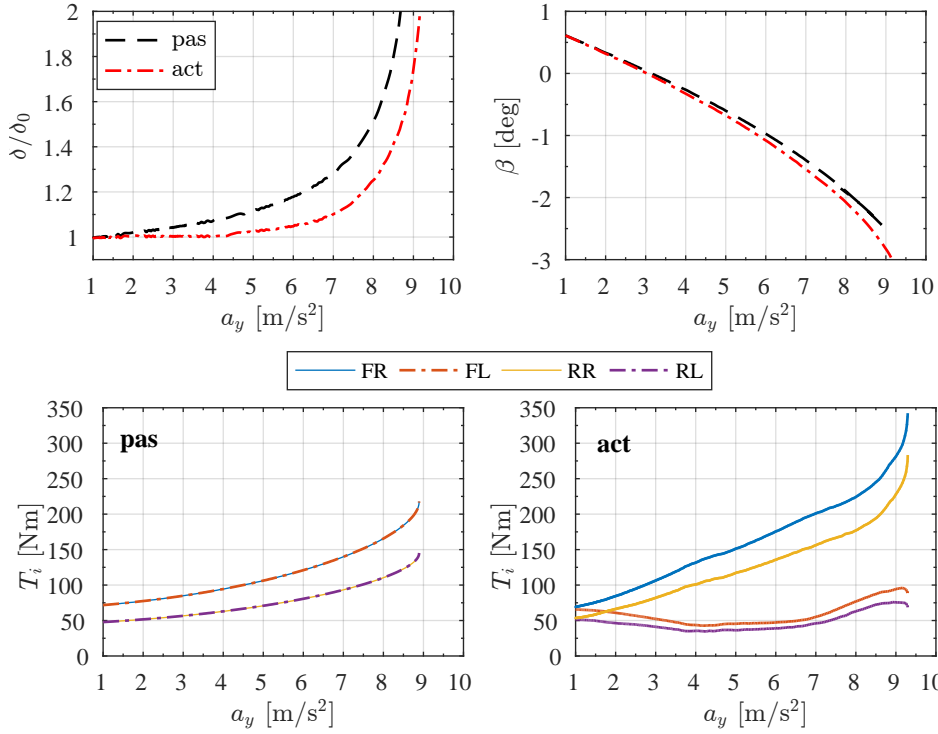


Figure 5.1: Steering pad constant radius (100 m) manoeuvre on low friction road $\mu = 1$. Comparison between active and passive vehicles.

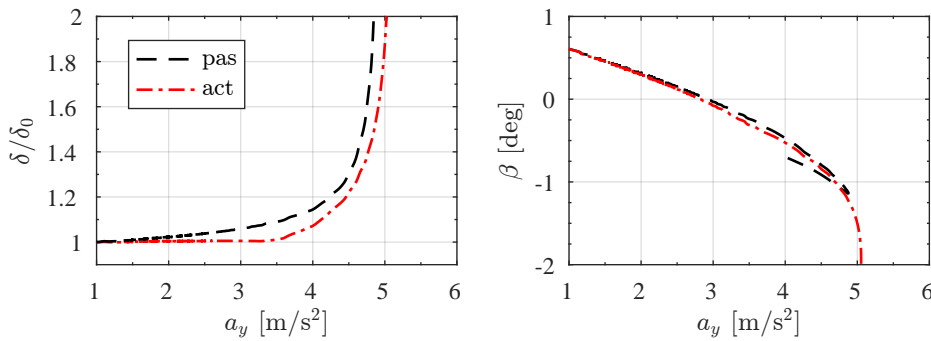


Figure 5.2: Steering pad constant radius (100 m) manoeuvre on low friction road $\mu = 0.5$. Comparison between active and passive vehicles.

5.1. STEADY-STATE CIRCULAR DRIVING BEHAVIOUR

Table 5.2: *Steering pad constant radius on high friction. Steering wheel angle as function of lateral acceleration.*

a_y [m/s ²]	1	2	3	4	5	6	7	8	9
δ_{SW} pas [deg]	26.8	27.3	28.1	28.9	30.0	31.7	34.6	40.6	-
δ_{SW} act [deg]	26.8	27.0	27.0	27.0	27.5	28.1	29.6	33.7	46.9

Results of the manoeuvre on high friction road are shown in Figure 5.1 and in Table 5.2 where steering angle ratio δ/δ_0 ¹ and sideslip angle β are reported as function of lateral acceleration a_y . It can be noticed that, with respect to passive, the active vehicle presents an extended range where the steer response is linear (up to 5 m/s² as imposed by the reference yaw rate of SSC controller. From 5 to 8 m/s² active vehicle slowly increases the steer gradient in order to let the driver understand that the vehicle is approaching the maximum lateral acceleration allowed by friction limit. Above 9 m/s² the active vehicle presents an higher maximum lateral acceleration with respect to passive vehicle: the increase is about 5.7% (passive 8.88 m/s² versus active 9.39 m/s²). No significant differences can be noticed in sideslip behaviour as function of lateral acceleration.

In Figure 5.1 also torques on wheels are reported. It can be noticed that the controller applies a yaw moment that helps the vehicle to turn. Right wheels torques are higher than left wheels. The resulting yaw moment reduces understeering behaviour of the vehicle helping the driver to remain on the reference circular path with smaller corrections on the steering wheel when lateral acceleration is smaller than 5 m/s², while, when it increases, the yaw moment reduces in order to alert the driver that the vehicle is reaching the maximum lateral acceleration. A considerable amount of yaw moment is still necessary for really high lateral acceleration in order to increase the maximum achievable value of a_y .

Even on low friction road, see Figure 5.2, the active vehicle presents the same improvements. The steering wheel angle has a linear behaviour up to 3.5 m/s² than is increases slowly up to the maximum lateral acceleration

¹ δ_0 is the Ackermann kinematic steering angle defined as

$$\delta_0 = \arctan\left(\frac{l}{\rho}\right) \quad (5.1)$$

where l is vehicle wheelbase and ρ is the curvature radius of the trajectory which, in this case, is constant and equal to 100 m.

which, compared to the one of passive vehicle, is increased up to 5.05 m/s^2 (3.5% higher than passive vehicle). Looking at sideslip angle it can be noticed that while passive vehicle presents a sudden change when the vehicle reaches the maximum lateral acceleration, the active vehicle has instead a smoother behaviour and a smaller gradient $\partial\beta/\partial a_y$. This is an advantage for the driver that can better perceive the maximum limit of the vehicle.

5.1.2 Steering pad constant speed

Steering pad constant speed is the dual manoeuvre of steering pad constant radius. It is an open loop manoeuvre which requires driving the test vehicle at one speed on circular paths of different radii, utilizing a range of steering-wheel angles. The directional-control response characteristics are determined from data plotted against lateral acceleration.

This test method could require large test areas, depending on the combination of speed and lateral acceleration. The discrete turn radii method requires a number of marked circles or circular segments with different radii, sufficient in number to provide 0.5 m/s^2 lateral acceleration increments at the selected speed. An adjustable steering stop should be used, for maintaining constant steering-wheel angles when using the discrete steering-wheel angle method.

The standard test speed is 100 km/h. If higher or lower speeds are selected, they shall be in 20 km/h increments.

Simulation results on high friction road are reported in Figure 5.3. Similarly to steering pad constant radius manoeuvre, the active vehicle, with respect to passive, presents an increased range in which the steer gradient is constant, up to 5 m/s^2 . Above this value of lateral acceleration, the steer gradient grows slowly up to the maximum value of lateral acceleration which is increased with respect to passive vehicle of about 4%. The increase of lateral acceleration with steering-wheel angle is thus more gradual, the vehicle results more straightforward for the driver. Looking at sideslip angle it can be noticed that the active vehicle slightly increases it but the maximum value does not exceed 3.5 degrees, this means that the vehicle is stable and controllable by the driver.

5.1. STEADY-STATE CIRCULAR DRIVING BEHAVIOUR

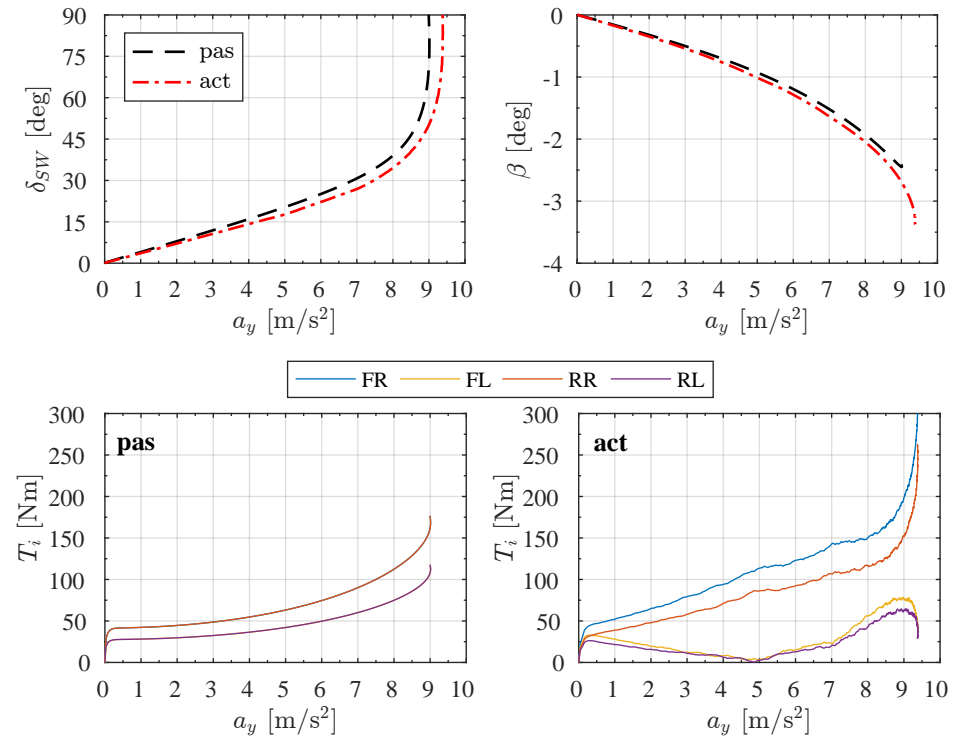


Figure 5.3: Steering pad constant speed manoeuvre. Comparison of active and passive vehicle. Manoeuvre is performed at 100 km/h

5.2 Lateral transient response

In order to assess controller performance in transient conditions, several transient manoeuvres have been simulated comparing passive vehicle (pas in legends) with full active vehicle (act in legends) and with vehicle equipped only with transient controller (dsc in legends). Both open and close loop manoeuvres have been simulated in order to evaluate the driver-vehicle interaction.

5.2.1 Steer step

Step steer manoeuvre is an open loop transient manoeuvre simulated according to ISO 7401 [21].

The vehicle is driven at constant speed in a straight line. A steering input is applied as rapidly as possible to a preselected value and maintained at that value for several seconds after the measured vehicle motion variables have reached a steady state. In order to keep the steering input short relative to the vehicle response time, the time between 10% and 90% of the steering input should not be greater than 0.15 s. No change in throttle position shall be made, although speed may decrease. The selected steer value is on purpose chosen so that the vehicle reaches the maximum lateral acceleration and the maximum yaw rate allowed by friction limit in order to better evaluate controller performance in limit manoeuvre.

Simulation results of a step-steer manoeuvre on high and low friction road are shown respectively in Figure 5.4 and 5.6. Table 5.3 instead reports the simulation results as suggested by standard ISO7401, i.e. lateral acceleration, yaw rate and sideslip angle. The meaning of the reported quantities is here explained²:

- \diamond_{ss} represents the steady-state value of \diamond quantity;
- $90\% \diamond_{ss}$ represents the 90% of the steady-state value of \diamond quantity;
- \diamond_{max} represents the maximum value of \diamond quantity;
- t_{\diamond} represents the time at which the \diamond quantity reaches the 90% of its steady-state value;

²diamond marker \diamond is used to indicate a general quantity since the explanation reported in section refers to subscripts which are applied to different variables (steering angle, yaw rate, lateral acceleration, etc..) with the same meaning.

5.2. LATERAL TRANSIENT RESPONSE

Table 5.3: Step-steer manoeuvre on high and low friction road surface.

		$\mu = 1$			$\mu = 0.5$		
		pas	act	dsc	pas	act	dsc
δ_{ss}	[deg]		50			30	
50% δ_{ss}	[deg]		25			15	
t_0	[s]			0.55			
$a_{y,ss}$	[m/s ²]	8.63	8.87	8.67	4.82	5.06	4.82
90% $a_{y,ss}$	[m/s ²]	7.77	7.99	7.80	4.34	4.56	4.33
$a_{y,max}$	[m/s ²]	9.15	8.90	8.95	5.03	5.06	4.85
t_{a_y}	[s]	0.92	1.025	0.96	0.91	0.86	0.96
$t_{a_y,max}$	[s]	1.22	1.19	1.18	1.46	1.09	1.61
$\dot{\psi}_{ss}$	[deg/s]	17.95	18.46	18.04	9.99	10.50	9.97
90% $\dot{\psi}_{ss}$	[deg/s]	16.15	16.62	16.23	8.99	9.45	8.98
$\dot{\psi}_{max}$	[deg/s]	23.55	19.39	21.48	13.51	14.07	11.79
$t_{\dot{\psi}}$	[s]	0.73	0.75	0.74	0.74	0.64	0.74
$t_{\dot{\psi},max}$	[s]	0.98	1.15	0.98	0.36	0.385	0.36
β_{ss}	[deg]	-1.48	-1.83	-1.47	-1.45	-2.17	-1.43
90% β_{ss}	[deg]	-1.34	-1.64	-1.32	-1.30	-1.95	-1.29
β_{max}	[deg]	1.58	1.84	1.48	2.16	2.17	1.52
t_{β}	[s]	1.02	1.25	1.20	1.01	1.16	1.16
$t_{\beta,max}$	[s]	1.21	1.19	1.18	1.36	1.41	1.36

- $t_{\diamond,max}$ represents the time at which the \diamond quantity reaches its maximum value;

Simulation on high friction (Figure 5.4) shows that the DSC vehicle presents lower oscillation and lower peak values of yaw rate, sideslip angle and lateral acceleration: with respect to passive vehicle the peak value of yaw rate is reduce of about 7% while practically no oscillation appears in sideslip angle. Full active vehicle is as effective as DSC in damping oscillation but it presents higher values of yaw rate and sideslip angle at the end of the manoeuvre: the steady state value of yaw rate for full active vehicle is 8.5% higher of both passive and DSC vehicle. Practically same increase is obtained for steady-state lateral acceleration. This is due to the higher linear behaviour of the full active vehicle thanks to SSC controller as better shown in steady-state manoeuvres results reported in following paragraph. Full active vehicle presents also higher promptness. This can be seen look-

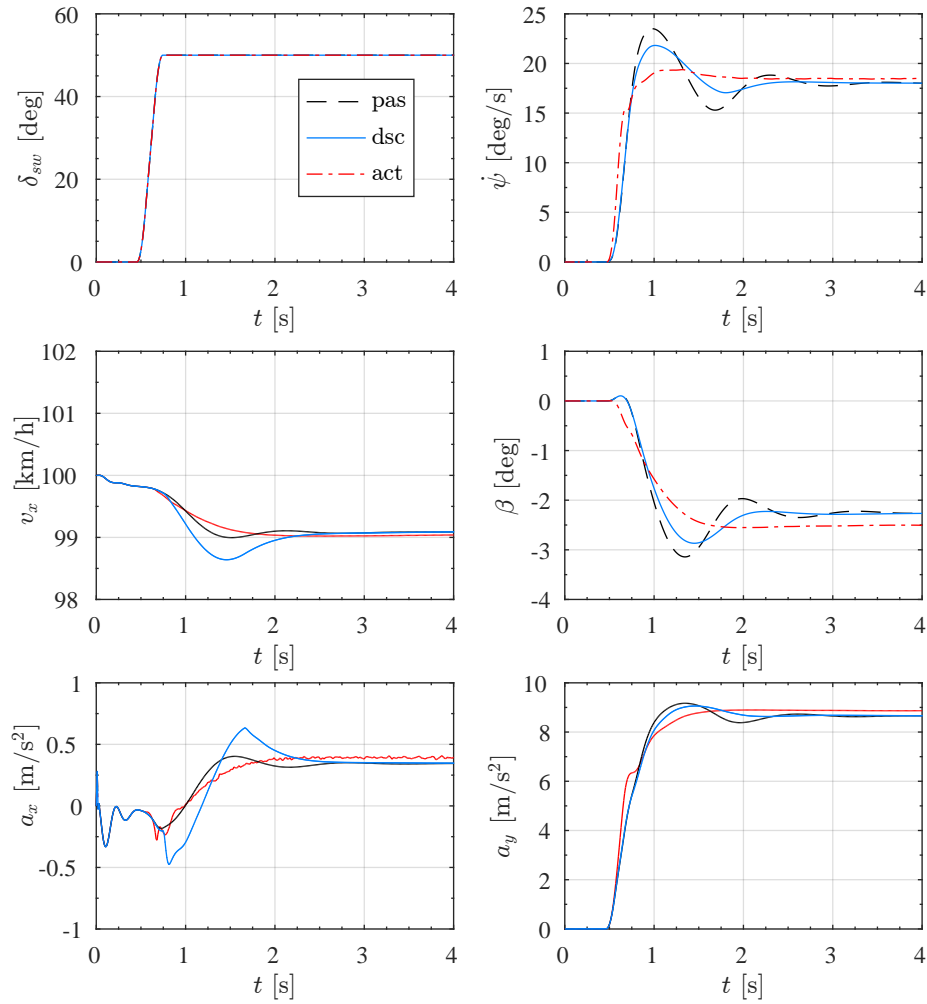


Figure 5.4: Simulation data of a steer step manoeuvre on high friction road surface ($\mu = 1$).

5.2. LATERAL TRANSIENT RESPONSE

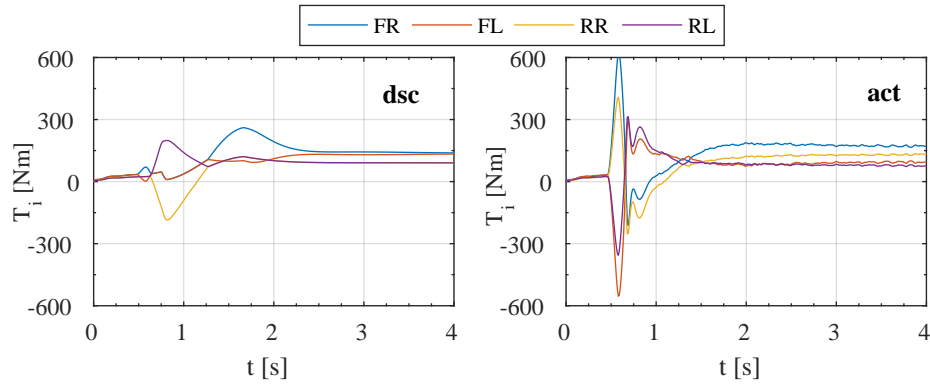


Figure 5.5: Simulation data of a steer step manoeuvre on high friction road surface ($\mu = 1$). Torque on wheels required by controller for DSC vehicle and full active vehicle.

ing at time need to reach the peak values of yaw rate which is 34% lower than both passive and DSC vehicle.

Figure 5.5 reports the wheel torques required by controllers in DSC and in full active vehicle. Significant differences can be noticed in particular in the beginning and at the end of the time history. The full active controller requires higher torques in the first part in order to make the vehicle turn faster when the steer is actuated. More in details it can be noticed that the right wheels torques (outer wheels since the turn is leftward) are higher than left wheels torques (inner wheels), this means that the controller is requiring an counterclockwise yaw moment (pushing the vehicle inside the turn) that helps the vehicle to steer. At the end of the manoeuvre, when steady-state conditions are achieved, the controller is still requiring an inward yaw moment and, in fact, the steady-state acceleration, as well as yaw rate, of full active vehicle is higher than DSC and passive vehicles. In the transient part of the manoeuvre, quite same torques are required by DSC and full active vehicle since in this part the DSC contribution is prevailing over SSC contribution. According to torques distribution strategy for DSC it can be noticed that in the first part of the steer actuation (t is about 0.5 s), the yaw moment is generated by DSC using only front wheels (the vehicle is in fact dynamically over-steering because of the time needed to the rear axle to develop a suitable cornering force) and in the same direction of the steer angle. In the second part ($0.6 < t < 0.8$ s) the vehicle is dynamically under-steering because the steer angle is increasing really fast and

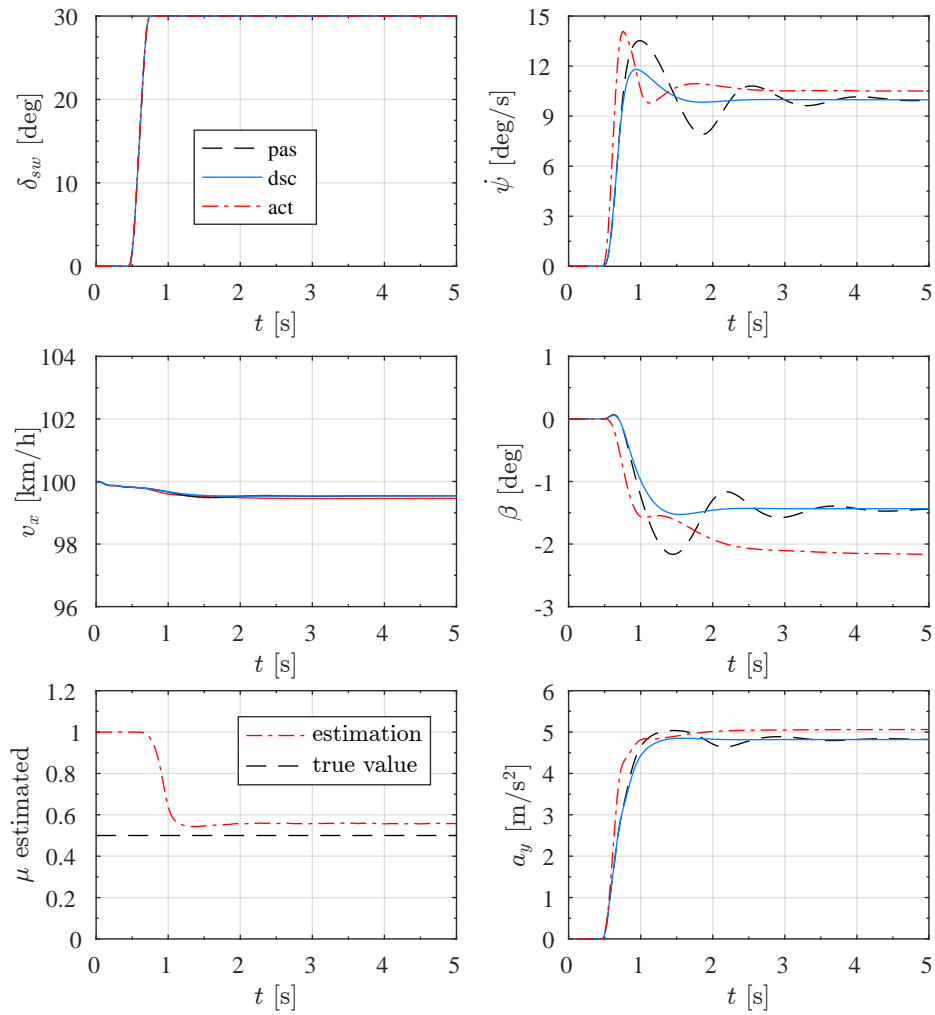


Figure 5.6: Simulation data of a steer step manoeuvre on low friction road surface ($\mu = 0.5$).

DSC generate an inward yaw moment using rear wheels. In the third part of the manoeuvre ($t > 0.9$ s) the vehicle is dynamically over-steering thus DSC generates a yaw moment outward the turn using only front wheels.

On low friction (Figure 5.6) same considerations can be done. DSC vehicle presents better performances than full active vehicle due to the time needed by SSC controller to correctly estimate the friction coefficient as it can be seen in Figure where the time history of a_x has been substituted by the friction coefficient estimated by EKF. The estimation takes about 0.35 seconds to reach the steady-state value (0.58 versus 0.5 which is the real value). In particular this can be seen in yaw rate time history where the full active vehicle presents the higher peak 4.5% higher than passive vehicle while DSC vehicle presents a decrease of about 12.7%.

5.2.2 Braking in a turn

As reported in standard ISO 7975[18], the purpose of this test is to examine the effect of braking on course holding and directional behaviour of a vehicle. Specifically, the method determines how the steady-state circular response of a vehicle is altered by braking action only when the steering wheel is maintained at the steady-state value achieved before the braking; it is an open loop manoeuvre.

The initial conditions are defined by constant longitudinal velocity and by a circle with a given radius, as specified by the constant-radius test method of ISO 4138. The steering wheel angle required for the steady-state circular run shall be constantly maintained during the entire test. During the test, the driver input and the vehicle response are measured and recorded. From the recorded signals, characteristic values are calculated.

Figure 5.7 reports results of the manoeuvre on an high friction road surface. The following quantities are considered: steering-wheel angle δ_{SW} , yaw rate $\dot{\psi}$, longitudinal vehicle speed v_x , sideslip angle β and longitudinal a_x and lateral a_y accelerations; also trajectory is reported.

The passive vehicle cannot accomplish the manoeuvre and spins; simulation has been interrupted when the vehicle sideslip angle exceeded a value of 30 degrees. DSC and full active vehicle complete the manoeuvre with similar results in terms of deceleration. The value of a_x remains constant and after 5 seconds of braking the terminal speed is 9.3 km/h for full active and 7.8 km/h for DSC vehicle.

The lateral dynamics behaviour presents instead same relevant differences. Looking at yaw rate, the peak of yaw rate for DSC is 44% higher

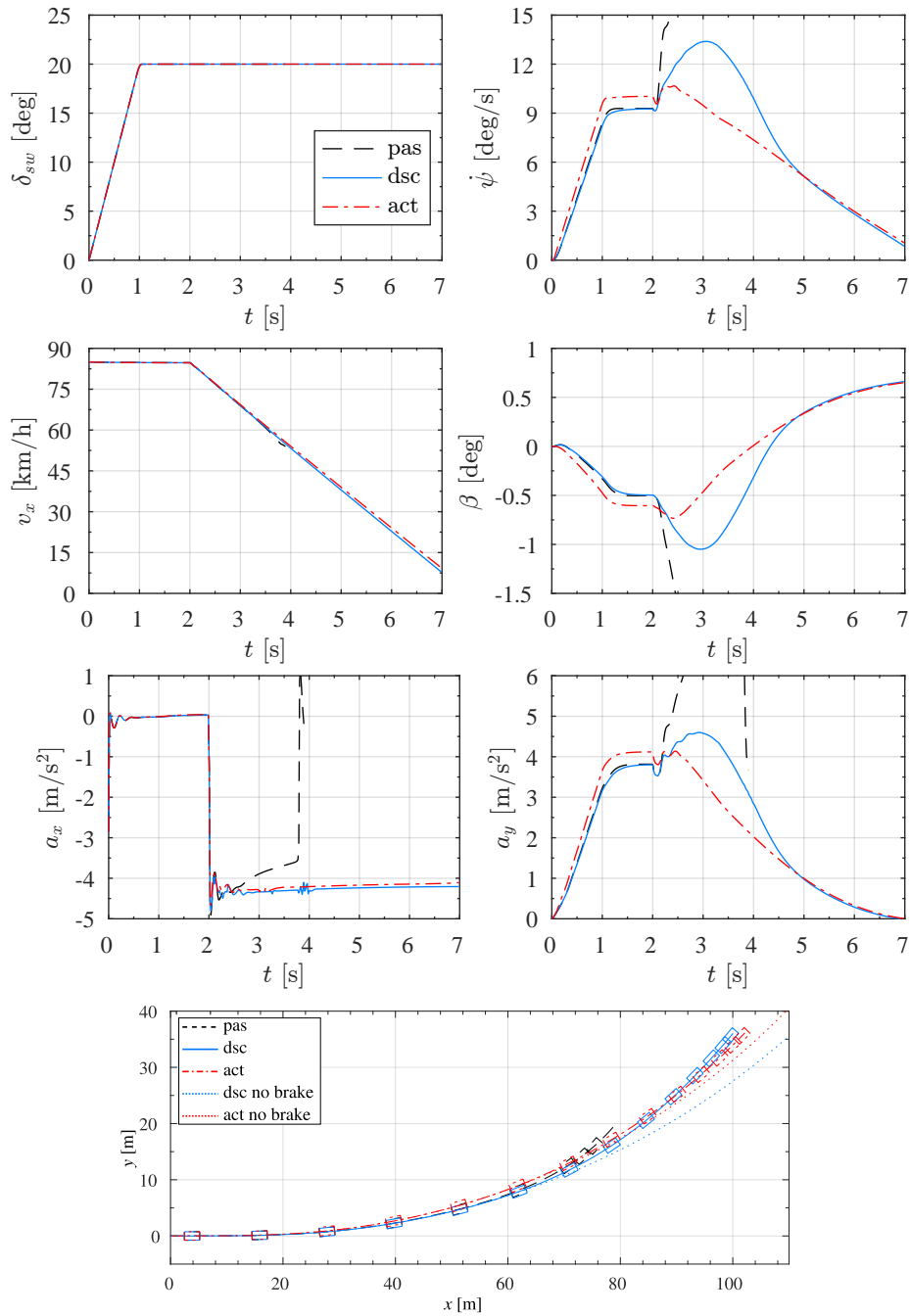


Figure 5.7: Simulation data of a braking in a turn manoeuvre on high friction road surface ($\mu = 1$).

5.2. LATERAL TRANSIENT RESPONSE

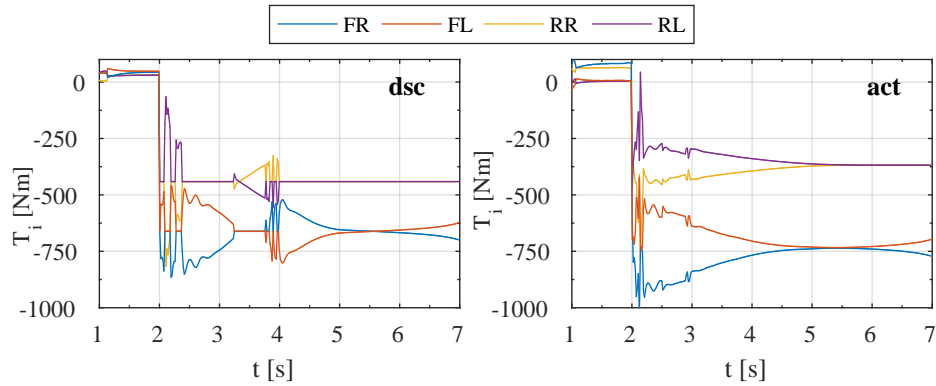


Figure 5.8: Simulation data of a braking in a turn manoeuvre on high friction road surface ($\mu = 1$). Torques on wheels.

than steady-state value before braking. For full active vehicle the increase is instead of only about 7%. Same considerations can be done for sideslip angle (DSC +110%, full active +21%) and lateral acceleration (+21% DSC, full active +0.5%). Looking at vehicle trajectory, it can be noticed that, although being the steady-state reference radius smaller for full active vehicle, the distance from the “non-braking” trajectory (dotted lines in figure) is 6.4 m for DSC and 2.2 m for full active vehicle.

In Figure 5.8 the torques applied on wheels for the described manoeuvre are reported. It can be noticed that the behaviour of the two controller is similar, both are applying a yaw moment that contrasts the oversteering behaviour of the vehicle. DSC presents lower peak values with respect to full active vehicle of maximum braking torque on the front right wheel which is the most stressed. Full active vehicle presents instead a smoother behaviour of the required torques.

It is to point out that the applied torque are within the characteristics of the considered IWM and no hydraulic brakes intervention is required.

5.2.3 Power on manoeuvre

Power on manoeuvre is a close loop manoeuvre in which the behaviour of the vehicle is analysed when a longitudinal acceleration is required by the driver while turning. It is performed on U turn reference trajectory with a constant radius of 70 m. The vehicle enters the turn at a constant speed of 60 km/h, when steady-state cornering condition are achieved, the driver

pushed the throttle pedal requiring a constant longitudinal acceleration of about 2 m/s^2 . The test is performed on an high friction road surface.

Simulation results are reported in Figure 5.9. Results are in agreement with previous simulations results. DSC vehicle presents a smoother behaviour and a more damped oscillations of yaw rate, sideslip angle and lateral acceleration with respect to passive vehicle. Full active vehicle is even more smoother and moreover it helps the driver reducing the steering wheel angle required to follow the reference trajectory. The steering wheel angle is in fact smaller during the all of the turn, in particular low steer increase is need at the beginning of the power on (from second 8 to second 10 of the simulation) an the peak value at the exit of the turn is reduced of about 40% (active is 68 degrees versus 113 degrees of passive). This behaviour is confirmed by torques on wheels time history in which it can be noticed that the full active vehicle presents really high different torques between outer (right) and inner (left) wheels. Outer wheels torques are in fact higher than inner wheels torques, the resulting yaw moment thus increases vehicle yaw rate and lateral acceleration.

5.2.4 Double lane change

The severe double lane-change manoeuvre is a close loop manoeuvre in which the driver task is to follow a reference trajectory. This manoeuvre is a dynamic process consisting of rapidly driving a vehicle from its initial lane to another lane parallel to the initial lane, and returning to the initial lane, without exceeding lane boundaries. The test is performed according to ISO 3888-1 [20]. The speed of entry into section 1 shall be the maximum possible speed to complete the test course while any throttle position can be used during the test.

Results of the simulation are reported in Figure 5.10 and 5.11 where the test have been performed at 100 km/h on high and low friction road ($\mu = 1$ and $\mu = 0.5$) while the accelerator pedal is not actuated during the manoeuvre.

As suggested by standard, the following quantities are considered: steering-wheel angle δ_{SW} , yaw rate $\dot{\psi}$, longitudinal vehicle speed v_x , sideslip angle β and longitudinal a_x and lateral a_y accelerations; for low friction the graph of a_x is substituted with the time history of friction coefficient estimated by EKF.

Results of a double lane change on high friction road ($\mu = 1$) are reported in Figure 5.10. Looking at steering wheel angle it can be noticed that

5.2. LATERAL TRANSIENT RESPONSE

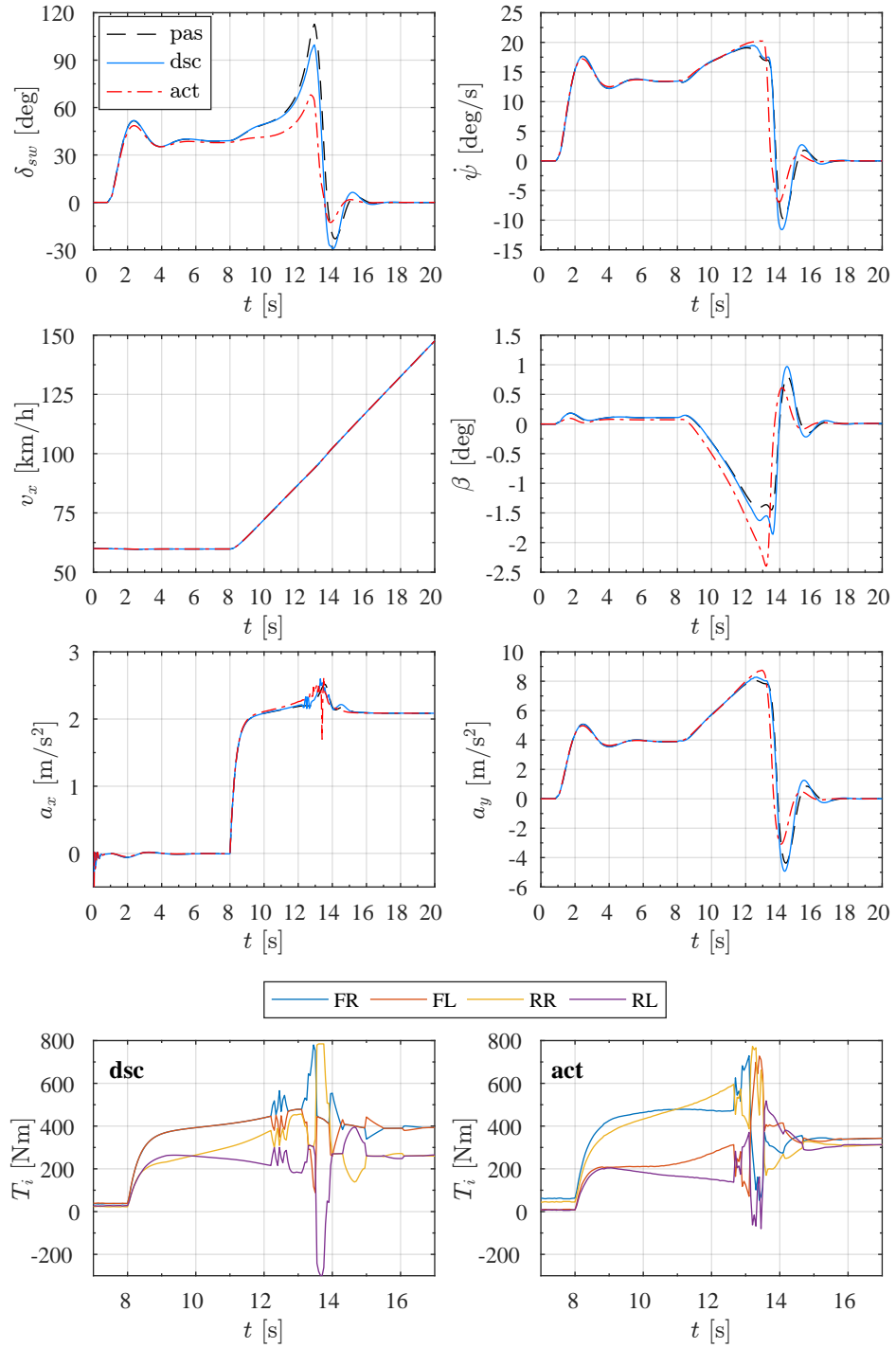


Figure 5.9: Power on manoeuvre, high friction.

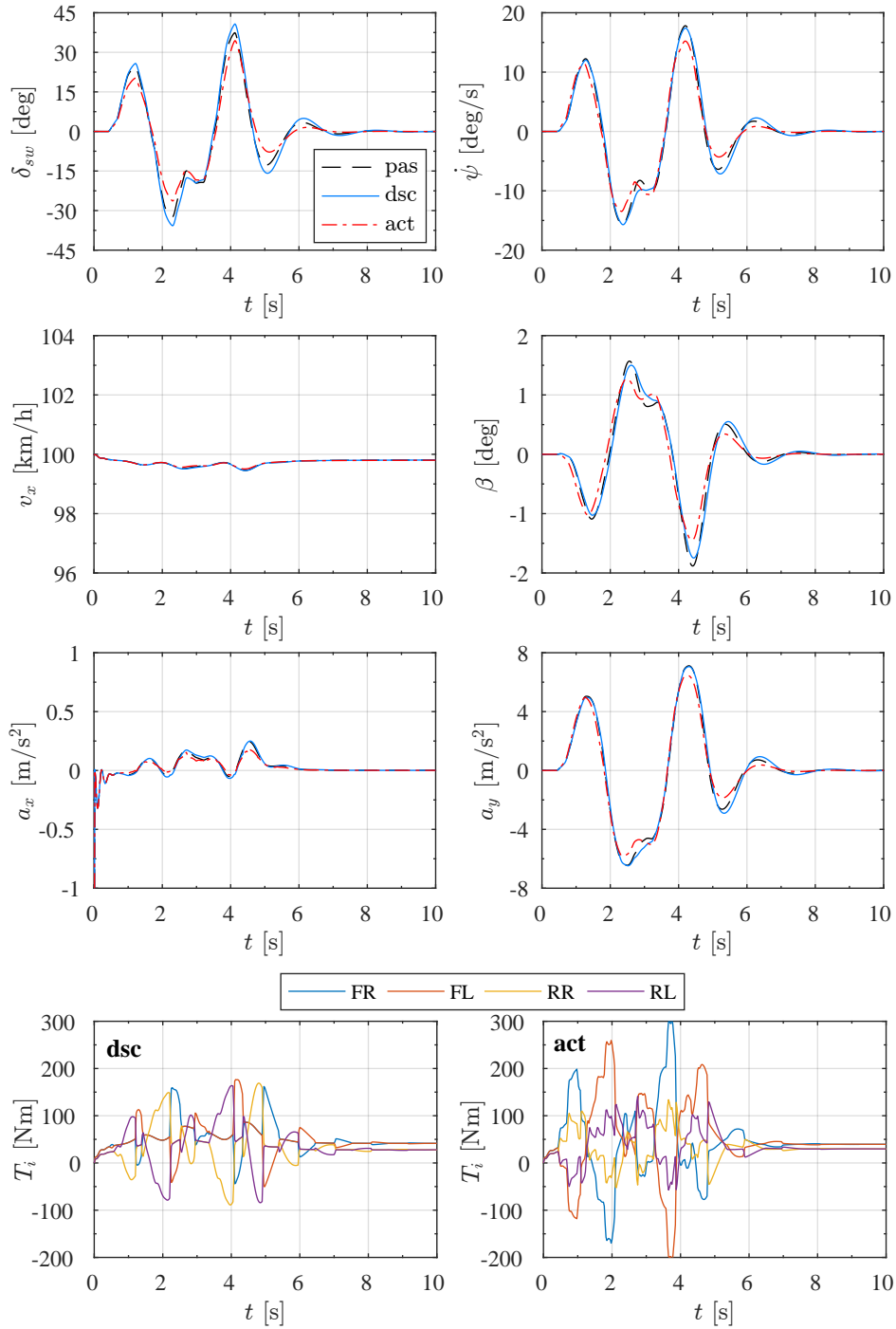


Figure 5.10: Simulation data of a double lane change manoeuvre on high friction road surface ($\mu = 1$).

5.2. LATERAL TRANSIENT RESPONSE

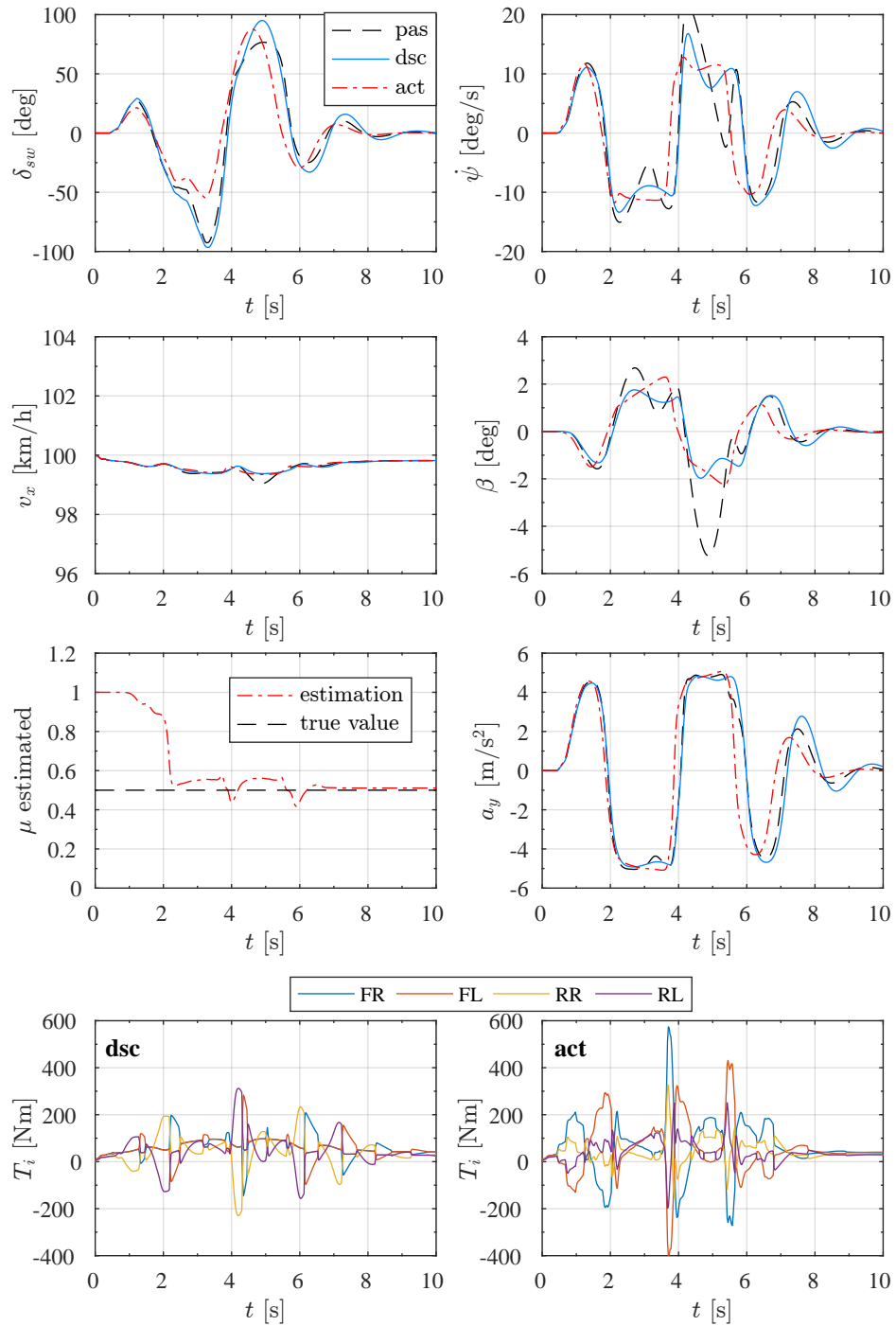


Figure 5.11: Simulation data of a double lane change manoeuvre on low friction road surface ($\mu = 0.5$).

the full active vehicle can considerably help the driver reducing the steering wheel actuation while pure DSC vehicle gives opposite result. In particular, using the passive vehicle as a comparison, the first δ_{SW} peak at about 1 s is reduced of about 20% by full active vehicle while it is increased of about 5% by DSC vehicle. Practically same amount can be obtained for the second (at $t = 2.3$ s), third (at $t = 4.1$ s) and fourth (at $t = 5$ s) peak of steering wheel angle. Looking at yaw rate, sideslip angle and lateral acceleration DSC vehicle presents the smoother behaviour, in fact it is the most effective in damping oscillation of the considered variables; in particular this can be seen from second 2 to second 4 of the time history. On the other hand the exit of the double lane change (at $5 \text{ s} \leq t \leq 6 \text{ s}$) is smoother for full active vehicle where oscillation amplitudes are significantly reduced: yaw rate is 30% lower, sideslip angle is 35% lower and lateral acceleration is 29% lower than passive vehicle.

Figure 5.11 reports instead the results of a double lane change on low friction road ($\mu = 0.5$). Practically same considerations can be done. The full active vehicle reduces considerably the steering wheel angle necessary to accomplish the manoeuvre. After 1.8 seconds from the very first steer actuation has correctly estimated the friction coefficient. The passive vehicle presents the worst behaviour, in particular this can be seen from yaw rate history which appears the most oscillating and moreover in sideslip angle that reaches a peak value of 5.2 degrees while both DSC and full active vehicles do not exceed 2.3 degrees.

5.2. LATERAL TRANSIENT RESPONSE

CHAPTER 6

TV for different powertrain layouts

IN previous chapters a control strategy applied to four independent wheel drive vehicle was presented. Although several powertrain layouts are available for HEV.

When modifying a common ICE vehicle, the most direct solution for converting it into a vehicle with an electric powertrain is to substitute the engine with one electric motor (EM). EMs however give an higher degree of freedom in designing vehicle overall layout. ICE has to be directly plug to gearbox in order to save room, also differential has been incorporated in gearbox for front wheel drive vehicles. With more than one EM, the motors can be housed onboard or directly inside the wheel (IWM), no motor reducer are need and electric motor drive can be placed in the most suitable place. Several layout can thus be imagined and actually have been developed by carmakers.

Figure 6.1 reports some possible powertrain layouts for HEV; they can be summarised as follow:

layout A consists of four independent EM, one per each wheel. This solution has been studied by many authors since it seems the one that

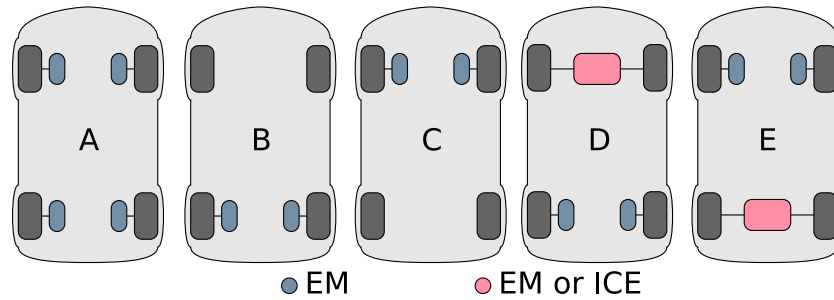


Figure 6.1: Powertrain layouts: A) 4 independent motors; B) 1 motor front 2 motors rear; C) 2 motors front 1 motor rear; D) 2 motors rear; E) 2 motors front.

better allows to exploit all EM capabilities;

layout B consists of two independent EM on the rear axle;

layout C consists of two independent EM on the front axle;

layout D consists of one motor in the front axle, which can either be a conventional ICE or an EM, and two independent EM on the rear axle;

layout E is similar to layout B but the reversed. Two independent EM on front axle and one EM or ICE on rear axle;

Aim of the present chapter is to evaluate performance of the proposed control strategy for layouts different from A, which was considered so far. Specifically, all the layouts shown in Figure 6.1 will be analysed and compared. On purpose, the previously described control strategy was adapted to each power layout, especially for what concerns torque distribution. It is to point out that the analysis is carried out considering the same weight for all layouts to evaluate the different behaviour/performance of the control strategy in the different cases. Note that this analysis may also be useful for evaluating effectiveness of the controller in downgraded conditions (failure of motors, etc.).

6.1 Steady-state torque distribution strategy for different layouts

As already mentioned, the controlled must be adapted to the different powertrain layouts. In particular, torque distribution must be modified, while it is possible to assume that calculation of torque demand remains the same independently on selected powertrain layout. Once the Optimal Controller has generated a desired yaw moment M_z , torques have to be applied on wheels in order to generate this yaw moment. It has also to be considered that also the total driving/braking force required by the driver has to be satisfied:

$$F_{xFR} + F_{xFL} + F_{xRR} + F_{xRL} = F_x \quad (6.1)$$

$$(F_{xFR} - F_{xFL})c_f + (F_{xRR} - F_{xRL})c_r = M_z \quad (6.2)$$

also vertical load distribution among front and rear axle is considered

$$\frac{|F_{xFR}| + |F_{xFL}|}{|F_{xRR}| + |F_{xRL}|} = \frac{l_r - \frac{a_x}{g}h_G}{l_f + \frac{a_x}{g}h_G} \quad (6.3)$$

where l_f and l_r are the distance of the vehicle cog from front and rear axle respectively, h_G is the height of vehicle cog, g is gravity and a_x is the longitudinal acceleration of the vehicle.

When applying the torque distribution equation (6.1), (6.2) and (6.3) to the layouts of figure 6.1, some other constraints have to be added since not all the wheels are equipped with an EM:

Layout B $F_{xFR}, F_{xFL} \leq 0$ it means that on front axle only braking torques can be developed;

Layout C $F_{xRR}, F_{xRL} \leq 0$ it means that on rear axle only braking torques can be developed;

Layout D $F_{xFR} = F_{xFL}$ it means that on front axle driving torques are the same due to differential;

Layout E $F_{xRR} = F_{xRL}$ it means that on rear axle driving torques are the same due to differential;

If layout D and E are considered as a plug-in solution, the most simple approach is to demand the driving force F_x to the axle with one motor and

6.2. SIMULATION RESULTS

the torque vectoring yaw moment to the axle with two independent motor. If previous considerations are accounted, the steady-state torque distributor generates the following torques on wheels:

layout	F_x FR	F_x FL	F_x RR	F_x RL
B	0	0	$\frac{F_x}{2} + \frac{M_z}{2c_r}$	$\frac{F_x}{2} - \frac{M_z}{2c_r}$
C	$\frac{F_x}{2} + \frac{M_z}{2c_f}$	$\frac{F_x}{2} - \frac{M_z}{2c_f}$	0	0
D	$\frac{F_x}{2}$	$\frac{F_x}{2}$	$\frac{M_z}{2c_r}$	$-\frac{M_z}{2c_r}$
C	$\frac{M_z}{2c_f}$	$-\frac{M_z}{2c_f}$	$\frac{F_x}{2}$	$\frac{F_x}{2}$

The torques applied on wheels are then

$$T_i = F_{x,i} R_r \quad (6.4)$$

6.2 Simulation results

In order to assess the control performances associated to each powertrain layout, several standard manoeuvres for vehicle dynamics evaluation have been simulated.

In order to test controller performances also with different vehicle, two different weight distribution are considered for all the layouts. In the following, vehicle 1 is a vehicle with a front to rear weight distribution of 57/43 while vehicle 2 presents a weight distribution of 43/57.

6.2.1 Steady-state circular driving behaviour

Steady state performances are evaluated by means of steering pad constant radius manoeuvre. In figure 6.2 results of the simulation are reported. In particular for each layout the active vehicle is compared with the corresponding passive vehicle:

Passive layout A is a 4WD vehicle in which torques on right and left side are equal and the ratio between front and rear torques is constant and equal to weight F/R ratio.

Passive layout B is a RWD vehicle in which torques on right and left side are equal due to differential.

Passive layout C is a FWD vehicle in which torques on right and left side are equal due to differential.

Passive layout D is equal to passive layout C since the main interest here is to compare FWD vehicle with an active solution in which torque vectoring is applied on the plug-in rear axle with two independent EMs (layout D active).

Passive layout E is equal to passive layout B since the main interest here is to compare RWD vehicle with an active solution in which torque vectoring is applied on the plug-in front axle with two independent EMs (layout E active).

Table 6.1 reports instead the numerical values of normalized steering angle for different values of lateral acceleration for active vehicles in order to compare active layouts with each other.

In general it can be observed that the active vehicle presents higher linear behaviour and an higher value of maximum lateral acceleration is achieved.

Layout B passive is always under-steering for vehicle 1 while it is over-steering for vehicle 2 for accelerations lower than 4 m/s^2 . The active layout B for both vehicle 1 and 2 presents a linear behaviour up to 5 m/s^2 . For higher lateral acceleration the increase in steering-wheel angle grows with small gradient and for vehicle 2 the active layout presents a smaller gradient with respect to passive layout. This behaviour is preferable since the driver can better perceive that limit of the vehicle is achieved. Finally the maximum lateral acceleration of the active layout with respect to passive is 2.7% higher for vehicle 1 and 1.7% for vehicle 2.

Layout C presents the best improvement with respect to its corresponding passive vehicle. In fact linear behaviour is largely increased and the maximum lateral acceleration achieved is increased of about 4.1%.

Layout D is compared with layout C passive. This is done in order to evaluate the effect of adding an independently wheel driven rear axle to a front wheel driven vehicle (passive layout C is in fact equivalent to a FWD vehicle with one motor and a differential, longitudinal forces on the front axle are the same due to differential). Layout D active vehicle 1 presents an increase in linearity with respect to passive and active layout C and an increase in maximum lateral acceleration with respect to passive layout C of about 3.4% while the maximum lateral acceleration of layout C active is 4.1% greater than passive layout C. For vehicle 2 (F/R weight distribution 43/57) results are comparable but layout D has better performances than layout C active in terms of maximum lateral acceleration. In particular the

6.2. SIMULATION RESULTS

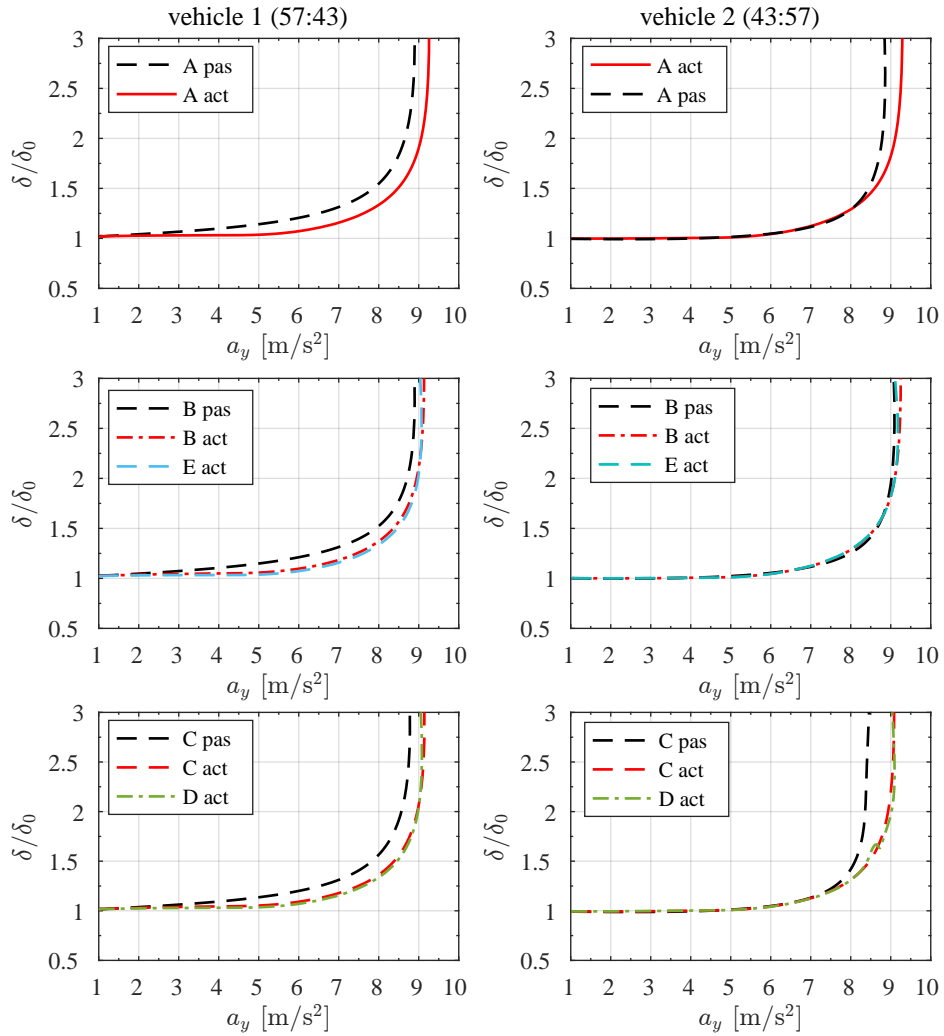


Figure 6.2: *Steering Pad Constant Radius manoeuvre. Comparison of different layout with corresponding passive vehicle. Graphs in the left column refers to vehicle 1 with a front/rear weight distribution of 57/43; graphs in the right column refers to vehicle 2 with a F/R weight distribution of 43/57.*

maximum lateral acceleration is increased of about 7.4% with respect to C passive and 0.2% with respect to C active.

Layout E is compared, as done for layout D, with passive and active layout B. Like layout D, active layout E presents an higher linearity for $a_y < 5 \text{ m/s}^2$ of both passive and active layout B. The maximum lateral acceleration is increased of about 2% for vehicle 1 and 1% for vehicle 2 with respect to corresponding passive layout B.

Comparing the active layouts, the one which presents better performances in terms of linearity is layout B but it presents the worse value of maximum lateral acceleration and the abrupt intervention of transient controller is not so indicated for commercial vehicles. The layout which instead presents the higher value of lateral acceleration is layout A. The small advantage obtained with respect to layout C makes this second layout preferable for its lower complexity. For sure layout A remains preferable when accelerating the vehicle in straightaway.

It is to point out that the passive vehicle is an understeering vehicle and the controller reference is generated in order to reduce this understeering behaviour. If the passive vehicle presents different under/oversteer behaviour the intervention of the control can change and may be tuned properly.

6.2.2 Transient cornering behaviour

Transient behaviour of the vehicle is evaluated through simulation of ATI 90-90 manoeuvre. The steer is actuated in open loop. The vehicle at the beginning of the manoeuvre has a speed of 100 km/h and no intervention is made on brakes and accelerator pedal. In this way the effect of torque vectoring only is analysed while layout B and D are exactly the same as well as layout C and E.

The passive vehicle is the same for all layouts since no torques on wheels are applied: only weight distribution is significant. Simulations have in fact been performed considering vehicle 1 and 2 like for steady-state manoeuvre. Vehicle 1 has a front to rear weight distribution of 57/43 while for vehicle 2 it is 43/57. Considering this condition layout B and D are equivalent since torque vectoring is fully exploited only by independent wheel driven axles, on other axle only braking torques are applied through hydraulic brakes; the same consideration is done for layout C and E. Thus only active layouts A, B and C are compared in simulations results.

Figure 6.3 and Figure 6.4 reports simulation results for ATI 90-90 manoeuvre for vehicle 1 and vehicle 2 respectively. The reported quantities are

6.2. SIMULATION RESULTS

Table 6.1: Steering pad constant radius. δ/δ_0 for different value of lateral acceleration and maximum lateral acceleration value. Comparison between different active and passive layouts for vehicle 1 and 2

Vehicle 1	active					passive		
	A	B	C	D	E	A	B	C
a_y [m/s ²]	δ/δ_0							
3	1.030	1.045	1.038	1.028	1.032	1.067	1.074	1.062
5	1.036	1.058	1.052	1.035	1.038	1.143	1.148	1.138
7	1.157	1.184	1.178	1.156	1.158	1.314	1.314	1.312
9	1.893	2.062	2.039	2.074	2.045	-	-	-
a_y max	9.260	9.135	9.140	9.079	9.072	8.898	8.898	8.779

Vehicle 2	active					passive		
	A	B	C	D	E	A	B	C
a_y [m/s ²]	δ/δ_0							
3	1.001	1.002	0.996	0.998	1.003	0.993	0.999	0.989
5	1.010	1.013	1.010	1.009	1.012	1.015	1.023	1.012
7	1.123	1.124	1.126	1.128	1.129	1.113	1.115	1.130
9	1.806	1.805	2.203	1.940	1.751	-	1.934	-
a_y max	9.293	9.248	9.083	9.097	9.180	8.862	9.093	8.464

the steering-wheel angle δ_{SW} , yaw rate $\dot{\psi}$, longitudinal speed v_x , sideslip angle β and longitudinal and lateral acceleration (a_x and a_y). Figure 6.5 reports the wheel torques required by controller for the three considered layouts and for the two considered vehicles. Torques required are always within the peak torque that can be developed by the considered IWM.

Passive vehicle 1 presents high oscillation of yaw rate and moreover of sideslip angle that reaches peaks of 2.5 degrees. Passive vehicle 2 cannot accomplish the manoeuvre and spins; the simulation has been interrupted when sideslip angle exceeded 30 degrees.

Layout B (same as D) is the less suitable for damping vehicle oscillations in particular when the vehicle is spinning. Controller performances degrade when the centre of gravity of the vehicle moves backward. This can be easily explained by considering the friction limit of tyre in combined slip condition. Vehicle 2 is in fact more critical than vehicle 1 and, in fact, it presents a peak value of sideslip angle of 6 degrees at the end of second step steer (about $t = 6$ s in Figure 6.4).

Layouts B is instead useful in reducing understeer and in sub-limit driving conditions as reported in steady-state simulation results ([32] reports same results). Moreover it is to point out that for this layout hydraulic brakes are still necessary to maintain vehicle stability. In case of understeering, the torque vectoring yaw moment required by torque vectoring must be applied to front wheels; if the vehicle does not have front independent motor only a brake torque can be applied to one of the front wheels. The use of hydraulic brakes results in higher decelerations, this can be seen from vehicle speed time history of both vehicle 1 and 2.

Layout C (same as E) presents comparable results with layout A which is the most performing. Both layouts reduce oscillations of yaw rate, sideslip angle and lateral acceleration, this results in an increase of vehicle damping. Also, the vehicle promptness is increased, the delay between the steer input and the vehicle response in terms of yaw rate and lateral acceleration is increased with respect to passive vehicle. At the end of the manoeuvre layout A presents the top longitudinal speed, this is due to the higher effectiveness of the controller which is capable of increasing vehicle stability without reducing longitudinal speed.

The manoeuvre consists in a first leftward step steer thus right wheel are the outer wheels and left wheels are the inner wheels. The second step steer is instead rightward, this means that right wheels are inner wheels and left wheels are outer wheels. Thus, looking at torques on wheels, see

6.2. SIMULATION RESULTS

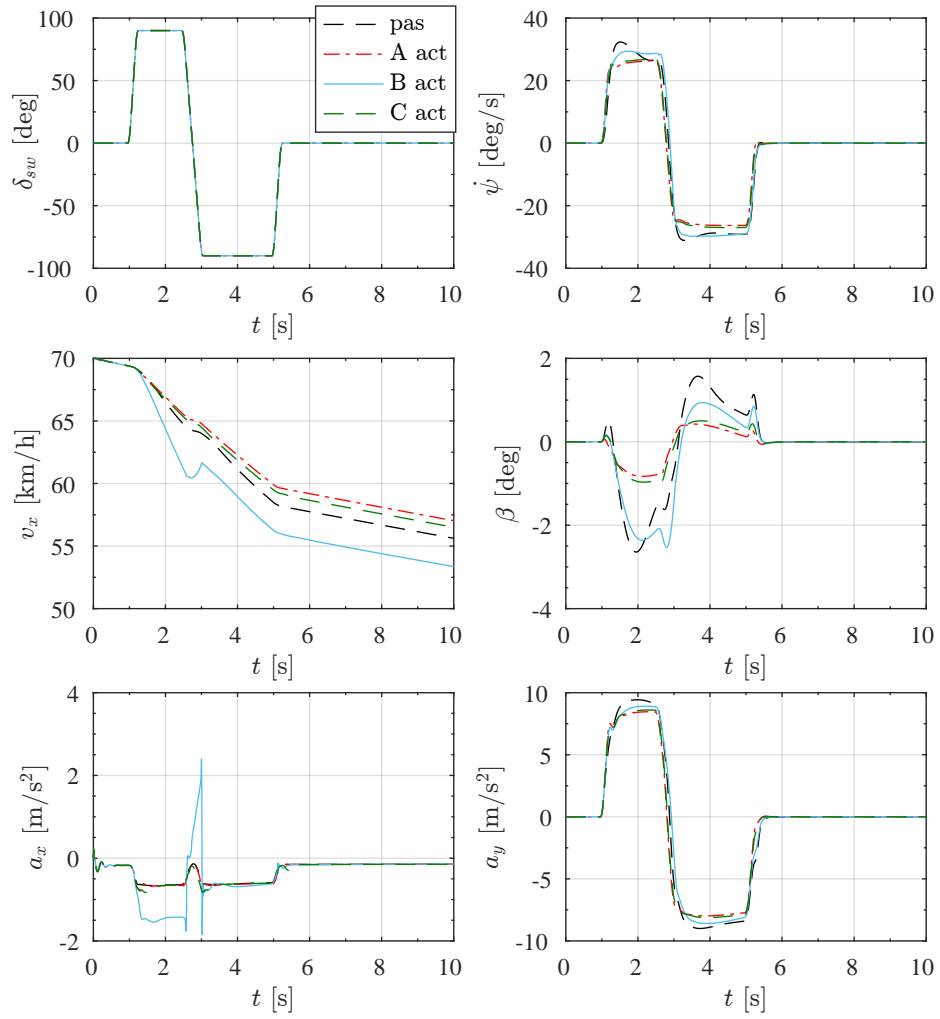


Figure 6.3: ATI 90-90 manoeuvre on high friction road surface. Vehicle 1 (F/R weight distribution 57/43). Comparison between different layouts.

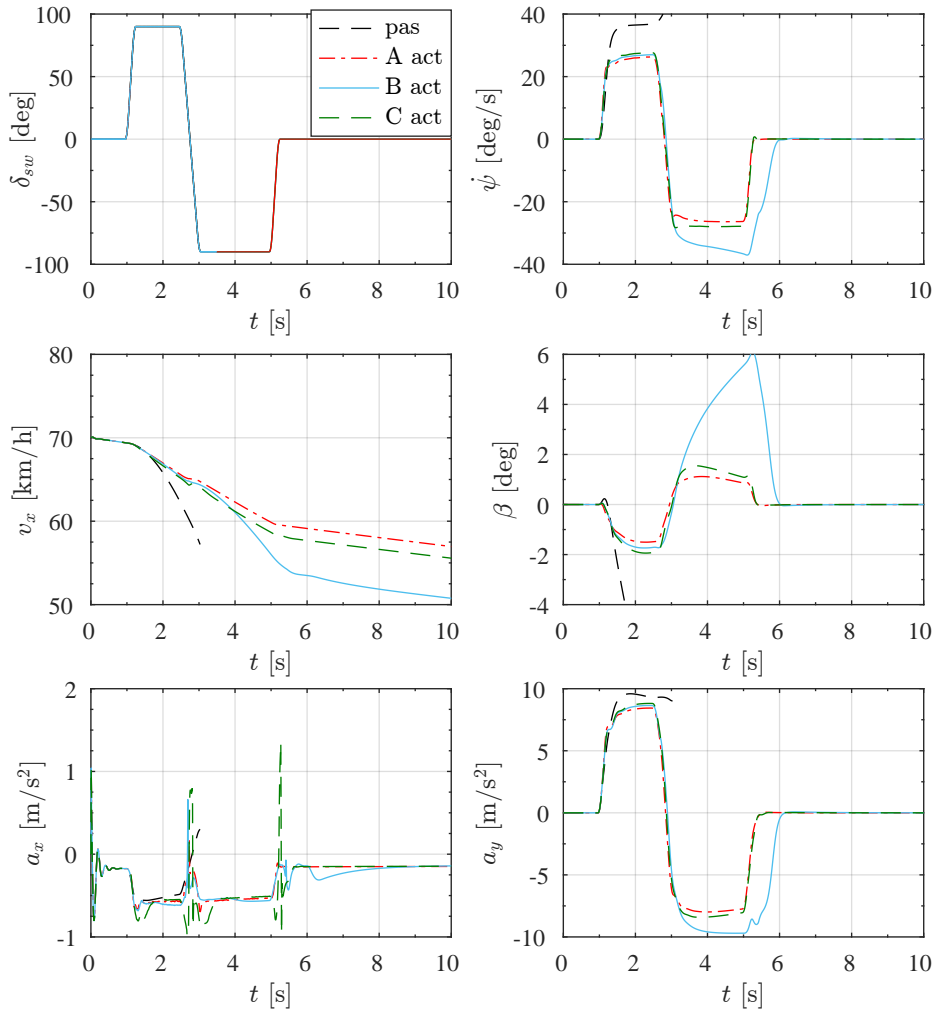


Figure 6.4: ATI 90-90 manoeuvre on high friction road surface. Vehicle 2 (F/R weight distribution 43/57). Comparison between different layouts.

6.2. SIMULATION RESULTS

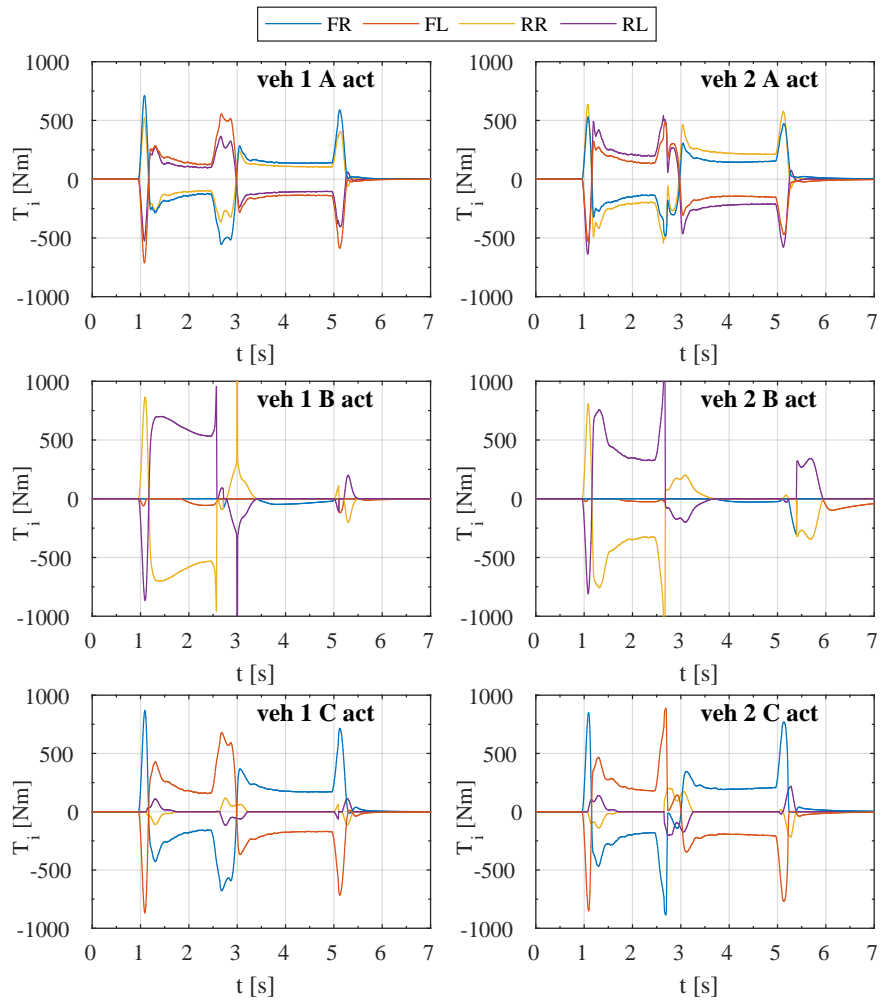


Figure 6.5: ATI 90-90 manoeuvre on high friction road surface. Vehicle 1 and 2, wheel torques.

Figure 6.5, it can be noticed that the primary target of the controller is to reduce oversteering, in fact the torques on wheels are applied mostly on the front axle and in order to generate a yaw moment opposite to yaw rate.

6.3 Considerations on different powertrain layouts

Several layouts for HEV have been compared by means of numerical simulations. Considered layouts were compared with their corresponding passive vehicle in terms of lateral dynamics behaviour in steady-state and in transient conditions. Four independent wheel driven vehicle (layout A) seems to be the most performing both in steady-state and in transient conditions. Rear independent wheel driven vehicle (layout B) presents an increase in steady-state performances with respect to passive vehicle but is not so effective in damping oscillation in transients, in fact hydraulic brakes intervention on the front axle is needed. Front independent wheel driven vehicle (layout C) is the most improving layout with respect to the corresponding passive vehicle; the only concern related to this layout is the performance comparison in pure longitudinal acceleration with respect to other layouts which was not enquired in this study. Layout D and E can be an optimal solution for expanding performances of existing vehicle with a plug-in solution on front/rear axle. In particular the plug-in solution of a front axle with independent motors allows to obtain high benefits for rear wheel drive conventional sport cars in particular cornering promptness and moreover allowing to enhance stability. It is to point out that the presented control strategy was applied to an understeering passive vehicle. Effectiveness of the controller may change if applied to a passive vehicle with difference steady-state behaviour.

6.3. CONSIDERATIONS ON DIFFERENT POWERTRAIN LAYOUTS

CHAPTER 7

Design of experimental vehicle prototype

In order to test the control strategy previously presented, a prototype of an HEV is under construction. The prototype chassis is taken from a formula SAE¹ vehicle in which the ICE has been replaced by two EMs on the rear axle.

7.1 Vehicle layout

As already mentioned, to test the developed control strategy, a formula SAE vehicle is being modified to host a pair of EMs. The vehicle is a rear wheel drive vehicle, its main dimensions and layout are reported in Figure 7.1. Since the chassis was designed for a ICE, it constraints the layout of the vehicle. The ICE has been replaced by two brushless AC motors which are positioned in the rear part of the vehicle and faced one to the other. The motors are independent and each one is connected to the corresponding wheel through a chain transmission. The motor drives are located under the

¹ The Formula SAE[®] Series competitions challenge teams of university undergraduate and graduate students to conceive, design, fabricate, develop and compete with small, formula style, vehicles.

7.1. VEHICLE LAYOUT

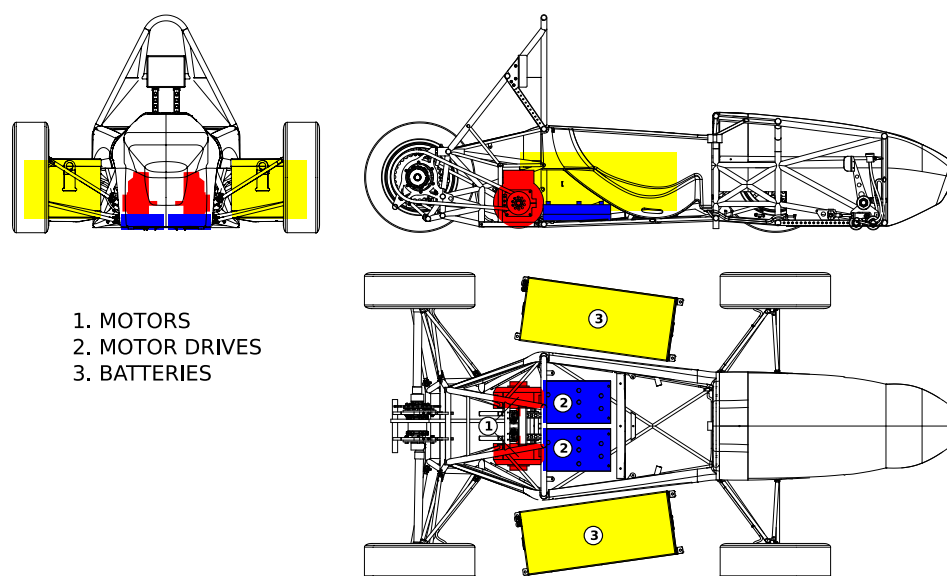


Figure 7.1: EV prototype layout. Position of motors, batteries and motor drives.

driver seat while the battery is divided in to two sub-packs placed on the sides of the vehicle. The vehicle control unit is positioned in the rear part of the vehicle just behind to the driver's head. Several sensors are used for vehicle state measurement and for driver's inputs measurements.

In the following the main information about vehicle layout, components and sensors is presented.

7.1.1 Electric motors

Electric motors are permanent magnet AC motors produced by Ashwood, model ELMO-S (see 7.3). The peak power is 15 kW while the peak torque is 70 Nm, nominal voltage is 72V and nominal peak current is 550 A. The motor torque characteristics @ 72 V and 550 A is reported in Figure 7.3 where also motor efficiency is reported.

Motors regenerative braking is used on the rear axle, of course, while on the front axle hydraulic brakes are still present and used.

7.1.2 Motor drives

Motor drives are designed and produced by DMC GmbH, the drive model is SuperSigma2. It is MOSFET based switching at 16 kHz and it allows

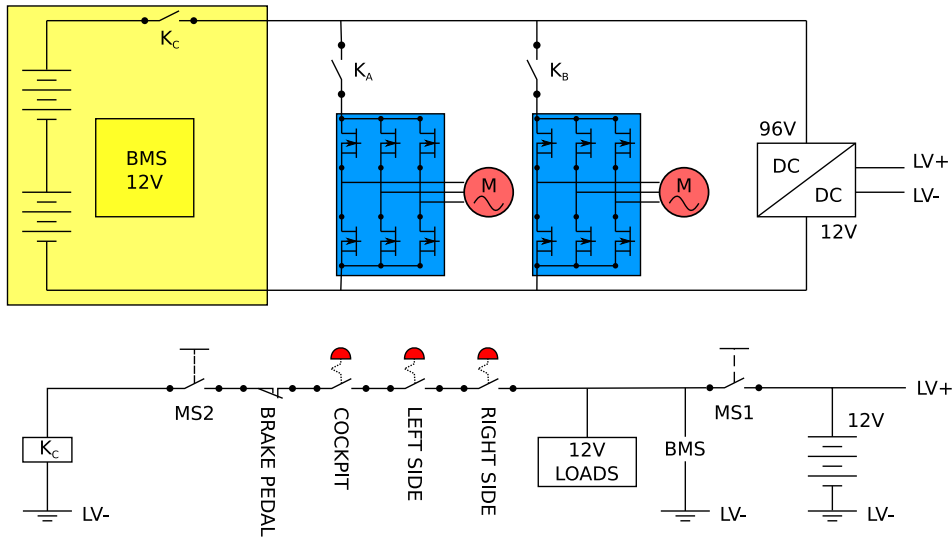


Figure 7.2: EV prototype. Electric scheme.

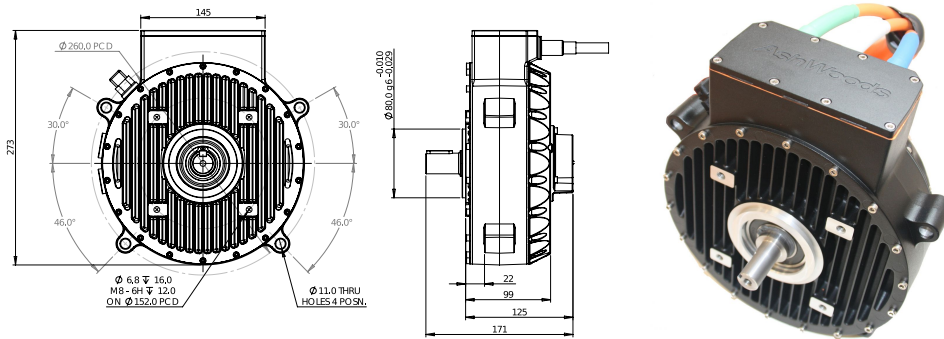


Figure 7.3: Aswood ELMO-S electric motor.

7.1. VEHICLE LAYOUT

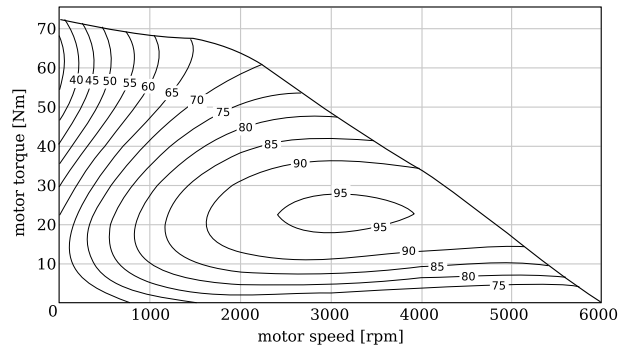


Figure 7.4: *Aswood electric motor torque as function of motor speed with efficiency map when power source is 72V.*

both torque and speed control of the motors. Torque control is used for clear reasons. Motor drives have a nominal voltage of 96V and a maximum current of 600 Arms. They communicate through CAN Open protocol with vehicle control unit from which they receive torque command.

7.1.3 Battery pack

Battery pack is produced by Kaitex SRL. It is a pack of 30 cells with a nominal total voltage of 96V and a nominal capacity of 100 Ah. The discharge ratio is 3C, it means that the peak current is 300 A. The battery pack is divided into two sub-packs with a voltage of 48V and a mass of 64 kg each which are positioned in left and right side of the vehicle respectively. In this way the weight distribution along y axis is balanced and the cog of the pack is in the middle of the vehicle. Along x axis, the cog of battery pack is in the middle of vehicle wheel base.

The battery pack is equipped with BMS and communicates through CAN Open protocol.

7.1.4 Vehicle control unit

The control unity of the vehicle is a CompactRio NI 9074 by National Instruments. Connections scheme is reported in Figure 7.5. CompactRIO platform features a range of embedded controllers with two processing targets: (1) a real-time processor for communication and signal processing and (2) a user-programmable FPGA to implement high-speed control and

DESIGN OF EXPERIMENTAL VEHICLE PROTOTYPE

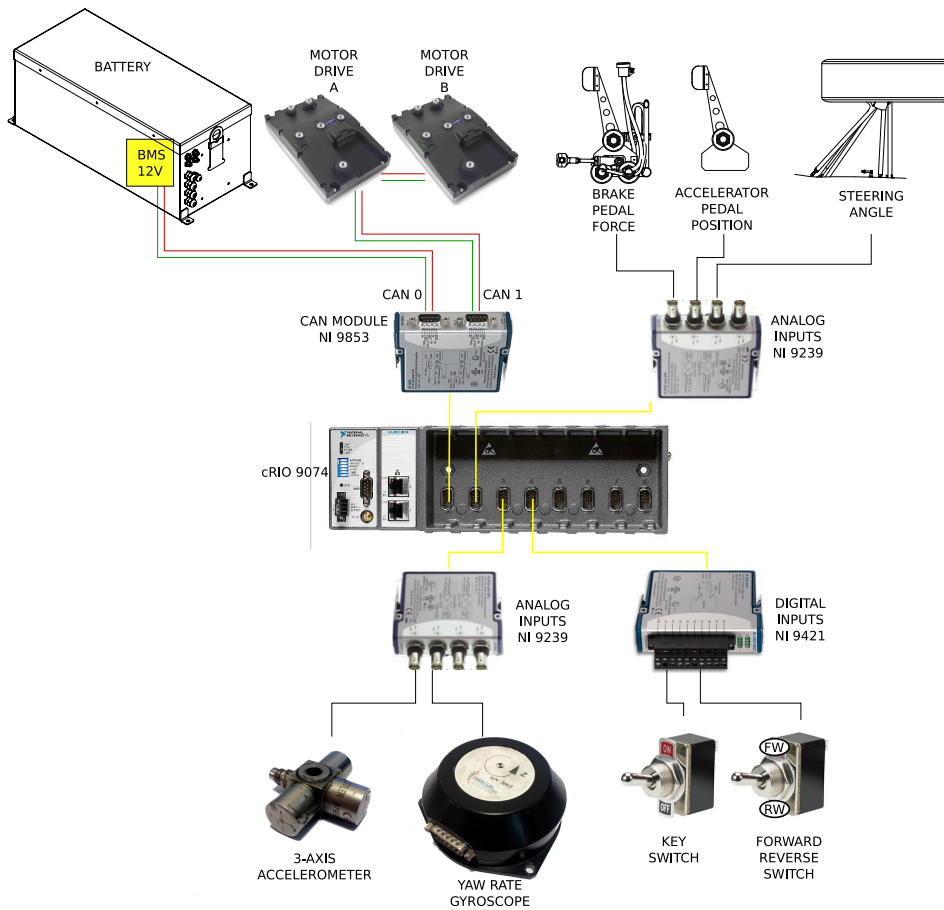


Figure 7.5: Vehicle Control Unit and scheme of collected signals.

custom timing and triggering directly in hardware. It is an highly customizable platform that has been equipped with an high-speed CAN module (NI 9853) that allows to control motor drives and battery status. NI 9239 modules are used to acquire analog signals from brake and accelerator pedal, steering wheel angle, yaw rate gyro and accelerometers. NI 9421 module is instead used to acquire digital inputs like key switch and forward or reverse selector.

7.1.5 Transmission

EM have a speed range of 6000 rpm and a peak torque of 70 Nm, in order to obtain a suitable torque on wheels and a good top vehicle speed the transmission ratio is about 4. This transmission ratio is obtained by means of chains, one per each motor. Motors are connected to respective pinions shafts through flexible joints. Pinion type 08B with 13 teeth move the chains which drive the transmission shafts that are connected to wheels independently via homokinetic joints.

7.1.6 Driver's inputs

The steering-wheel line has been equipped with a potentiometer in order to measure steering-wheel rotation. The sensor is mounted on steer rack pinion thus the wheel steer angle is related to steering wheel rotation through suspensions kinematics.

Accelerator pedal is also equipped with two potentiometer for redundancy requirement.

Brake pedal is directly connected to the master cylinder pump that is connected to front brakes callipers. The driver's braking force is measured by a load scale fixed in between the

7.1.7 Sensors

The vehicle is equipped with yaw rate gyroscope and accelerometers to measure longitudinal and lateral accelerations. Vehicle speed is estimated from rear wheels angular rate which is taken from motor sensors which is read and used by motor drives.

7.2 Vehicle expected performances

The vehicle layout changes the overall vehicle characteristics in term of mass distribution. Table 7.1 reports the vehicle mass distribution of the new EV prototype with respect to the original ICE vehicle.

The mass of the vehicle, accounting also for driver's mass (70 kg), is increased from 218 kg to 345 kg. The cog is lowered of 51 mm and moved forward of 30 mm.

The pure longitudinal performances of the vehicle can thus be roughly evaluated.

Table 7.1: *Prototype mass distribution. Comparison with original FSAE vehicle. The mass of the vehicle accounts also for driver mass (70 kg).*

	m kg	J_x kg m ²	J_y kg m ²	J_z kg m ²	l_f mm	l_r mm	h_G mm	weight F/R
old ICE vehicle	218	16	51	62	786	889	297	53:47
new EM vehicle	345	23	58	74	756	920	246	55:45

Considering pure longitudinal dynamic equilibrium of the car, neglecting rolling and aerodynamic resistances, the longitudinal acceleration is

$$a_x = \frac{2F_{x,f} + 2F_{x,r}}{m} \quad (7.1)$$

The normal load on wheels is instead

$$F_{z,f} = \frac{m}{2l}(gl_r - a_x h_G) \quad (7.2)$$

$$F_{z,r} = \frac{m}{2l}(gl_f + a_x h_G) \quad (7.3)$$

When accelerating, considering the peak driving torque of the motors ($T_{m,\max} = 70$ Nm), the resulting maximum longitudinal acceleration $a_{x,\max}$ is

$$a_{x,\max} = \frac{2T_{m,\max}}{R_r \tau m} = 6.3 \text{ m/s}^2 \quad (7.4)$$

where R_r is the rolling radius (250 mm), τ is the transmission ratio due to chain pinion and gear ($z_1/z_2 = 15/58 = 1/3.87$).

When braking, the required torques on wheels that brake the car at friction limit ($a_x = \mu g$) are

$$F_{xf} = \mu \frac{mg}{2l}(l_r - \mu h_G) \quad (7.5)$$

$$F_{xr} = \mu \frac{mg}{2l}(l_f + \mu h_G) \quad (7.6)$$

$$(7.7)$$

Figure 7.6 reports the braking curve for the EV prototype. Longitudinal forces of the rear wheels (F_{xr}) are reported as function of longitudinal force on front wheels (F_{xf}). The secondary y axis reports the equivalent braking torque required to EMs that generate the longitudinal forces (F_{xr}) calculated according to the following equation

$$T_m = F_{xr} R_r \tau \quad (7.8)$$

7.2. VEHICLE EXPECTED PERFORMANCES

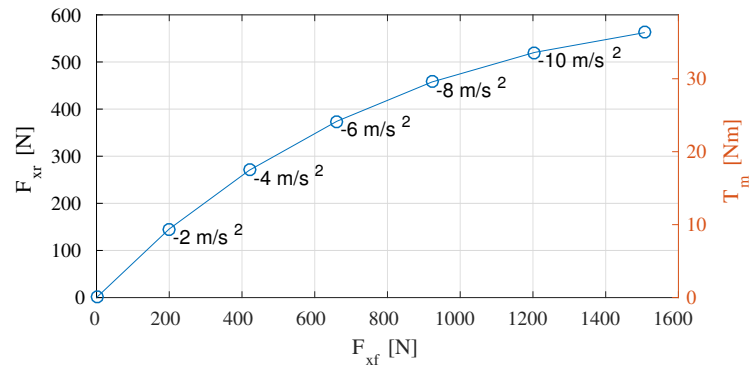


Figure 7.6: *EV prototype braking curve.*

As it can be noticed the regenerative braking torques of motor is enough to brake the rear wheels for really high decelerations. It means that no hydraulic brakes are required on the rear axle.

Conclusions

In this doctoral dissertation a new control strategy based on Torque Vectoring applied to 4 IWMs vehicle has been designed. It is made of two contributions: one for transient conditions, the other for steady-state conditions. This choice is driven by the necessity of increase vehicle stability in all conditions and to avoid wrong intervention that can arise in typical model based controllers.

The transient controller in fact does not need any vehicle model or vehicle state estimation except for vehicle speed estimation which is not a critical estimation in most common driving conditions. The transient controller can cancel steady-state contribution in critical conditions. In this way erroneous interventions of steady-state controller due to estimation lag are avoided.

The steady-state controller is instead based on a LQR applied to non linear single track vehicle model. This is possible due to the coupling with an EKF which is used both for vehicle state estimation and for friction coefficient estimation.

The effectiveness of the controller has been tested in several steady-state and transient manoeuvres both in close and open steer loop steer conditions. Also the effect of friction coefficient variation has been analysed. Simulations results showed that the control strategy can in fact increase vehicle performances in all tested driving conditions. For low lateral accelerations the active vehicle presents an higher degree of linearity with respect to passive vehicle, this make the vehicle easier and funnier to drive. The con-

troller helps in fact the driver to follow a reference trajectory with smaller corrections on the steering-wheel and with higher cornering performances. For high lateral acceleration, performances of the vehicle are in general increased in terms of maximum lateral achievable acceleration.

In transient conditions the active vehicle presents in general a smoother behaviour. Oscillations of yaw rate, lateral acceleration and side slip angle are reduced together with overshoot values. In this high transient conditions the transient controller by itself gives significant improvements with respect to the passive vehicle. This controller does not need the steady-state contribution and it can give significant improvements also if compared with classical brake based control systems.

The presented control strategy has also been applied to different powertrain layouts allowed by the use of independent motors. Same performance improvements are highlighted for all the layouts although small differences occur. In order to confirm controller performances also different front to rear weight distribution have been considered. From simulation results emerges that: four independent wheel driven vehicle seems to be the most performing solution both in steady-state and in transient conditions. Rear independent wheel driven vehicle presents an increase in steady-state performances with respect to its corresponding passive vehicle but is not so effective in damping oscillations during transients, in fact hydraulic brakes intervention on the front axle is needed in really critical oversteering conditions. Independent Front wheel driven vehicle is the most improving layout with respect to the corresponding passive vehicle and this makes this layout preferable with respect to other in term of mechanical complexity and probably costs. The only concern related to this layout is the performance in pure longitudinal acceleration if compared with other layouts; this condition was not enquired in this thesis. Plug-in solution for front and rear axles can be an optimal solution for expanding performances of existing vehicles. In particular the front axle with independent motors plug-in solution allows to obtain high benefits for rear wheel drive conventional sport cars in particular in cornering promptness and moreover in enhancing stability.

APPENDIX *A*

MF-Tyre model

MF-TYRE model by Pacejka is here reported as it is written in [30]. The Magic Formula model equations contain the non-dimensional model parameters p , q , r and s and, in addition, a set of scaling factors λ . Other parameters and variable quantities used in the equations are:

g gravity,

V_c magnitude of the velocity of the wheel contact centre C ,

$V_{cx,y}$ components of the velocity of the wheel contact centre C ,

$V_{sx,y}$ components of slip velocity V_s (of point S) with $V_{sy} \approx V_{cy}$,

V_r ($= R_e \Omega = V_{cx} - V_{sx}$) forward speed of rolling,

R_0 unloaded tyre radius,

R_e effective rolling radius,

Ω wheel speed of revolution,

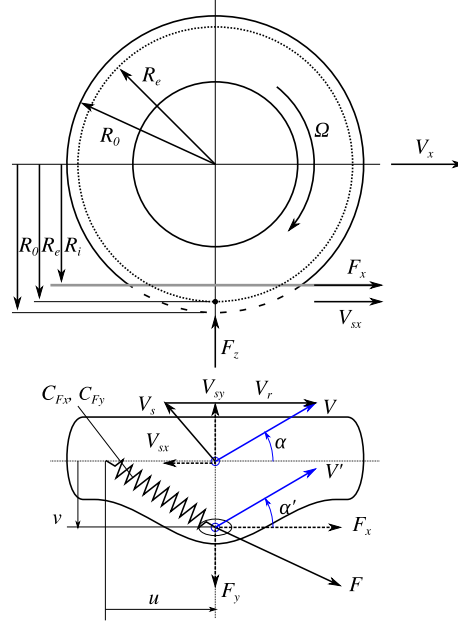


Figure A.1: Tyre reference quantities.

F_{z0} nominal load,

df_z the normalised change in vertical load $df_z = \frac{F_z - F_{z0}}{F_{z0}}$,

κ the longitudinal slip $\kappa = -\frac{V_{sx}}{V_{cx}}$.

Figure A.1 shows the meaning of the reported kinematic quantities.

A.1 Longitudinal Force (pure longitudinal slip)

$$F_{x0} = D_x \sin [C_x \arctan \{B_x \kappa_x - E_x (B_x \kappa_x - \arctan(B_x \kappa_x))\}] + S_{Vx} \quad (\text{A.1})$$

$$\kappa_x = \kappa + S_{Hx} \quad (\text{A.2})$$

$$C_x = p_{Cx1} \lambda_{Cx} \quad (> 0) \quad (\text{A.3})$$

$$D_x = \mu_x F_z \zeta_1 \quad (> 0) \quad (\text{A.4})$$

$$\mu_x = (p_{Dx1} + p_{Dx2} df_z) \lambda_{\mu_x}^* \quad (> 0) \quad (\text{A.5})$$

$$E_x = (p_{Ex1} + p_{Ex2} df_z + p_{Ex3} df_z^2) \{1 - p_{Ex4} \text{sign}(\kappa_x)\} \lambda_{Ex} \quad (\leq 1) \quad (\text{A.6})$$

$$K_{x\kappa} = F_z (p_{Kx1} + p_{Kx2} df_z) \exp(p_{Kx3} df_z) \lambda_{Kx\kappa} \quad (\text{A.7})$$

$$B_x = K_{x\kappa} / (C_x D_x + \varepsilon_x) \quad (\text{A.8})$$

$$S_{Hx} = (p_{Hx1} + p_{Hx2}df_z)\lambda_{Hx} \quad (\text{A.9})$$

$$S_{Vx} = (p_{Vx1} + p_{Vx2}df_z)\{|V_{cx}|/(\varepsilon_{Vx} + |V_{cx}|)\}\lambda_{Vx}\lambda'_{\mu x}\zeta_1 \quad (\text{A.10})$$

A.2 Lateral Force (pure side slip)

$$F_{y0} = D_y \sin [C_y \arctan \{B_y \alpha_y - E_y (B_y \alpha_y - \arctan(B_y \alpha_y))\}] + S_{Vy} \quad (\text{A.11})$$

$$\alpha_y = \alpha + S_{Hy} \quad (\text{A.12})$$

$$C_y = p_{Cy1}\lambda_{Cy} \quad (> 0) \quad (\text{A.13})$$

$$D_y = \mu_y F_z \zeta_2 \quad (> 0) \quad (\text{A.14})$$

$$\mu_y = (p_{Dy1} + p_{Dy2}df_z)(1 - p_{Dy3}\gamma^{*2})\lambda_{\mu y}^* \quad (> 0) \quad (\text{A.15})$$

$$E_y = (p_{Ey1} + p_{Ey2}df_z)\{1 - (p_{Ey3} + p_{Ey4}\gamma^*)\text{sign}(\alpha_y)\}\lambda_{Ey} \quad (\text{A.16})$$

$$K_{y\alpha 0} = p_{Ky1}F'_{z0} \sin[2 \arctan\{p_{Ky2}F'_{z0}\}]\lambda_{Ky\alpha} \quad (\text{A.17})$$

$$K_{y\alpha} = K_{y\alpha 0}(1 - p_{Ky3}\gamma^{*2})\zeta_3 \quad (\text{A.18})$$

$$B_y = K_{y\alpha}/(C_y D_y + \varepsilon_y) \quad (\text{A.19})$$

$$S_{Hy} = (p_{Hy1} + p_{Hy2}df_z)\lambda_{Hy} + p_{Hy3}\gamma^*\lambda_{Ky\gamma}\zeta_0 + \zeta_4 - 1 \quad (\text{A.20})$$

$$S_{Vy} = F_z\{(p_{Vy1} + p_{Vy2}df_z)\lambda_{Vy} + (p_{Vy3} + p_{Vy4}df_z)\gamma^*\lambda_{Ky\gamma}\}\lambda'_{\mu y}\zeta_2 \quad (\text{A.21})$$

$$K_{y\gamma 0} = \{p_{Hy3}K_{y\alpha 0} + F_z(p_{Vy3} + p_{Vy4}df_z)\}\lambda_{Ky\gamma} \quad (\text{A.22})$$

A.3 Longitudinal Force (combined slip)

$$F_{xs} = G_{x\alpha}F_{x0} \quad (\text{A.23})$$

$$G_{x\alpha} = \cos[C_{x\alpha} \arctan\{B_{x\alpha}\alpha_S - E_{x\alpha}(B_{x\alpha}\alpha_S - \arctan(B_{x\alpha}\alpha_S))\}]/G_{x\alpha 0} \quad (\text{A.24})$$

$$G_{x\alpha 0} = \cos[C_{x\alpha} \arctan\{B_{x\alpha}S_{Hx\alpha} - E_{x\alpha}(B_{x\alpha}S_{Hx\alpha} - \arctan(B_{x\alpha}S_{Hx\alpha}))\}] \quad (\text{A.25})$$

$$\alpha_S = \alpha^* + S_{Hx\alpha} \quad (\text{A.26})$$

$$B_{x\alpha} = r_{Bx1} \cos[\arctan(r_{Bx2}\kappa)]\lambda_{x\alpha} \quad (\text{A.27})$$

$$C_{x\alpha} = r_{Cx1} \quad (\text{A.28})$$

$$E_{x\alpha} = r_{Ex1} + r_{Ex2}df_z \quad (\text{A.29})$$

$$S_{Hx\alpha} = r_{Hx1} \quad (\text{A.30})$$

A.4 Lateral Force (combined slip)

$$F_{ys} = G_{y\kappa}F_{y0} + S_{Vy\kappa} \quad (\text{A.31})$$

$$G_{y\kappa} = \cos[C_{y\kappa} \arctan\{B_{y\kappa}\kappa_S - E_{y\kappa}(B_{y\kappa}\kappa_S - \arctan(B_{y\kappa}\kappa_S))\}]/G_{y\kappa 0} \quad (\text{A.32})$$

$$G_{y\kappa 0} = \cos[C_{y\kappa} \arctan\{B_{y\kappa}S_{Hy\kappa} - E_{y\kappa}(B_{y\kappa}S_{Hy\kappa} - \arctan(B_{y\kappa}S_{Hy\kappa}))\}] \quad (\text{A.33})$$

$$\kappa_S = \kappa + S_{Hx\kappa} \quad (\text{A.34})$$

A.5. RELAXATION LENGTH

$$B_{y\kappa} = r_{By1} \cos[\arctan\{r_{By2}(\alpha^* - r_{By3})\}] \lambda_{y\kappa} \quad (\text{A.35})$$

$$C_{y\kappa} = r_{Cy1} \quad (\text{A.36})$$

$$E_{y\kappa} = r_{Ey1} + r_{Ey2} df_z \quad (\text{A.37})$$

$$S_{Hy\kappa} = r_{Hy1} + r_{Hy2} df_z \quad (\text{A.38})$$

$$S_{Vy\kappa} = D_{Vy\kappa} \sin[r_{Vy5} \arctan(r_{Vy6}\kappa)] \quad (\text{A.39})$$

$$D_{Vy\kappa} = \mu_y F_z (r_{Vy1} + r_{Vy2} df_z + r_{Vy3} \gamma^*) \cos[\arctan(r_{Vy4} \alpha^*)] \zeta_2 \quad (\text{A.40})$$

A.5 Relaxation length

In order to account for force dynamics, the force on i -th wheel is thus calculate according to following differential equations

$$\begin{cases} \frac{L_x}{v_i} \dot{F}_{x,i} + F_{x,i} = F_{xs,i} \\ \frac{L_y}{v_i} \dot{F}_{y,i} + F_{y,i} = F_{ys,i} \end{cases} \quad (\text{A.41})$$

where v_i is the longitudinal velocity of wheel hub in wheel reference frame while L_x and L_y are the so called relaxation length respectively for longitudinal and lateral forces. L_x is comparable to contact path length while L_y is comparable to tyre circumference length.

Bibliography

- [1] Martyn Anderson and Damian Harty. “Unsprung Mass with In-Wheel Motors - Myths and Realities”. In: *10th International Symposium on Advanced Vehicle Control*. Loughborough, UK, 2010.
- [2] Francesco Braghin et al. “Race driver model”. In: *Computers & Structures* 86.13 (2008), pp. 1503–1516.
- [3] M. Canale et al. “Robust vehicle yaw control using an active differential and IMC techniques”. In: *Control Engineering Practice* 15.8 (2007). cited By 91, pp. 923–941. DOI: [10.1016/j.conengprac.2006.11.012](https://doi.org/10.1016/j.conengprac.2006.11.012).
- [4] Federico Cheli, Davide Ivone, and Edoardo Sabbioni. “Smart Tyre Induced Benefits in Sideslip Angle and Friction Coefficient Estimation”. In: *Sensors and Instrumentation, Volume 5*. Springer, 2015, pp. 73–83.
- [5] Federico Cheli et al. “A 14dof model for the evaluation of vehicle’s dynamics: numerical–experimental comparison”. In: *International Journal of Mechanics and Control* 6.2 (2006), pp. 19–30.
- [6] Federico Cheli et al. “Full energetic model of a plug-in hybrid electrical vehicle”. In: 2008, pp. 733–738. DOI: [10.1109/SPEEDHAM.2008.4581319](https://doi.org/10.1109/SPEEDHAM.2008.4581319).
- [7] U-sök Chõng, Eok Namgoong, and Seung-Ki Sul. “Torque steering control of 4-wheel drive electric vehicle”. In: *IEEE* (1996).
- [8] Leonardo De Novellis et al. “Comparison of feedback control techniques for torque-vectoring control of fully electric vehicles”. In: *IEEE Transactions on Vehicular Technology* 63.8 (2014), pp. 3612–3623.

BIBLIOGRAPHY

- [9] Leonardo De Novellis et al. “Torque vectoring for electric vehicles with individually controlled motors: state-of-the-art and future developments”. In: *26th Electric Vehicle Symposium 2012*. Los Angeles, California, USA, 2012.
- [10] Fabio Della Rosa, Gianpiero Mastinu, and Carlo Piccardi. “Bifurcation analysis of an automobile model negotiating a curve”. In: *Vehicle System Dynamics* 50.10 (2012).
- [11] E. Esmailzadeh, A. Goodarzi, and G.R. Vossoughi. “Optimal yaw moment control law for improved vehicle handling”. In: *Mechatronics* (2003).
- [12] Gianmarco Galmarini, Massimiliano Gobbi, and Gianpiero Mastinu. “A quadricycle for urban mobility”. In: *ASME 2012 International Design Engineering Technical Conferences and Computers and Information in Engineering Conference*. American Society of Mechanical Engineers. Houston, Texas, USA, 2012, pp. 451–458.
- [13] Cong Geng, Toshiyuki Uchida, and Yoichi Hori. “Body slip angle estimation and control for electric vehicle with in-wheel motors”. In: *Industrial Electronics Society, 2007. IECON 2007. 33rd Annual Conference of the IEEE*. IEEE. Boston, MA, USA, 2007, pp. 351–355.
- [14] C. Ghike, T. Shim, and J. Asgari. “Integrated control of wheel drive-brake torque for vehicle-handling enhancement”. In: *Proceedings of the Institution of Mechanical Engineers, Part D: Journal of Automobile Engineering* 223.4 (2009). cited By 19, pp. 439–457. DOI: [10.1243/09544070JAUTO1032](https://doi.org/10.1243/09544070JAUTO1032).
- [15] Tommaso Goggia et al. “Torque-vectoring control in fully electric vehicles via integral sliding modes”. In: *2014 American Control Conference*. IEEE. 2014, pp. 3918–3923.
- [16] Stephen J. Hallowell and Laura R. Ray. “All-wheel driving using independent torque control of each wheel”. In: *Proceedings of the American Control Conference*. IEEE. 2003.
- [17] M J Hancock et al. “A comparison of braking and differential control of road vehicle yaw-sideslip dynamics”. In: *Proc. IMechE*. 2005.
- [18] ISO. *Passenger cars – Braking in a turn – Open-loop test methods*. ISO 7401. 2006.
- [19] ISO. *Passenger cars – Steady-state circular driving behaviour – Open-loop test methods*. ISO 4138. 2012.
- [20] ISO. *Passenger cars – Test track for a severe lane-change manoeuvre – Part 1: Double lane-change*. ISO 3888-1. 1999.

-
- [21] ISO. *Road vehicles – Lateral transient response test methods – Open-loop test methods*. ISO 7401. 2011.
- [22] Leonidas Kakalis, Federico Cheli, and Edoardo Sabbioni. “The Development of a Brake based Torque Vectoring System for a Sport Vehicle Performance Improvement.” In: *ICINCO-ICSO*. 2009, pp. 298–304.
- [23] D-H Kim et al. “Optimal brake torque distribution for a four-wheel-drive hybrid electric vehicle stability enhancement”. In: *IMechE. J. Automobile Engineering*. 221. 2007. DOI: [10.1243/09544070JAUTO352](https://doi.org/10.1243/09544070JAUTO352).
- [24] J. Larminie and J. Lowry. *Electric Vehicle Technology Explained: Second Edition*. 2012. DOI: [10.1002/9781118361146](https://doi.org/10.1002/9781118361146).
- [25] Ferdinando Luigi Mapelli, Davide Tarsitano, and Marco Mauri. “Plug-in hybrid electric vehicle: Modeling, prototype realization, and inverter losses reduction analysis”. In: *Industrial Electronics, IEEE Transactions on* 57.2 (2010), pp. 598–607.
- [26] Gianpiero Mastinu and Manfred Ploechl. *Road and Off-road Vehicle System Dynamics Handbook*. Ed. by Gianpiero Mastinu and Manfred Ploechl. CRC Press, Taylor & Francis Group, 2014.
- [27] Satoshi Murata. “Innovation by in-wheel-motor drive unit”. In: *Vehicle System Dynamics* 50.6 (2012), pp. 807–830.
- [28] Eiichi Ono et al. “Vehicle dynamics integrated control for four-wheel-distributed steering and four-wheel-distributed traction/braking systems”. In: *Vehicle System Dynamics* 44.2 (2006), pp. 139–151.
- [29] Russell P Osborn and Taehyun Shim. “Independent control of all-wheel-drive torque distribution”. In: *Vehicle system dynamics* 44.7 (2006), pp. 529–546.
- [30] Hans B. Pacejka. *Tyre and Vehicle Dynamics*. Second. Oxford, UK: Butterworth-Heinemann, 2006.
- [31] Andrew Pennycott et al. “Enhancing the energy efficiency of fully electric vehicles via the minimization of motor power losses”. In: *2013 IEEE International Conference on Systems, Man, and Cybernetics*. IEEE. 2013, pp. 4167–4172.
- [32] Lorenzo Pinto et al. “Advanced yaw motion control of a hybrid vehicle using twin rear electric motors”. In: *Advanced Vehicle Control*. Vol. 4. 2010, pp. 640–645.

BIBLIOGRAPHY

- [33] P. Pusca et al. “Fuzzy-logic-based control applied to a hybrid electric vehicle with four separate wheel drives”. In: *IEE Proc.-Control Theory Appl.* Vol. 151. 1. 2004.
- [34] R.J. Rieveley and B.P. Minaker. “Variable torque distribution yaw moment control for hybrid powertrains”. In: *SAE Technical Papers* (2007). DOI: [10.4271/2007-01-0278](https://doi.org/10.4271/2007-01-0278).
- [35] Edoardo Sabbioni et al. “Comparison of torque vectoring control strategies for a IWM vehicle”. In: *SAE International Journal of Passenger Cars-Electronic and Electrical Systems* 7.2 (2014), pp. 565–572.
- [36] Shin-ichiro Sakai, Hideo Sado, and Yoichi Hori. “Dynamic Driving/Braking Force Distribution in Electric Vehicles with Independently Driven Four Wheels”. In: *Electrical Engineering in Japan* 138.1 (2002).
- [37] Shin-ichiro Sakai, Hideo Sado, and Yoichi Hori. “Motion control in an electric vehicle with four independently driven in-wheel motors”. In: *Mechanics, IEEE/ASME Transactions on* 4.1 (1999), pp. 9–16.
- [38] Justin H Sill and Beshah Ayalew. “Managing axle saturation for vehicle stability control with independent wheel drives”. In: *Proceedings of the 2011 American Control Conference*. IEEE. 2011, pp. 3960–3965.
- [39] Justin Sill and Beshah Ayalew. “A saturation-balancing control method for enhancing dynamic vehicle stability”. In: *International Journal of Vehicle Design* 61.1-4 (2012), pp. 47–66.
- [40] R Vos, IJM Besselink, and H Nijmeijer. “Influence of in-wheel motors on the ride comfort of electric vehicles”. In: *Proceeding of the 10th International Symposium on Advanced Vehicle Control (AVEC'10)*. 2010, pp. 835–840.